Mechanical and Dynamic Properties of Mixed Modifier Silicate Glasses and Vanadium-Tellurite Glasses

Kjeldsen, Jonas

Publication date:
2014

Document Version
Publisher's PDF, also known as Version of record

AALBORG UNIVERSITY
DENMARK

Ph.D. Dissertation

Mechanical and Dynamic Properties of Mixed Modifier Silicate Glasses and Vanadium-Tellurite Glasses

By
Jonas Kjeldsen

Section of Chemistry
Department of Chemistry and Bioscience
Aalborg University, Denmark

Date of Defence
December 5th 2014

Assessment Committee

Morten Lykkegaard Christensen
Associate Professor
Aalborg University
Denmark

Edgar Dutra Zanotto
Professor
Federal University of São Carlos
Brazil

Tor Grande
Professor
Norwegian University of Science and Technology
Norway

Supervisor

Yuanzheng Yue
Professor
Aalborg University
Denmark

Preface and Acknowledgements

This dissertation is submitted to the Faculties of Engineering and Science, Aalborg University in partial fulfilment of the requirements for obtaining the Ph.D. degree. The Ph.D. study was carried out from October 2011 to October 2014. The work was primarily performed at the Section of Chemistry at Aalborg University with external stays at Federal University of São Carlos. The study was partially financed by Aalborg University and partially by Corning Incorporated.

First of all I would like to thank my supervisor Yuanzheng Yue for his dedicated supervision, encouragement, and helpful nature. I am truly grateful for your believe in me and for the enrolment as your Ph.D. student at Aalborg University. I have learned a lot during my stay and enjoyed our daily collaboration, and I hope this collaboration can carry future mutual projects. I will also take this chance to acknowledge my unofficial co-supervisor Ana C.M. Rodrigues from Federal University São Carlos, who took me in and facilitated my stays in Brazil. I appreciate the help and support, and hope we can keep collaborating on future ventures.

My kind acknowledgements go to Corning Incorporated for the financial support, and especially to the employees John C. Mauro and Marcel Potuzak, plus former Corning Inc. employee Morten M. Smedskjaer. John C. Mauro and Morten M. Smedskjaer believed in me and my ideas, contributed with valuable discussions, and facilitated glass production and characterisation through the Characterization and Materials Processing Directorate at Corning Incorporated. Without their help, most of the studies presented in this thesis would not have been possible, and I am grateful for their complete support throughout my studies. Marcel Potuzak helped by providing glass samples and valuable discussion, which enabled for studies impracticable at Aalborg University. I have appreciated the collaboration and thank you for your kind nature.

I would like to thank Susanne Mossin at the Technical University of Denmark for providing me access to their laboratories and for performing supplementary electron spin resonance measurements. Thanks to Randall E. Youngman at Corning Incorporated for conducting nuclear magnetic resonance spectroscopy, and for providing helpful discussion and analysis. Liping Huang at Rensselaer Polytechnic Institute for conducting Raman spectroscopy, and Caio B. Bragatto at Federal University of São Carlos for conducting impedance spectroscopy.

Thanks go to present and former members of the Center for Amorphous Materials Science at Aalborg University for providing a functioning social and scientific working environment. I have enjoyed our collaboration and numerous discussions of both scientific and non-scientific character. Special thanks go my former fellow engineering students, Rasmus R. Petersen, Thuy T. Do, and Christian Hermansen for accompanying me on this journey. You have been amazing company and I will miss our daily communication.

Abstract

Due to the fascinating and complicated amorphous structure of glass, composition-structure-property relations are hitherto not well established. The properties of glasses are large determined from the structure of the glass, which in turns is determined by the composition of the glass. Establishing these composition-structure-property relations are important both from scientific and technical point of views, as these relations enable design of glasses with properties specifically tailored for an application. The aim of the present Ph.D. thesis is to obtain a better understanding of transport processes and mechanisms in inorganic glass, and gain insights into the link between composition, structure and property. Transport processes in glass are especially important when designing glass products for architectural purposes, for personal electronic devices, and batteries.

To achieve a coherent picture of the transport mechanisms in glass we investigate two series of vanadium tellurite glass and six mixed modifier aluminosilicate glass series. We determine the influence of composition and critical parameters on the processes and mechanisms of transport, and reveal physical links between structure characteristics and compositional property scaling. In detail, for the vanadium tellurite glasses we study the influence of redox state, carrier concentration, and crystallinity on the electronic conductivity and correlate the compositional influence of structure on hardness, viscosity, and liquid fragility. For the mixed modifier aluminosilicate glasses we correlate the specific ratios between the deformation processes under indentation to the accompanying structural changes and Vickers hardness. Finally, we discuss the compositional trends of density, glass transition temperature, elastic moduli, and Poisson's ratio in regard to existing theoretical models and reveal direct composition-structure-property relations.

In the vanadium tellurite glasses we find a strong correlation between the valence state of the vanadium and glass properties related to the connectivity of the network, i.e., hardness and liquid fragility. We propose the existence of a critical vanadia concentration equal to 45 mol%, and explain the compositional trends in hardness and liquid fragility by V^{4+} resulting in a more constrained structure than V^{5+}. We show that the electronic conductivity of the vanadium tellurite glass occurs strictly adiabatic and correlates linearly to the average jump distance and non-linearly to the redox state of vanadium. Out of the three critical parameters for electronic conduction (redox state of electron carrier, distance between electron carriers, and activation energy for jumps between electron carriers) we find the distance between electron carriers to have the largest influence on the electronic conductivity. The decoupling of electronic conductivity from the valence state of vanadium, combined with the strong influence of the valence state of vanadium on liquid fragility and hardness, enables optimization of hardness and liquid fragility independent from the electronic conductivity. This structure-property link is technical important for glass applications such as cathodes in secondary batteries.

In the mixed modifier aluminosilicate glasses we find that the structural trademark of the mixed modifier effect results in universal negative deviations from linearity in glass transition temperatures and liquid fragility indices. We explain the mixed modifier effects on glass transition temperatures and liquid fragility via an overall bond weakening in the vicinity of the network modifying ions, combined with a positive deviation in tetrahedrally bonded silica units. We find no correlation between hardness and either elastic deformation or densification under indentation, but a

positive correlation between hardness and the plastic flow part of indentation. We propose the hardness of mixed modifier glasses is dominated by the resistance to plastic flow, and that the amount of plastic flow under indentation is closely related to glass viscosity. An increase in viscosity increases the resistance to plastic flow of the mixed modifier glasses, and thus increases glass hardness. This structure-property link is potentially important for glass applications such as cover glass.

We observe an interesting structure characteristic of the mixed alkali effect which results in positive deviations from linearity in both density and hardness. We explain the compositional scaling by two opposite scenarios; (i) general bond weakening around the network modifying ions (universal for the mixed modifier effect), and (ii) a tight-knit structure only available at low temperatures (unique to the mixed alkali effect). These two effects counterbalance each other and explain the compositional trends of positive deviations from linearity in density and hardness, and the negative deviations from linearity in glass transition temperatures and liquid fragility.

Resume (Danish Abstract)

Grundet den fascinerende og komplicerede amorfe struktur af glas er komposition-struktur-egenskab relationer endnu ikke vel etableret. Egenskaberne af glas er bestemt ud fra strukturen af glasset, som igen er bestemt af kompositionen. Etableringen af komposition-struktur-egenskab relationer er vigtig både fra videnskabelige og tekniske synspunkter, efter som disse relationer gør det muligt at designe glas med egenskaber skræddersyet til en bestemt applikation. Målet med denne Ph.D. afhandling er at opnå en bedre forståelse af transport processer og transport mekanismer i uorganisk glas, og få indsigt i relationerne imellem komposition, struktur og egenskaber. Transport processer i glas er specielt vigtige når man designer glas produkter for arkitekturiske formål, personlige elektroniske apparater og batterier.

For at opnå et sammenhængende billede af transport mekanismerne i glas undersøger vi to serier af vanadium tellurite glas og seks miksede modificerede aluminiumsilikat glas serier. Vi bestemmer indflydelsen af komposition og kritiske parametre på processerne og mekanismerne for transport, og afslører fysiske links imellem karakteristiske strukturer og kompositionel egenskabs skalering. I detalje studerer vi for vanadium tellurite glassene indflydelsen af redox stadie, elektronbærer koncentrationen og krystalgraden på den elektroniske konduktivitet, og korrelerer den kompositionelle indflydelse af struktur på hårdhed, viskositet og væske skrøbelighed. For de seks miksede modificerede aluminiumsilikat glas serier korrelerer vi den specifikke ratio imellem deformations processer under tryk til ledsagende strukturelle ændringer og hårdhed. Til sidst diskuterer vi de kompositionelle tendenser af densitet, glas transitions temperaturer, elastisk moduli og Poisson's ratio i henhold til eksisterende teoretiske modeller og afslører direkte komposition-struktur-egenskab relationer.

I vanadium tellurite glassene finder vi en stærk sammenhæng imellem valens stadie af vanadium og glasegenskaber relateret til bindingstætheden i glasnetværket, dvs. hårdhed og væske skrøbelighed. Vi foreslår eksistensen af en kritisk V_2O_5 koncentration lig med 45 mol% og forklarer de kompositionelle tendenser af hårdhed og væske skrøbelighed med at V^{4+} resulterer i flere bindinger end V^{5+}. Vi viser at den elektroniske konduktivitet af vanadium tellurite glas sker udelukkede adiabatisk og korrelerer lineært til den gennemsnitlige hop afstand og ikke-lineært til redox stadiet af vanadium. Ud af de tre kritiske parametre for elektron konduktivitet (redox stadie af vanadium, afstand imellem vanadium ioner og aktiverings energi for hop imellem vanadium ioner) finder vi at afstanden imellem vanadium ioner har størst indflydelse på elektron konduktiviteten. Frakoblingen af elektronisk konduktivitet fra valens stadie af vanadium, kombineret med den stærke indflydelse af valens stadie af vanadium på hårdhed og væske skrøbelighed, åbner for optimering af hårdhed og væske skrøbelighed uafhængigt fra elektron konduktiviteten. Denne struktur-egenskab relation er teknisk vigtig for glas anvendelser såsom katoder i sekundære litium batterier.

I de miksede modificerede aluminiumsilikat glas serier finder vi at det strukturelle varemærke for den miksede modificerende effekt resulterer i universelle negative deviationer fra linearitet i glas transition temperaturer og væske skrøbeligheder. Vi forklarer den miksede modificerende effekt på glas transition temperaturer og væskeskrøbeligheder via en overall svækkelse i bindingsstyrke i området omkring de netværk modificerende ioner kombineret med en positiv afvigelse i mængden af tetrahedralt bundet silikatenheder. Vi finder ingen korrelation imellem hårdhed og enten den

elastiske part eller densifikationsparten under tryk, men finder en positiv korrelation imellem hårdhed og mængden af plastisk flow under tryk. Vi foreslår at hårdheden af miksede modificerende glas er domineret af modstanden mod plastisk flow og at mængden af plastisk flow er tæt forbundet med viskositet. En forøgelse i viskositet øger modstanden mod plastisk flow af miksede modificerende glas og forøger derved hårdheden af glasset. Denne struktur-egenskab relation er potentielt vigtig for glasanvendelser såsom dækglas.

Vi observerer en interessant karakteristisk struktur for den miksede alkali effekt hvilket resulterer i positive deviationer fra linearitet i både densitet og hårdhed. Vi forklarer den kompositionelle skalering via to modstridende scenarier; (i) en general svækkelse i bindingsstyrke omkring de modificerende ioner (universel for den miksede modificerende effekt) og (ii) en tæt knyttet struktur som kun er tilgængelig ved lave temperaturer (unik for den miksede alkali effekt). Disse to effekter afbalancerer hinanden og forklarer de kompositionelle tendenser af positive deviationer fra linearitet i densitet og hårdhed and de negative deviationer fra linearitet i glas transition temperaturer og væske skrøbeligheder.

Table of Contents

1. Introduction

Man-made glass dates back to 7000 B.C [1], and ever since glass has been a part of our daily life. In early time, glass was merely used for jewellery, but eventually, with the intervention of glass blowing in the 1st century, the range of applications greatly expanded. Glass found its appearance as containers and in construction, but the main focus remained on decoration. The science of glass was for a long period strongly limited by homogeneity issues, and the connection between composition and property remained undeveloped. The chemistry behind the glassy state was not accessed before the 19th century, where advanced stirring methods were developed. In modern society glass is ubiquitous, ranging from practical usages as containers, windows, covers, and kitchenware all the way to high technical usages as in optical fibres for telecommunication, liquid crystal displays and substrates [2]. A whole range of human requirements are met by glass, and more than 90% of the glass in use is silica-based oxide glass. Silica is however not a requirement for glass formation, and the glassy state can be achieved in literally all elements of the periodic table, solely or in mixtures [3]. The above listed applications are covered exclusively by oxide glass, but the glassy state can also occur as metallic glass and even in plastics.

Time has encountered many definitions of glass and through that a general consensus has evolved [3,4]. From a structural perspective, a glass is a liquid which has lost its ability to flow [5]. Glass is normally produced by fast cooling of a liquid, where the liquid is cooled within a timescale shorter than that of crystallisation. That is, so fast that the individual atoms do not have time to find their respective lattice position and effectively freezes in place. The resulting solid (i.e., a glass) thus mimics that of the last thermally equilibrated liquid. In scientific terms, glass may be defined as amorphous solid lacking long range order and exhibits time-dependent glass transition behaviour. The glass transition region is the temperature range, where the liquid leaves its equilibrium and enters a meta-stable solid state relative to the corresponding crystal [4]. Basically, glass lacks order and periodicity.

From the 19th century to today, the science behind glass has transformed into a major field of interest, especially with respect to the structure-property relationship. Since Zachariasen in 1932 published the seminal paper about the random network theory of oxide glasses [6], the glass structure and its relation to physical and chemical properties have been intensively investigated [7-9]. Even today, the structure of many glass systems has not been fully revealed. Only recently, with the advances in high resolution microscopy techniques, scientists have obtained true sight of the atomic arrangement of individual atoms in the glass, and verified the random network theory [10]. Since the glass structure dictates the properties of the glass, understanding and prediction of the glass structure is of important technical interest. With help of computer simulation [11,12], network constraint theory [13,14], the dynamic structure model [15,16] and the modified random network model [17,18], the understanding of the glass structure and the structure-property relationship will be greatly enhanced in the future.

1.1. Background and Challenges

Glass is intrinsically a liquid, and whereas the transport mechanism in liquids occurs by self-diffusion and well understood [19,20], in the case of glasses, the process of transport remains

unanswered. The individual components of inorganic glass can, via Dietzel's model of field strength [21], be separated into three categories; (i) network formers, (ii) intermediates, and (iii) network modifiers. Network formers (e.g. Silica, boron, and germanium) exhibit covalent bonding to neighboring atoms, creating the solid framework. Network modifiers (e.g. sodium, calcium, and potassium) form ionic bonds and therefore experience some degree of freedom. Intermediates (e.g. aluminium and beryllium) are in between and can occur in both bonding schemes. The covalent bonds found between network formers are stronger than the ionic bonds that the network modifiers create, and thus only network modifiers experience self-diffusion. As only a part of the glass network can diffuse, the self-diffusion model doesn't apply to glass. Existing models concerning transport in glasses thus revolve around the mobility of the network modifiers [16,18]. Achieving a coherent picture of the general mechanisms of mass transfer in glass also requires understanding of the influence of the network formers on the transport processes. The main aim of the present Ph.D. thesis is to gain insights into the dynamic properties of glass and get a coherent understanding of the mechanisms of mass transfer. In detail, we look at deformation processes under indentation, elastic moduli, and viscosity as key parameters, since these parameters account for the combined behavior of both network modifiers and network formers. To get a coherent understanding of the transport processes in glass, we also investigate the influence of individual movement of electrons and ions, and relate to both structure and properties of the glass. The secondary aim of the present Ph.D. thesis is to achieve a fundamental understanding of transport in glass, and thereby facilitate for new technical applications of glass.

Over the past decades a considerable interest in studying the conduction behavior of both electrons and ions in glasses has evolved. Such study dates back to 1847 with Kohlrausch's work on vitreous ionic materials, and hence has continued for more than 160 years old. Despite most scientific problems have been solved, some important questions regarding electron and ionic conductivity remains unanswered [22]. Regarding the ionic conductivity, the general consensus is that the diffusion of mobile ions occurs via hopping between potential minima in the glass network, and several models for the ionic conduction have been proposed [23]. These models include the diffusion controlled relaxation model [24], the jump diffusion model [25], the weak electrolyte model [26,27], the strong electrolyte model [28] and the dynamic structure model [15,29]. However, none of the models are capable of describing the fundamentals of the ionic transport to a satisfying degree [16]. The exact mechanism of ion transport is thus remains unknown. Turning to the electronic conductivity the proposed conducting mechanism is that of polarons, where the theory is adapted from polarons in crystals [30]. Either the mechanism for electronic conductivity or the mechanism for ionic conductivity is fully understood and neither is the influence of critical parameters on the conduction mechanisms. Conducting glass is used for several applications, e.g., batteries, fuel cells, smart windows, and chemical sensors, so an explicit understanding of the underlying mechanism of conduction is essential for future product development [16,31].

In order to achieve a coherent picture of the transport mechanisms in glass it is necessary to investigate and determine the influence of composition and critical parameters on the mechanisms of transport. We study a model vanadium-tellurite system to evaluate the influence of redox state, carrier concentration, and crystallinity on the electronic conductivity. The compositional influence

on hardness, viscosity, and liquid fragility is evaluated, and correlated to the structure of the vanadium tellurite glasses.

Most modifier-containing oxide glasses exhibit non-additive variations of certain properties when one modifier ion is substituted by another one, and hence are ideal systems for studying the link between dynamic properties and structure. The phenomenon of non-additive variations in properties during substitution of network modifier ions is nominated the “mixed modifier effect” and is one of the most intriguing unsolved phenomena of glass science [31,32]. The mixed modifier effect manifests itself in non-additive discrepancies in transport properties, such as diffusion, conductivity, and viscosity. These properties are commonly referred to as dynamic properties, in contrast to static properties such as density, refractive index, and molar volume, all of which exhibit relatively small deviations from linearity [33,34]. The mixed alkali effect (i.e. substitution of one alkali ion by another) has been known for decades, yet it continually draws significant attention [34-39]. In contrast, the mixed alkaline earth effect (i.e. substitution of one alkaline earth ion by another) and the mixed alkali-alkaline earth effect (i.e. substitution of one alkali ion by an alkaline earth ion) have received little attention. Both are phenomenologically analogous to the mixed alkali effect, i.e., concerns substitution of one modifier ion by another one, The influence of both the mixed alkaline earth and the mixed alkali-alkaline earth effect on glass properties is also analogous to that of the mixed alkali effect, i.e., deviations from linearity are mainly observed in dynamic properties [40-44]. The mixed modifier effect is throughout the present Ph.D. thesis used as a collective name for the mixed alkali, mixed alkaline earth, and mixed alkali-alkaline earth effects. Since the mixed modifier effect affects glass properties in a non-predictive manner, studying the mixed modifier effect is important from both a scientific and a technical point of view.

Despite the structural and topological origins of the mixed modifier effect have been explored by large amounts of experimental and modeling work, a thorough understanding of these origins remains lacking [23,44,45]. Despite making progress in interpreting the mixed modifier effect by establishing phenomenological and physical models for ionic conduction, experimental findings cannot be theoretically explained to a satisfying degree. The mixed modifier effect has primarily been investigated in silicate and aluminosilicate glass due to the industrial importance of these systems, e.g., as chemically strengthened cover glasses in personal electronic devices [46] and for modern architectural purposes [35,47]. In a systematic investigation of glass properties and their dependence of the mixed modifier effect, Byun *et al.* [48] conclude that no simple mechanism is responsible for the observed nonlinearities. Moreover, they point out that the deviation from linearity of certain properties is intimately connected with microscopic structural changes. Hence, in order to reveal the origin of the mixed modifier effect, the accompanying structural changes must be recognized.

In the present Ph.D. thesis we study six mixed modifier aluminosilicate systems and correlate the specific ratios between the deformation processes under indentation to the accompanying structural changes and Vickers hardness. We discuss the compositional trends of structural, mechanical and dynamic properties in regard to existing theoretical models and reveal direct relations amongst mechanical and dynamic properties and glass structure.

1.2. Objectives

1. Achieve a better overall understanding of transport processes in inorganic glass
2. Clarify the influence of critical parameters such as degree of crystallinity, redox state of carrier, and carrier concentration on electronic conductivity.
3. Clarify the influence of electron and ion motion in regard to bulk properties and structure of glass.
4. Investigate the physical link between Vickers hardness and properties related to structural rearrangement (e.g. Poisson's ratio, liquid fragility and elastic moduli).
5. Clarify the impact of chemical composition on deformation processes under indentation and link to accompanying topological and structural changes.

1.3. Thesis Content

The thesis is presented as a plurality, including an introductory overview followed by papers. The thesis is based in the following publications (in the text these papers are referred to by roman numerals).

I: J. Kjeldsen, A.C.M. Rodrigues, S. Mossin, and Y.Z. Yue, "Critical V_2O_5/TeO_2 Ratio Inducing Abrupt Property Changes in Vanadium Tellurite Glasses," *J. Phys. Chem. B* **118** (2014) 14942-14948.

II: J. Kjeldsen, M.M. Smedskjaer, J.C. Mauro, and Y.Z. Yue, "Hardness and Incipient Plasticity in Silicate Glasses: Origin of the Mixed Modifier Effect," *Appl. Phys. Lett.* **104** (2014) 051913.

III: J. Kjeldsen, M.M. Smedskjaer, J.C. Mauro, and Y.Z. Yue, "On the Origin of the Mixed Alkali Effect on Indentation in Silicate Glasses," *J. Non-Cryst. Solids* **406** (2014) 22-26.

IV: J. Kjeldsen, M.M. Smedskjaer, J.C. Mauro, R.E. Youngmann, L. Huang, and Y.Z. Yue, "Mixed Alkaline Earth Effect in Sodium Aluminosilicate Glasses," *J. Non-Cryst. Solids* **369** (2013) 61-68.

V: J. Kjeldsen, M.M. Smedskjaer, M. Potuzak, and Y.Z. Yue, "Role of Elastic Deformation in Determining the Mixed Alkaline Earth Effect of Hardness in Silicate Glasses," *J. Appl. Phys.* **117** (2015) 034903.

VI: J. Kjeldsen, Y.Z. Yue, C.B. Bragatto, and A.C.M. Rodrigues, "Electronic Conductivity of Vanadium-Tellurite Glass-Ceramics," *J. Non-Cryst. Solids* **378** (2013) 196-200.

This thesis has been submitted for assessment in partial fulfillment of the PhD degree. The thesis is based on the submitted or published scientific papers which are listed above. Parts of the papers are used directly or indirectly in the extended summary of the thesis. As part of the assessment, co-

author statements have been made available to the assessment committee and are also available at the Faculty. The thesis is not in its present form acceptable for open publication but only in limited and closed circulation as copyright may not be ensured.

2. Structure, Dynamics and Properties of Glass and Glass Forming Melts

In order to discuss mass transfer processes in connection to structural and topological changes in the glass, it is important to obtain a fundamental understanding of the glassy structure and key properties. Therefore, we start by reviewing the vitreous state and then look at the primary properties of interest and establish the link between the individual property and the structure.

2.1. Relevant Structural and Kinetic Aspects

Glass structure was not accessed before the beginning of the last century when Tammann was the first to investigate glasses from a structural perspective [3]. He regarded glasses as strongly supercooled liquids and believed that the structure of the glass was similar to that of a liquid [49]. In 1926, Goldschmidt [50] evolved the theory of glass structure and proposed that cations of a certain size invoke glass formation as these cations were able to coordinate to 4 oxygen ions. This condition was fulfilled in the case of e.g. SiO_2, P_2O_5, B_2O_3 and GeO_2 [1]. The model by Goldschmidt lacked information about the topology and assumed that all oxides behaved purely ionic. Zachariasen [6] continued the work of Goldschmidt and formulated rules for glass formation and proposed covalent bonding similar to that found in crystals. His rules revolved around the oxygen ions, and stated that; (i) each oxygen ion should be linked to no more than two atoms and (ii) that each oxygen ion polyhedra shared corners, not edges or faces. Following these rules leads to the formation of a random network of oxygen polyhedra and consequently the glass structure as depicted in Figure 2.1.

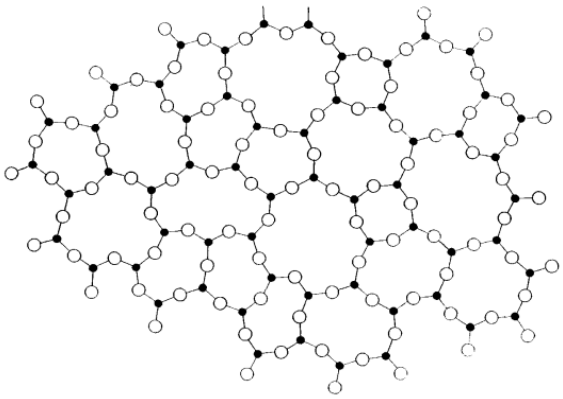

Figure 2.1: Representation of the glassy network following the rules proposed in Ref. [6].

The model proposed by Zachariasen [6] defines the glass structure as an extended network of corner sharing oxygen polyhedra, lacking periodicity, and energetically comparable to the corresponding crystal structure. As the glassy network is continuous and intrinsically random, it is often referred to as a continuous random network. The glass consists of an interpenetrating network of cations bonded to oxygen anions, termed bridging oxygen (BO). Any non-bonding oxygen ion is termed non-bridging (NBO). When a highly ionic oxide (e.g. Na_2O) is added to the network, it breaks the

Si-O-Si linkages, and creates an ionic bond to the oxygen, i.e., an NBO. The introduction of Na_2O therefore depolymerises the formed SiO_2 network, hence the names "network modifier" and "network former". Smekal [51] recognized that in order to achieve glass formation, a mixture of both covalent and ionic bonding was essential. Pure covalent and pure ionic bonding both induce crystalline order, but when bond lengths and angles can vary, short range order is eliminated and glass can persist. The major weakness of prior models was that the nature of the bonding was not considered. In 1952, Stanworth [52] introduced an electronegativity criterion to differentiate between atoms and their bonding characteristics. The ionic character of the atoms was standardised and their bonding scheme in the glass deduced.

With recent development in spectroscopic techniques we have reached the realisation that the bonding of each atom is depending on the surrounding network, and cannot be completely classified theoretically. The bond angles in a glass are distributed following a bell distribution [53,54], and whereas former models predicts strict chemical order, the rule of chemical order is not always obeyed [55]. A glass is an amorphous solid without long-range periodic structure and its fascinating nature continuously attracts our attention. For instance, one of the complicated features of glass is the so-called boron and aluminium anomalies [56,57].

2.1.1. Boron and Aluminium Anomalies

The network modifying ions possesses different structural roles depending on the glass environment. In pure silica glass, the network modifiers disrupt the network connectivity and create NBOs, thus network modifiers increase the flexibility of the entire network by creating flobby nodes. In pure boron, all boron is initially three coordinated (trigonal), however, with addition of modifier, the boron become four coordinated (tetrahedral) and is charge compensated by a modifier ion. With further increase in modifier concentration the fraction of tetrahedral boron reaches a maximum after which it decreases due to the formation of NBOs [58]. Because an energetic difference exists between the configurations the network modifying ions can participate in, the network modifier ions enter a thermodynamic competition between the formation of an NBO and the conversion of boron from trigonal to tetrahedral configuration.

Analogue to boron, aluminium requires network modifiers to charge compensate and stabilize the aluminium in a tetrahedral configuration. As the aluminium coordination changes from three to four, the connectivity of the network increases, as in complete contrast to the consequences of adding modifier to pure silica glass. In aluminosilicate glass, the modifiers are in a thermodynamic equilibrium where the formation of four coordinated aluminium is energetically preferred. Meaning that, under the circumstances of excess modifier, all aluminium will be charge balanced in the four coordinated tetrahedral configuration. In the case of excess aluminium, some aluminium ions take a charge balancing role as five- or six-fold coordinated. Viz., when network modifying ions are unavailable, aluminium ions take the role as charge compensator in higher coordination configurations [15]. The individual energy of the network modifier sites largely depend on; (i) the neighbouring atoms, (ii) the atom itself, and (iii) the structural role it takes. Some network modifier ions are thus better charge compensators than others, and when more than one network modifier is available, a competition arises. As a general rule, an excess of network modifier in relation to

aluminium, results in all aluminium being change balanced by network modifier and existing in tetrahedral four-fold coordination [57].

2.1.2. The Mixed Alkali Effect and Structure Models Concerning Ionic Mobility

Network modifying ions, which are characterised by their ionic bonding character, are found to diffuse completely decoupled from the amorphous matrix [59]. As network modifiers ions diffuse much faster than the remaining glass network, i.e., the network formers, the general consensus among scientists have been that the network modifiers are responsible for the initial movement under strain. A structural and topological origin of the diffusive behaviour of network modifiers have been the subject of much experimental and modelling work, but a coherent picture is not yet achieved [44,45].

Glass systems containing alkali oxides experience non-linear variation of several properties during gradual substitution of one alkali by another. The non-linear behaviours excel in electronic conductivity, internal friction, and viscosity, all of which involve ionic motion [3]. The generic term for the non-linear behaviours is the mixed alkali effect, and since 1884 where the mixed alkali effect was first encountered, it has attracted attention from scientists [1,34,39,60]. A number of approaches have been made in attempt to understand the origin of the mixed alkali effect, all of which emphasize on the structure and bonding aspects around the network modifier ions. Among early approaches, Stevels [61] argued that the free volume of the glass was responsible for the mixed alkali effect, as interstitial spacing in the glass has a size distribution easier filled by two alkali ions. Filled interstices are structurally more stable, which increases the activation energy for ionic motion and result in the mixed alkali effect [3]. From the perspective of filling free volume in the glass, the involved gradual substitution does not need to revolve around two alkali ions, but also occur for the mixed alkaline earth, the mixed alkali-alkaline earth, and the mixed modifier effects in general.

The introduction of the dynamic structure model [15,29] has helped to establish a more coherent picture of ionic conductivity in glass [3,16,39,62]. The dynamic structure model was primarily developed to explain the mixed modifier effect, but also applies to single network modifier glasses. In short, the dynamic structure model is based on an energy landscape approach, in which the unoccupied interstitial sites initially are associated with a relatively high potential energy. As the previously unoccupied interstitial sites become occupied, the surrounding atoms in the glassy network orders accordingly. Consequently, the structural rearrangement creates a difference in potential energy for occupied and unoccupied interstitial sites. When an ion leaves its site, the associated potential energy relaxes back to that of the unoccupied site. Thus, there exists a time window during which the occupation of this site by a similar ion is energetically favoured. As the relaxation time and the potential energy associated with the ion site depend on the type of ion, each ion creates its own preferred pathway in the network, and participates in the evolution of the energy landscape. Several studies have demonstrated that the mixed alkali effect has a structural origin associated with a cationic potential energy mismatch effect [18,63]. The dynamic structure model has been supported by results from both reverse Monte Carlo modelling [64] and molecular dynamics simulations [65].

The intermediate range order is particular relevant to ionic diffusion, as it is over these distances that the network modifiers interact and jump [17,18]. The structure resulting from the continuous random network theory (shown in Figure 2.1) provides a solution to the short-range order of glasses, but fails to predict the exact structural depolymerisation caused by network modifiers. Advances in both computational power and spectroscopic techniques have found evidence of intermediate structures which are not completely random [66,67]. The intermediate microstructure is characterised by segregation of modifying ions clustered within the network, creating channels of network modifying ions. The microstructure of modifying ions percolated in channels is known as the modified random network model, and rationalise the transport of the network modifying ions. As the network modifying ions are percolated in close proximity and forming a channel structure, both the jump distance and the energy difference between sites are minimized. The thermal energy required for channel hopping is thus much smaller than that for the network formers, enabling the high diffusivity of the network modifying ions [17]. At low concentrations of network modifier the ionic mobility will be governed by high energy jumps, but as the network modifier concentration increases towards the percolation threshold the activation energy of hopping decrease as conducting channels are established. An example of the modified random network structure is shown in Figure 2.2.

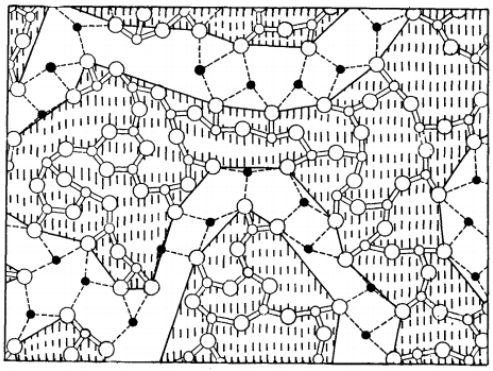

Figure 2.2: The structure of an oxide glass according to the modified random network theory. Covalent bonds are illustrated by solid lines and ionic bonds by dotted lines. The non-shaded regions highlight the percolation channels of high ion mobility [17].

An effect of the microsegregation of network modifier ions is that planes of low shear resistance arise when the concentration of modifier exceed the percolation threshold. One can thus argue that shear deformation is promoted by the hopping of network modifiers in the percolation channels, facilitating slipping between rigid parts of the network [36].

Since the properties of glasses are determined by their structure and topology, it is technically important to identify and potentially predict the structural arrangement. A combination of the modified random network and the dynamic structure model are, to a certain degree, able to predict and explain compositional property scaling in glass [16,68]. However, despite the vast amount of work on structure-property relations in glass, none of the existing models are able to account for the

compositional scaling of the dynamic properties. Hence, in the following sections the relation between chosen properties and structure characteristics will be elucidated. Focus will lie on compositional scaling during modifier substitution, as its non-linear deviations are the prime setback of existing models.

2.2. Density and Molar Volume

Density (ρ) is defined as the molecular mass per unit volume, and is normally an additive property. Meaning that, ρ normally exhibits linear compositional scaling, which from a structural perspective means that substitutes simply change places without interacting with the neighbouring environment. An example the compositional scaling of ρ is shown in Figure 2.3 where V_2O_5 is substituted for TeO_2.

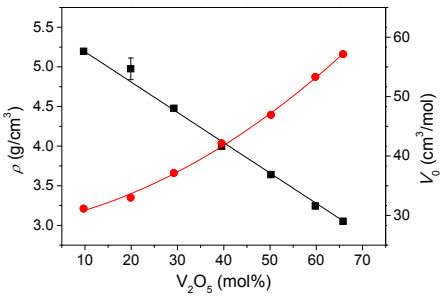

Figure 2.3: Room temperature density (ρ) and molar volume (V_0) as a function of composition in vanadium tellurite glasses. Solid lines are guides for the eyes. Data for the figure is reproduced from Paper I.

In vanadium tellurite glass, both vanadium and tellurium mainly exist in a trigonal bipyramidal configuration. Initially, as vanadium is put into the glass it will be surrounded exclusively by tellurium bipyramids. With further increase in the vanadium concentration the possibility of finding another vanadium bipyramid as next nearest neighbour increases, but the volume of the newly introduced vanadium trigonal pyramid remains the same, independent of the surroundings. The decrease in ρ with increasing V_2O_5 concentration (Figure 2.3) indicates a looser packing of the atoms since the molar weight of V_2O_5 is higher than that of TeO_2. The molar volume (V_0) is an indicator of the compactness of the network and is calculated as the molar mass divided by the density. Hence, both density and molar volume are often used as indicators of the resistance to further compaction. The increase in V_0 also implies that vanadia constitute a looser structural arrangement compared to TeO_2.

ρ is basically an interplay between two effects; (i) the weight of the individual ions, and (ii) the volume of the local environment around the ions. The mass of the structural units are determined from the periodic table and the total mass of the glass average that of its constituents. Each ion creates an environment suitable for itself, where the topology depends on the type and the field strength of the ion. High field strength ions (e.g. Na^+ and Mg^{2+}) tend to create compact environments where the oxygen anions are brought in close proximity, leading to a relatively dense

structure, whereas low field strength ions tend to create a relatively open network. Simplified, the individual ions are very similar to building blocks, each ion has its own weight and volume, independent of the configuration, and ρ is simply an average over its building blocks. The linear compositional scaling behaviour of ρ was acknowledged back in the 19th century where the first composition-density relations described linear dependence [69]. In most cases a linear composition-density relation is applicable, but there are special cases where linear compositional scaling is not applicable. An example is the mixed modifier effect. The mixed modifier effect can be separated in categories depending on the participating ions and we will focus mainly on three; (i) mixed alkali effect, (ii) the mixed alkali-alkaline earth effect, and (iii) the mixed alkaline earth effect. The simultaneous presences of two network modifiers give rise to non-additive variations in many properties, but density mostly remain unaffected [34].

Figure 2.4 shows three examples of the mixed modifier effect; the mixed alkali effect (Na/K), the mixed alkali-alkaline earth effect (Ca/Li), and the mixed alkaline earth effect (Mg/Ca). All three series are aluminosilicate glasses, and in Figure 2.4b) and c) all aluminium is charge balanced by sodium. In Figure 2.4a) the total aluminium concentration equals the combined concentration of sodium and potassium, meaning that sodium and potassium collaborate as charge balancer of the aluminium.

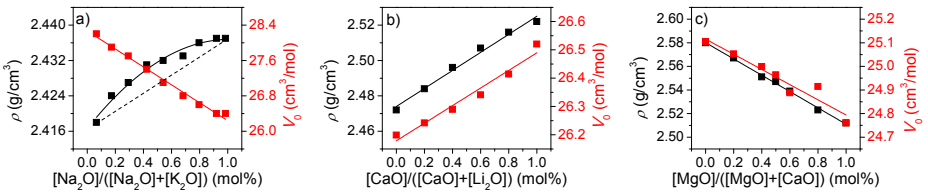

Figure 2.4: Room temperature density (ρ) and molar volume (V_0) as a function of composition in three series of aluminosilicate glass. a) illustrates the compositional scaling of ρ and V_0 in mixed alkali glasses, and b) and c) that in mixed alkali-alkaline earth and mixed alkaline earth glasses, respectively. Both solid and dashed lines are guides for the eyes. Data for the figure is reproduced from Papers II and III.

The densities of the glasses in the mixed Na/K series exhibit a positive deviation from linearity with the Na/K ratio, whereas densities of the glasses in the mixed Ca/Li and in the mixed Mg/Ca series scale linearly with composition (Figure 2.4). ρ is regarded as a static property and thus expected to scale linearly with the ratio of mixed modifier, unlike the dynamic properties such as viscosity and elastic moduli [34]. Both of which will be discussed in the following sections. The linear composition dependence of ρ observed for the mixed Ca/Li and mixed Mg/Ca series is in agreement with that reported for other mixed modifier silicate systems [35,70]. However, several studies of both mixed alkali silicate and aluminosilicate systems have shown a positive deviation from linearity in ρ, i.e., similar to the trend observed in Figure 2.4a) [60,71-75]. It is noteworthy that the observed positive deviation from linearity is not limited to mixed Na/K series, but applies to all mixed alkali systems whereas it does not apply to e.g. mixed alkaline earth systems [35,37,73,75]. It has been proposed that the positive deviation from linearity in ρ is linked to a tight-knit structure caused by pairs of dissimilar alkali ions [71]. The tight-knit structure, however, does not explain why some series do not exhibit this mixed alkali effect [70]. The positive deviation from linearity

must be directly linked to a compactness of the network when two types of alkali ions co-exist, but the origin of the structural compactness requires further investigation.

2.3. Dynamic Properties of Supercooled Liquids

The dynamic properties studied in the project include viscosity (η), liquid fragility index (m), and glass transition temperature (T_g). The viscosity of glass forming liquids exhibits a universal departure from Arrhenius behaviour which is perhaps the most important feature of liquids [5], and the viscosity-temperature relationship has thus been the focus of several models [76-78]. Mauro *et al.* [78] proposed a new and improved model, founded upon the temperature dependence of configurational entropy via the Adam–Gibbs equation of viscosity [76]. The model is able to account for the configurational entropy both at the high temperature limit (an issue with the Avramov-Milchev model [77]) and at the low temperature limit (an issue with the Vogel-Fulcher-Tammann model [79]). Another important feature is that all three fitting parameters of the model bear a physical meaning. The model is given by Eq. (1).

$$\log\eta(T) = \log\eta_\infty + (12-\log\eta_\infty)\frac{T_g}{T}\exp\left[\left(\frac{m}{12-\log\eta_\infty}-1\right)\left(\frac{T_g}{T}-1\right)\right] \quad (1)$$

where η_∞ is the high-temperature limit of liquid viscosity, T_g the glass transition temperature, and m the liquid fragility index. m is defined as the slope of an Angell plot at T_g (Eq. (2)) [5]. T_g is the temperature corresponding to $\eta = 10^{12}$ Pa s [80,81].

$$m \equiv \left.\frac{\partial(\log\eta(T))}{\partial(T_g/T)}\right|_{T=T_g} \quad (2)$$

According to studies of glass forming liquids, η_∞ is a universal value of 10^{-3} Pa s [82]. This leaves the Eq. (1) with only two fitting parameters, viz., T_g and m. By fitting Eq. (1) to experimental viscosity data both m and T_g are determined, and an example of this determination is shown in Figure 2.5.

Open network liquids like silicates show relatively low extent of Arrhenius variations of viscosity with temperatures at T_g, and are thus characterised as intermediate fragile liquids. Silica and Germania liquids are termed “strong” and experiences high resistance to structural changes caused by changing temperature. Glass forming liquids characterised by non-directional coulomb interactions or by van der Waals attractions belong to the other extremity. These liquids are termed “fragile” and have relatively high m values. The structure of these liquids rapidly collapses under thermal activation, and flocculate over a wide range of orientations and coordination states. The fragile liquids exhibit a strong non-Arrhenius viscous behaviour. Strong liquids typically experience smaller jumps in C_p at T_g ($\Delta C_p = C_{pl} - C_{pg}$ where C_{pl} and C_{pg} are the heat capacities of the glass forming liquid and that of the glass, respectively), whereas fragile liquids experience larger jumps [5]. The fragility determined via Eq. (2) is referred to as the kinetic or liquid fragility, whereas ΔC_p is a measure of the thermodynamic fragility. For many glass forming liquids the thermodynamic and the kinetic fragilities exhibit a linear relation [83,84]. Meaning that, differential scanning calorimetry (DSC) measurements can be used to determine changes in both liquid fragility and

structure [84]. Differentiation of Eq. (1) over T_g/T enables determination of the liquid fragility. It is well established that a linear relation exists between the DSC cooling rate (q_s) dependence of fictive temperature (T_f) and the temperature dependence of viscosity of the formed glass [85,86]. From this relation Eq. (3) is obtained.

$$\log\left(\frac{q}{q_s}\right) = m - m\frac{T_g}{T_f} \tag{3}$$

Figure 2.5 shows m values determined both by fitting the viscosity data to Eq. (1) and by fitting the q_s - T_f relation to Eq. (3), respectively.

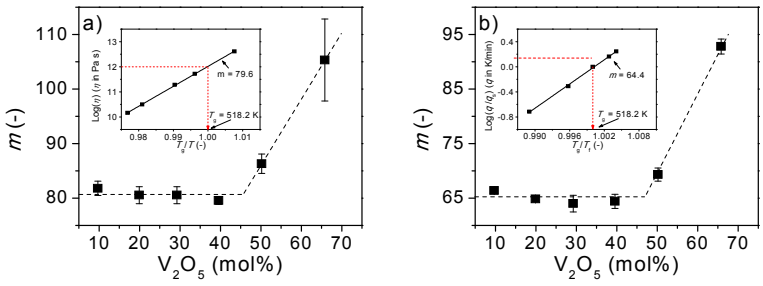

Figure 2.5: a) Liquid fragility index (m) as a function of the molar V_2O_5 concentration in binary vanadium tellurite glasses determined via Eq. (1). The dashed line is a guide for the eye showing the compositional scaling of m. Inset: Determination of m using Eq. (2) by taking the 40 mol% V_2O_5 glass as an example. Data for the figure is reproduced from Paper I. b) m as a function of the molar V_2O_5 concentration in binary vanadium tellurite glass determined via Eq. (3). The dashed line is a guide for the eye showing the compositional scaling of m. Inset: Determination of m using Eq. (3) by taking the 40 mol% V_2O_5 glass as an example.

As observed in Figure 2.5, the vanadium tellurite system exhibits an offset between the m-values determined from viscosity and by DSC, but both exhibit similar compositional scaling behaviour. Vanadium tellurite glasses contain both VO_4 and VO_5 [87], where V^{4+} primarily exists in tetragonally distorted octahedral coordination [88]. At low V_2O_5 concentrations, V^{5+} mainly exists in a trigonal bipyramidal configuration (~80%), but as the V_2O_5 concentration increases, the energetically preferred coordination geometry of V^{5+} changes. Going from a trigonal bipyramidal coordination configuration at low V_2O_5 concentrations, the preferred configuration changes to a 50/50 mixture of trigonal bipyramidal and tetrahedral sites at high V_2O_5 concentrations [89,90]. An increase in tetrahedral sites expands the glassy network (Figure 2.3) and consequently decreases the amount of bonds per unit volume. If all V^{4+} ions occupy tetragonally distorted octahedral sites, the fraction of distorted tetrahedral sites starts to drop at V_2O_5 = 45 mol%. If the V^{4+} ions contribute to more constraints than V^{5+}, the behaviour of m can be caused by structural changes in the coordination configuration of vanadia. When the fraction of tetragonal V^{4+} sites starts to decrease, the quantity of the most constrained network diminish, leading to a an increase in m.

The compositional dependence of T_g and m is an indirect measure of structural changes, and their scaling behaviour is thus predictable when sufficient structure data are available [91]. However, structure data are not always accessible and the structural origin of the mixed modifier effect remains unknown. Figure 2.6 shows three examples of the mixed modifier effect; the mixed alkali effect (Na/K), the mixed alkali-alkaline earth effect (Ca/Li), and the mixed alkaline earth effect (Mg/Ca). In all three cases both T_g and m exhibit non-linear compositional scaling.

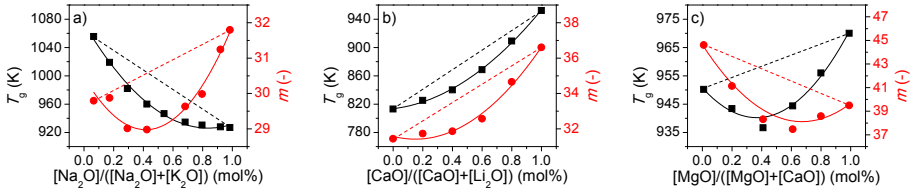

Figure 2.6: Liquid fragility index (m) and glass transition temperature (T_g) as a function of composition in three series of aluminosilicate glass. a) illustrates the compositional scaling of m and T_g in mixed alkali glasses, and b) and c) that in mixed alkali-alkaline earth and mixed alkaline earth glasses, respectively. Both solid and dashed lines are guides for the eyes. Data for the figure is reproduced from Papers II and III.

Neuville and Richet [92] explain the minima in viscosity by an excess of entropy caused by mixing. The proposed minima in viscosity are in contrast to the theory given by Dietzel [33]. Dietzel proposed that oxygen ions stabilized by two different ions are energetically much more favoured than oxygen ions stabilized by similar ions, which results in maxima in T_g. The observed minima in Figure 2.6 indicate the exact opposite, viz. that the mixed modifier compositions experience weaker bonding than the end-member compositions. Taking the mixed alkaline earth effect as an example (Figure 2.6c)), Raman and ^{27}Al MAS NMR analysis are plotted in Figure 2.7.

Raman spectra of the mixed Mg/Ca aluminosilicate glasses are shown in Figure 2.7a), where the Raman intensity is plotted as a function of wavenumber (ν). The two low wavenumber peaks are both unaffected by composition, i.e., stationary positioned at ~498 cm^{-1} and ~570 cm^{-1}, respectively. According to Galeener [94] these peaks are caused by Si–O–Si bending vibrations of three-fold and four-fold silica ring structures embedded in the glass network. The position of the high wavenumber band, ~1000 cm^{-1}, varies as magnesium is exchanged with calcium. According to McMillan [95], this band is associated with Si-O stretching vibrations of tetrahedral silicate units. The dashed line in Figure 2.7b) represents a linear relation between the end-member compositions. We find that the peak position diverges positively from a linear tendency, with the largest deviation found at [MgO]/[MgO]+[CaO]) = 0.63, indicating an increase in the amount of tetrahedrally connected silica units for the mixed network modifier glasses.

^{27}Al MAS NMR spectra of mixed Mg/Ca aluminosilicate glasses are shown in Figure 2.7c). The spectra all exhibit a narrow asymmetric peak centred at 50 ppm, consistent with tetrahedral aluminium groups (Al^{IV}) [96]. The aluminium speciation of these glasses is thus very similar to each other, since both position and shape of the ^{27}Al resonance exhibits only minor composition dependence. Only the spectrum of the magnesium end-member composition is slightly broader and more asymmetric on the more shielded side (lower shift), which is due to the presence of higher Al coordination in the sample, such as five-fold coordinated aluminium (Al^{V}).

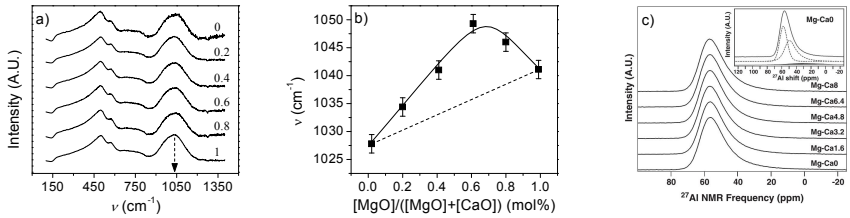

Figure 2.7: a) Raman spectra for the mixed Mg/Ca aluminosilicate glasses. The spectra are shifted vertically for clarity. The designation written on the right corresponds to a specific [MgO]/([MgO]+[CaO]) ratio. The arrow indicates the approximate peak positions, which in b) is plotted as a function of composition. b) Peak position wavenumber (ν) of the Raman peak near 1050 cm^{-1} as a function of the molar Mg/Ca ratio. The solid line represents the apparent relation between ν and the molar ratio of [MgO]/([MgO]+[CaO]), whereas the dashed line represents a linear relation between the end-member compositions. Both lines are guides for the eyes. c) ^{27}Al MAS NMR spectra for the six mixed Mg/Ca aluminosilicate glasses. The inset shows an example of deconvoluting these data into Al^{IV} (dashed lines) and Al^{V} peaks (filled area), allowing for an estimation of changes in Al coordination [93]. Multiple Al^{IV} resonances were required to account for the complex lineshape and are consistent with literature values for isotropic chemical shift and quadrupolar coupling product in sodium aluminosilicate and alkaline earth aluminosilicate glasses. The fitting parameters for the Al^{V} resonance match those used in Ref. [93]. Data for the figure is reproduced from Papers IV.

The high wavenumber vibration modes of Raman spectroscopy are associated with higher network connectivity because more energy is required to induce atomic vibrations (shifts in the Q^n-value of the tetrahedral SiO_4 units). Since the oxygen coordination number of Mg^{2+} is lower than that of Ca^{2+} [97-99], the number of affected oxygen ions in the SiO_4 network decreases when substituting Mg^{2+} for Ca^{2+}. A decrease in bonding oxygen ions thus explains why the concentration of T-O-T bonds (T = tetrahedral unit) increases as magnesium is substituted for calcium.

From the NMR data presented in Figure 2.7c), we conclude that AlO_4 tetrahedra in the calcium-containing glasses are essentially all charge-balanced by a combination of Na^+ and Ca^{2+}. These spectra can be satisfactorily simulated without the need for an Al^{V} resonance. However, in the composition where the Ca^{2+} concentration approaches zero, the need for alkaline earth cations (Mg^{2+}) to complement the role of Na^+ is partially ineffective, leading to a small population of Al^{V} species. In detail we find approximately 5% Al^{V} in the magnesium end-member composition compared to 0% in the remaining compositions. Such quantities of Al^{V} species are consistent with high quality fitting of ^{27}Al MAS NMR spectra in similar systems [92,93]. Changes in aluminium speciation in the mixed alkaline earth compositions are thus negligible. The slight increase in Al^{V} of the magnesium end-member composition contributes to the general trend, being that the magnesium end-member composition compared to the calcium end-member composition has higher T_g. Figure 2.7 thus shows that the mixed alkaline earth effect manifests itself as a maximum in T-O-T bonds and has no influence on the aluminium speciation.

The negative deviation from linearity in m is associated with higher network connectivity of the liquid. However, the viscosity at T_g of the mixed alkaline earth compositions is lower than that of the end-member compositions. Raman spectroscopic data suggest that the network connectivity of

the mixed Mg/Ca compositions is higher than that of the two end-members, which normally increases viscosity. Therefore we can infer that the decrease of viscosity is not related to the network connectivity, but instead is mainly related to the local structural environment around the network modifiers causing overall bond weakening, viz., the minimum in viscosity originates from the structural character of the modifying ions.

2.4. Elastic Moduli and Poisson's Ratio

Glasses are intrinsically isotropic solids due to their lack of long range atomic order. The isotropic behaviour of glass is most evident in their elastic properties as elastic properties are studied on a macroscopic scale. Glass has an elastic component and under stress it deforms elastically, i.e., non-plastically. The applied force that creates the stress can be applied e.g. uniaxial, transverse, or uniformly. Young's modulus (E) describes tensile elasticity, or the tendency to deform along an axis when opposing forces are applied along that axis. Shear modulus (G) describes the tendency to deform when acted upon by transverse forces, and bulk modulus (K) describes the volumetric elasticity, or the tendency to deform uniformly under volumetric stress. E, G, and K are as a group referred to as the elastic moduli [101]. Isotropic elastic materials, e.g., glass, have their elastic properties uniquely determined by any two of the three moduli. Thus, given any two parameters of the elastic moduli, the last can be calculated. Hence, only E and G have been measured and their compositional scaling as a function of the mixed modifier effect is shown in Figure 2.8.

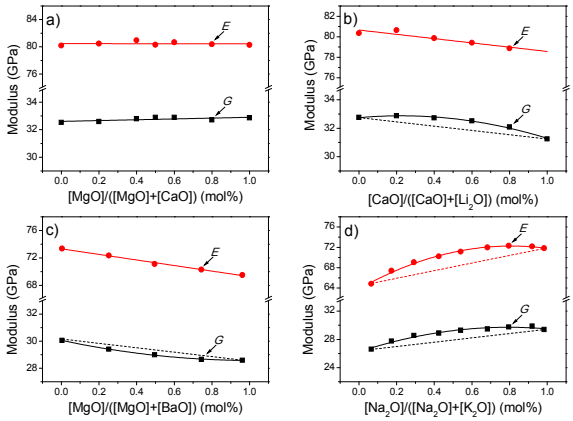

Figure 2.8: Young's modulus (E) and Shear modulus (G) as a function of composition in four series of aluminosilicate glass. a) illustrates the compositional scaling of E and G in mixed Mg/Ca glasses, b) the compositional scaling of E and G in mixed Ca/Li glasses, c) that in mixed Mg/Ba glasses, and d) that in mixed Na/K glasses. Both solid and dashed lines are guides for the eyes. Data for the figure is reproduced from Papers II, IV, and V.

Elastic moduli give a macroscopic view of a material's resistance to elastic deformation and reflect both the interatomic bonding energies and the connectivity of the network. Elastic moduli are therefore particularly helpful in correlating structural changes to compositional property scaling

[101]. As elastic moduli, hence also E, is closely related to structure, several models have been proposed to predict E from composition. The most widely used model is that proposed by Makishima *et al.* [102] which expresses E as a function of the volume density of energy and the packing density. The volume density of energy is calculated from the dissociation energies of the different oxides, and the packing density from composition and density. The theoretical prediction of E is in silicates in good agreement with experiments, but in phosphates and borates E is greatly overestimated. In phosphates, the overestimation is due to the presence of double bonded oxygen ions on phosphate, which does not contribute to the network stiffness and the bond energy of the double bond should thus be subtracted from the dissociation energy of P_2O_5. In borates, the overestimation originates from relatively weak bonds between borate in planar BO_3 triangle coordination. Within the same glass family, a general rule of higher elastic moduli when substituting for higher field strength modifying ions exist [103,104]. This rule of thumb, however, does not apply to substitutions involving either magnesium or lithium.

An elastic moduli-field strength relation is consistent with the results shown in Figure 2.8d) as sodium has higher field strength than potassium. The anomalies caused by Mg^{2+} and Li^{+} are explainable by collaboration between highly compressible Q^4 species and clusters of modifying ions [103]. Further structure studies are required to verify why a relatively high field strength ion like magnesium is causing lower degrees of polymerisation compared to other alkaline earth ions. As the results presented in Figure 2.8 cannot be explained by simple connectivity theory, they indicate that the structural changes accompanied by the mixed modifier effect are not limited only to modifier-modifier interactions, but include changes in the framework connectivity of the glass. The elastic moduli exhibit linearity, positive- and negative deviations from linearity. Hence, we recognize that existing theoretical models concerning the elastic moduli do not provide significant insight into the structural details of the mixed modifier effect.

2.4.1. Poisson's ratio

Determination of elastic moduli is a prerequisite to calculate the Poisson's ratio (v), where v is defined as the negative ratio of transverse to axial strain. When a glass is compressed in one dimension it expands in the two dimensions perpendicular to the dimension of compression. v is the fraction of expansion divided by the fraction of compression and can be calculated via Eq. (4) [105]:

$$v = \frac{E}{2G} - 1 \tag{4}$$

Glasses have v-values of ~0.3 depending on the structure and the density of cross linking [106]. As v is proportional to E/G it reveals something about the ratio between the ability of the glass to resist densification and the ability of the glass to resist shear, and is thus useful when predicting deformation processes under indentation. A subject discussed in detail in chapter 4. Figure 2.9 shows calculated v-values of the mixed Mg/Ba glasses presented in Figure 2.8c).

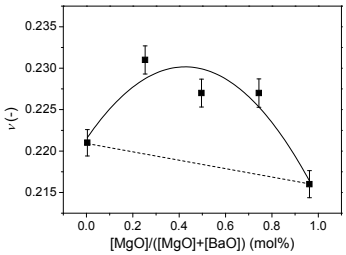

Figure 2.9: Poisson's ratio (v) as a function of composition in a series of mixed Mg/Ba aluminosilicate glasses. Both solid and dashed lines are guides for the eyes. Data for the figure is reproduced from Paper V.

The negative deviation from linearity observed in G (Figure 2.8c)) is responsible for the positive deviation from linearity of v observed in Figure 2.9, as v and G are negatively related via Eq. (4). The relative increase in v of the mixed Mg/Ba glasses compared to the end-member compositions corresponds to a smaller degree of shear, which is in good agreement with viscosity measurements of the series, as T_g goes through a minima at roughly [MgO] = [BaO]. It should be stressed that a correlation between T_g and v is not a universal trend.

2.5. Summary

By comparison between Figure 2.6Figure 2.8 we realise that the structural trademark of the mixed modifier effect, which results in universal negative deviations from linearity in T_g and m, is not encountered in measurements of E and G. The mixed modifier effect always manifests itself as negative deviations from linearity in T_g and m, while the effect on E, G and v can be both negative, positive or linear. As both T_g and m are measures of viscosity their compositional scaling may be a result of structural or topological changes occurring on a microscopic level. Meaning that, the glass is able to follow the path of least resistance and shear via bonds of relatively low energy, i.e., via ionic bonds percolated in channels. E and G are both macroscopic properties, as their measurements involve constrained movement of the glass entity. The network formers of the glass are thus forced to budge, facilitating movement via the strongest bonds of the network. The mixed modifier effect universally shows a weakening in the overall bond strength in the vicinity of the network modifying ions, while the effect on the network formers is not universal and varies with ion pairs.

The mixed modifier effect on ρ is only evident in the mixed alkali case, where a positive deviation from linearity is observed. We propose the positive deviation from linearity in ρ is directly linked to a compactness of the network structure which is also responsible for the positive deviation from linearity in E. The origin of the structural compactness is not experimentally verified, but we suggest the presence of a tight-knit structure only occurring for mixed alkali compositions and not e.g. mixed alkaline earth compositions.

In the mixed network former system, i.e., the vanadium tellurite glasses (glasses with no network modifier ions), we find a strong link between structure, composition, and the resulting properties. The link is evident in the direct structural dependencies of density, liquid fragility, and hardness. The compositional scaling of hardness is discussed in detail in the following chapter.

3. Mixed Modifier and Mixed Network Former Effects on Hardness

In order to investigate the link between Vickers hardness and properties related to structural rearrangement (e.g. Poisson's ratio, liquid fragility and elastic moduli) it is important to obtain a fundamental understanding of the definition and applicability of Vickers hardness. Therefore, we start by reviewing Vickers hardness and then look at both mixed modifier effects on hardness and mixed network former effects on hardness. We give universal explanations for the observed mixed modifier effects and mixed network former effects on hardness and couple the explanation to the compositional scaling of viscosity, liquid fragility, and density. The composition-hardness correlation is a main focus of Papers I and IV.

3.1. Vickers Hardness: Definition and Implementation

Glass exhibit permanent deformation when subjected to indentation under sharp contact loading, e.g., Vickers indentation. Indentation tests are simple and a useful technique to evaluate mechanical properties of glass [107]. Hardness is defined as the applied load divided by the projected area of the deformed region, and is the measure of the ability of the glass to resist permanent deformation. Understanding and predicting the compositional dependence of glass hardness is important for many applications, such as construction materials for architectural purposes [47] and scratch-resistant glass covers for personal electronic devices [46].

The process of indentation involves both compression and shear. If the load is low, the deformation is within the elastic limit, and upon unloading the glass relaxes to its original shape. Beyond the elastic limit, the glass deforms by a permanent densification due to hydrostatic stress and a plastic deformation due to shear caused by excess stress. At even higher loads, cracks initiate and enable measurements of fracture toughness [108]. The size of the permanent indents is generally in microns and the hardness value is therefore referred to as microhardness. The normal hardness scale in glass is that of Vickers, where the hardness (H_v) is defined as in Eq. (5):

$$H_v = \frac{2P\sin(\frac{1}{2}\theta)}{d^2} \tag{5}$$

P is applied load, θ the angle between the indent tip and the glass (136°), and d the diagonal length of the indent [105]. As seen in Eq. (5) Vickers hardness is directly related to the size of the indent, but not to the time of indentation. The diagonal, d, is obtained after unloading, and as the elastic part of the indent relaxes upon pressure removal, d becomes slightly shorter. The ratio of elastic deformation to total deformation under indentation is higher at lower loads and results in the so-called "indentation size effect", where hardness is overestimated at low loads [109,110]. As the elastic behavior of glass below the elastic limit is largely dependent on the elastic properties of the glass, consecutive cycles of loading and unloading can be employed to determine both the elastic limit and E [111]. In forthcoming sections E is therefore used to represent the amount of elastic deformation occurring under indentation.

As the indenter is pressing into the glass, an area of increased density is created beneath the indenter. The size of the indent will keep growing until equilibrium exists between the resistance to further densification and the applied load. The time required to establish this equilibrium is

measured in days whereas measurement times normally are couple of seconds. The time of indentation is not presented in Eq. (5), but for comparison of H_v values, a constant pressing time is important.

In order to achieve reproducible and comparable hardness values, loads above the elastic limit are recommended. However, the applied force should be below the required force for crack initiation, as to avoid the creation of cracks around the indent. As cracks are created, the stress concentrates at the tip of the crack, and the energy converted by crack propagation is not contributing to the creation of a permanent indent. Meaning that, cracks convert energy which results in smaller indents volumes and thus erroneously high hardness values.

3.2. Mixed Alkali Effect

The composition dependences of H_v for two aluminosilicate glasses series are shown in Figure 3.1. The two mixed sodium-potassium aluminosilicate glass series are standard aluminosilicate glass (SiO_2-Al_2O_3-MgO-Na_2O/K_2O) and soda lime float glass (SiO_2-Al_2O_3-MgO-CaO-Na_2O/K_2O) compositions. The standard aluminosilicate series contains relatively high concentration of alumina (>10 mol%, AS series), whereas the float glass series contains considerable less alumina (<2 mol%, S series). Both series exhibit an initial increase followed by a decrease of H_v with increasing Na/K ratio, i.e., a mixed alkali effect of hardness. The largest positive deviation from linearity and the maximum value of H_v are observed at around $[Na_2O] = [K_2O]$. The overall trend shows that glasses from the AS series are harder than those from the S series. As the total alkali concentration is kept constant and above the concentration of alumina, all alumina is charge compensated by alkali ions, leaving less alkali ions to create NBO's.

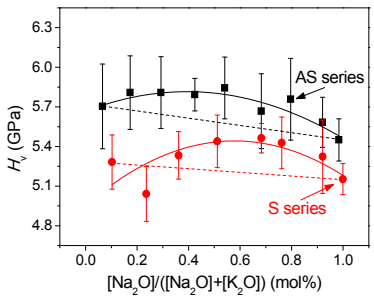

Figure 3.1: Vickers hardness (H_v) as a function of the molar ratio of sodium to total alkali content in two mixed Na/K aluminosilicate series. The solid lines represent the compositional scaling of H_v, whereas the dashed lines depict a linear relation between the two end-member compositions. Both lines are guides for the eyes. Compositions depicted by squares are from a high-alumina series (AS), while compositions depicted by circles are from a low-alumina series (S). Data for the figure is reproduced from Paper III.

The observed maximum in hardness of the mixed alkali compositions is in good agreement with literature, where a positive deviation from linearity have been shown for several mixed alkali compositions [32,34-36]. Ainsworth [112] measured a positive deviation from linearity in hardness for mixed alkali compositions back in 1954, but until now no universal theory have been able to

describe his observations. The positive deviation from linearity in hardness is probably related to the positive deviation from linearity found in ρ, as a more closely packed structure infers both higher density and higher hardness [101]. Dietzel [33] proposed that oxygen ions stabilized by two different network modifying ions are energetically more favored than oxygen ions stabilized by similar ions, thus creating stronger bonding and higher hardness. In density, the observed effect is rather small because the contraction of the coordination sphere around the stronger field strength network modifier is balanced by an extension of the coordination sphere of the lower field strength network modifying ion. In order to have a positive deviation in ρ and H_v the coordination sphere of Na^+ must contract more than the coordination sphere of K^+ is able to accommodate, resulting in a denser structure.

3.3. Mixed Alkaline Earth Effect

Figure 3.2 shows Vickers hardness plotted as a function of the molar ratio of magnesium to total alkaline earth content. The dashed line represents a linear relationship between the end-member compositions. A parabolic fit matches data, and the largest deviation from linearity is found at a substitution degree of 0.5. Both series are aluminosilicates, where the alkali concentration equals the aluminium concentration.

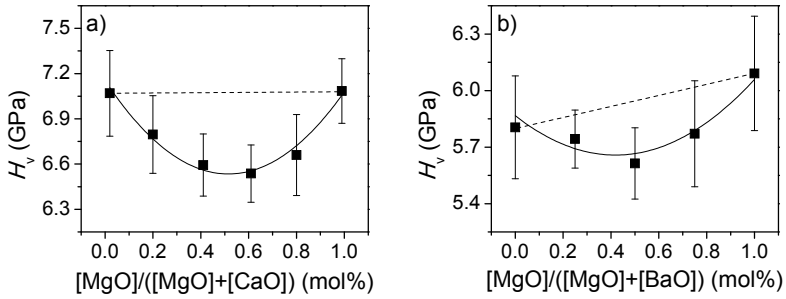

Figure 3.2: Vickers hardness (H_v) as a function of composition in (a) mixed Mg/Ca and (b) mixed Mg/Ba aluminosilicate glass series. The solid line represents the apparent relation between H_v and composition, whereas the dashed line is a linear extrapolation between the end-member compositions. Both lines are guides for the eyes. Data for the figure is reproduced from Papers IV and V.

The theory by Dietzel [33] implies that oxygen ions stabilized by two different alkaline earth ions are energetically much more favored than oxygen ions stabilized by similar alkaline earth ions, which results in a maximum in Vickers hardness. The observed minimum in Vickers hardness indicates the opposite, viz., the mixed Mg/Ca and mixed Mg/Ba compositions experience weaker bonding than the end-member compositions. If viscosity is linked the resistance to indentation, we suggest that the occurrence of the minimum in hardness is associated with the corresponding minimum in isokom temperatures (Figure 2.6). Despite the deformation under indentation and the viscous flow under shear occur at various temperature regions, their mechanisms are similar to large extents, i.e., both are related to the translational motion of structural units. It can be argued that the responsible underlying topological constraints of the mechanisms may differ, due to the temperature

dependence of these constraints. If this is the case, an offset might occur between the minima in Vickers hardness and isokom temperatures at room-temperature [113].

The composition dependence of H_v of oxide glasses with varying alkaline earth ratio has been reported in the literature as a positive deviation from linearity with a maximum deviation at the ratio of about 1:1 [35,114-116]. To the best knowledge of the author, we are first to report a minimum in H_v for mixed alkaline earth compositions.

3.4. Mixed Alkali-Alkaline Earth Effect

The composition dependences of H_v is plotted in Figure 3.3. The nominal compositions of the studied mixed alkali-alkaline earth aluminosilicate glasses are 60SiO2-16Al2O3-16Na2O-(8-*y*)Li2O-*y*CaO where $y = \{0, 1.6, 3.2, 4.8, 6.4, 8\}$. H_v exhibits a minimum value (i.e. largest mixed alkali-alkaline earth effect) at the substitution degree of 0.5.

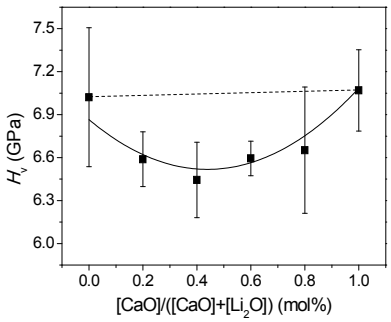

Figure 3.3: Composition dependence of Vickers hardness (H_v) for a mixed Ca/Li aluminosilicate glass series. Solid lines represent the apparent relation, whereas dashed lines are linear extrapolations between end-member compositions, both intended as guides for the eyes. Data for the figure is reproduced from Paper II.

In a systematic investigation of glass properties and their dependence of the mixed alkali-alkaline earth effect (i.e. when both alkali and alkaline earth ions co-exist), Byun *et al.* [48] conclude that no simple mechanism can be responsible for the observed nonlinearities in the mechanic properties. Moreover, they point out that the deviation from linearity must be intimately connected with microscopic structural changes. Hence, in order to reveal the origin of the negative deviation from linearity, the accompanying structural changes must be known. Greene [117] investigated the mixed Ba/K effect in three borosilicate and three aluminosilicate glass series and found linear compositional scaling of H_v in all series. The linear tendencies are explained by differences in the field strength of the two modifier ions, but no mixing effect was observed.

To the best knowledge of the author, there are no reports on a minimum in mechanic properties for mixed alkali-alkaline earth compositions. However, the measured minimum in H_v can be explained by similar considerations as for the mixed alkaline earth effect, i.e., via the minimum in isokom temperatures and viscosity (Figure 2.6).

From a structural perspective, the mixed alkali-alkaline earth effect is qualitatively similar to the mixed alkaline earth effect and not to the mixed alkali effect. As ρ is linear for both mixed alkali-alkaline earth and the alkaline earth glasses, the minimum in H_v indicate that the presence of just one alkaline earth ion in any mixed modifier system strongly reduces the overall bonding strength. As discussed in section 2.3, in mixed alkaline earth glasses we observe an increase in the amount of T-O-T bonds, and explained the negative deviation from linearity in H_v via relative weak bonds located around the network modifying ions. The same explanation is applicable for the mixed alkali-alkaline earth effect.

3.5. Mixed Network Former Effect

A series of V_2O_5-TeO_2 glasses with varying vanadia content were synthesized via the melt quenching technique. The H_v values are plotted in Figure 3.4a) as a function of V_2O_5 concentration. H_v remains constant when V_2O_5 increases from 10 to 45 mol%, followed by a linear decrease with further increasing the concentration of V_2O_5 from 45 to 65 mol%. The observed trend is in contrast to the trend reported in literature [118,119], viz., a continuous decrease in H_v with increase in vanadia concentration. The compositional behaviour of H_v strongly resembles that of the redox state of the vanadium ions (Figure 3.4b)), i.e., an initial plateau followed by a decrease with further increase in V_2O_5 concentration.

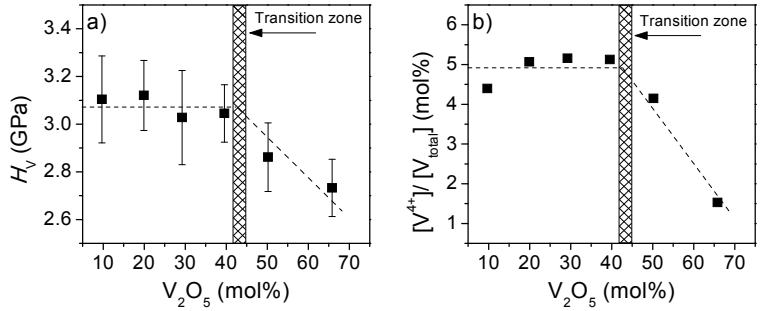

Figure 3.4: a) Vickers hardness (H_v) and b) redox ratio of vanadium ($[V^{4+}]/[V_{total}]$) as a function of V_2O_5 in binary V_2O_5-TeO_2 glass. The concentration of V^{4+} was determined by electronic spin resonance (ESR) and the total concentration of vanadium (V_{total}) determined by energy dispersive X-ray spectroscopy (EDX). The dashed line represents the compositional scaling and is a guide for the eyes. The transition zone is where abrupt changes in the compositional scalings occur. Data for the figure is reproduced from Paper I.

As mentioned in section 2.2, an increase in V^{4+} sites expands the glass network and consequently decreases the amount of bonds per unit volume. If the V^{4+} ions contribute to more constraints than V^{5+}, the behaviour of c ($c = [V^{4+}]/[V_{total}]$, where $[V_{total}]$ is the total concentration of vanadium) might be the reason for the transition zone at about V_2O_5 = 45 mol% observed in both m (Figure 2.5) and H_v (Figure 3.4a)). When the fraction of tetragonal V^{4+} sites starts to decrease, the quantity of the most constrained network diminish, leading to a decrease in H_v and an increase in m. Sharma *et al*. [118] measured H_v and c of vanadium phosphate, vanadium tellurite and vanadium borate glasses and found that in each system the c value decreases with increase in vanadia concentration,

almost parallel to a 1:1 decrease in H_v. We therefore propose that c, which is related to the structure of the glass, is strongly linked to the physical and dynamic properties of the glass. For three different vanadium systems, an approximately 1:1 correlation between H_v, m and c is found.

3.6. Summary

The mixed modifier effect on H_v manifest itself as positive deviations from linearity for the mixed alkali glass, whereas it results in negative deviations from linearity for both mixed alkali-alkaline earth and mixed alkaline earth glasses. These results indicate that the theory proposed by Dietzel, suggesting increased bond strength when to different modifier ions are in close proximity is only valid in the mixed alkali case and not in general. The observed negative deviations from linearity in H_v observed for both the mixed alkali-alkaline earth effect and the mixed alkaline earth effect are explained by a viscosity decrease caused by a decrease in the overall bonding strength surrounding the network modifiers. The direct viscosity-hardness link is inconsistent with the positive deviation from linearity observed in H_v for the mixed alkali effect, as the mixed Na/K series also experiences negative deviations from linearity in viscosity and isokom temperatures. The mixed alkali effect manifests itself as a positive deviation from linearity in ρ, and the increased hardness can be explained by the effect of increased density exceeding the effect of decreased viscosity. The exact cause of the positive mixed alkali effect on hardness is discussed in further detail in chapter 4.

The tendency in H_v observed for the mixed V_2O_5-TeO_2 series is explained from a structure perspective and correlates well with the valence state ratio of vanadium (c). We propose that c is strongly linked to the physical and dynamic properties of the glass and can be directly correlated to changes in both H_v and m.

4. Impact of Chemical Composition on Indentation Processes

In order to clarify the impact of chemical composition, and hence the structure dependence on deformation processes under indentation, it is important to obtain a fundamental understanding of the deformation processes under indentation. Therefore, we start by reviewing indentation deformation processes and then look at the mixed modifier effects on the indentation processes and hardness. We discuss the origin of the different deformation processes under indentation and give explanations for their compositional scaling. We discuss their influence on hardness and link the compositional scaling to other properties, such as viscosity, density, and elastic moduli. The origin of the different deformation processes and their influence on hardness is one of the main focus points of Papers II, III, and V.

4.1. Deformation Processes during Indentation

The study of indentation deformation processes originated in 1962 when Hillig [120] discovered that no single operative process was responsible for the deformation under indentation. Deformation under indentation was initially proposed to obey the law of classical plasticity, i.e., indentation was perceived as a purely plastic process [121,122]. Later, via volume comparison between indent volumes and pile-up volumes, it was shown that the deformation occurred via two processes; (i) one related to plasticity and (ii) one involving densification [123-125]. Neely and Mackenzie [126] found that a portion of the densified volume was recoverable by sub-T_g annealing, and proposed that the permanent deformation was related to a density equilibrium. Nowadays, we widely accept glass as an intrinsically brittle material which deforms both plastically and via densification.

According to Yamane and Mackenzie [105], the resistance of a glass to deformation is a result of three distinct deformation processes: plastic flow, densification, and elastic deformation. Plastic (or shear) flow is a volume conservative displacement of matter, while densification is a non-volume conservative irreversible compression that creates a hemispherical area of increased density beneath the indentation, and elastic deformation a reversible compression that recovers after unloading. Another set of terminology has been proposed by Varshneya *et al.* [127], separating the deformation into two distinct processes (hydrostatic and deviatoric) each with an elastic component. Yoshida *et al.* [116] proposed a method to quantify the recoverable part of the indent volume (i.e., densified volume), which in turn provides an indirect measure of the plastic flow. Several studies have applied this method to investigate the link between densification and plastic deformation in borates, phosphates, and silicates, but simultaneous measurements of deformation volumes and Vickers hardness have been performed in only a few studies [108,128-131]. All of which are inconclusive on the relation between the deformation processes and hardness.

The method proposed by Yoshida *et al.* [116] is capable of quantifying the amount of non-plasticity in glass, and applies sub-T_g annealing to quantify the densification part and the plastic flow part. Walls *et al.* [132] reported that the magnitudes of the volumes systematically varied depending on the definition of the zero-level surface. We define the original surface as the zero-level surface and all material above zero-level is pile-up and all missing material under zero-level is indent volume. Atomic force microscopy (AFM) measurements are employed to determine the size of the indents and the amount of pile-up both before and after sub-T_g annealing at $0.9 \times T_g$ (in K). From these

measurements, the volume of densification (V_d) and the volume of plastic flow (V_p) are calculated as per Eqs. (6) and (7) [116]:

$$V_d = (V_i^- - V_a^-) + (V_a^+ - V_i^+) \tag{6}$$

$$V_p = V_i^- - ((V_i^- - V_a^-) + (V_a^+ - V_i^+)) \tag{7}$$

where subscripts *i* and *a* indicate initial volumes and volumes after annealing, respectively, and superscripts - and + indicate indentation volumes and pile-up volumes, respectively. Examples of the AFM images used to quantify V_d and V_p are shown in Figure 4.1.

Based on the AFM determinations of the size of the indent and the amount of pile-up the volume recovery (V_R) can be calculated per Eq. (8):

$$V_R = \frac{V_d}{V_i^-} = \frac{(V_i^- - V_a^-) + (V_a^+ - V_a^-)}{V_i^-} \tag{8}$$

V_R is defined as the ratio of the recovered volume during annealing relative to the initial volume of the indentation, i.e., the ratio of the densified volume relative to the initial indent volume. V_R shows a remarkably good correlation to *v*, why *v* is a suitable parameter to predict the densification ratio of indentation, and via Eq. (7) also the plastic flow ratio of indentation.

It is worth noting that the ratio of densification and the ratio of plastic flow under indentation both are load dependent. The load dependence is explained by a difference in the activation energy of the atomic bonds which are activated during the specific deformation process. That is, at a certain loads, certain atomic bonds are activated and the resulting deformation mechanism is a result hereof. As a rule of thumb the mechanisms responsible for the deformations are: bond bending and stretching for elastic deformation, bond breaking around network modifying ions or planes of low shear resistance for plastic flow, and bond breaking around the network formers for densification. As a result hereof the activation energies of the deformation processes are in ascending order: $E_{\text{elastic deformation}} < E_{\text{plastic flow}} < E_{\text{densification}}$. Meaning that at low loads, elastic deformation is favoured, while at high loads, plastic flow and densification is favoured. The deformation processes load dependence is supported by V_R measurements, as amorphous silica (pure network former glass) has a $V_R > 90\%$, while bulk metallic glass (pure network modifier glass) has a $V_R < 5\%$, i.e., >95% plastic flow [116,133].

The pile-up volume for all the glasses increased after annealing ($V_i^+ < V_a^+$). This increase originates from recovery of the densified zone as it extends to regions beyond that of the indent. Hence, both the changes in pile-up and in indent volume are assumed to constitute the densified volume. Three arguments support the assumption that the recovered volume corresponds to the volume of densification: (i) the activation energy of volume recovery is at $0.9 \times T_g$ approximately one order of magnitude lower than that of viscous flow [122,126,134]. (ii) plastic deformation do not result in a driving force for volume recovery [116]. (iii) 99% of the original volume of hydrostatically densified silica glass can be recovered and as silica glass contains no network modifiers the deformation originate solitary from densification [133]. Whether $0.9 \times T_g$ is sufficient to fully relax

and recover the densified volume is a dilemma, but 0.9xT_g is supported by Mackenzie [133] who showed that silica glass fully recovered after annealing for 1 h at approximately 0.9xT_g.

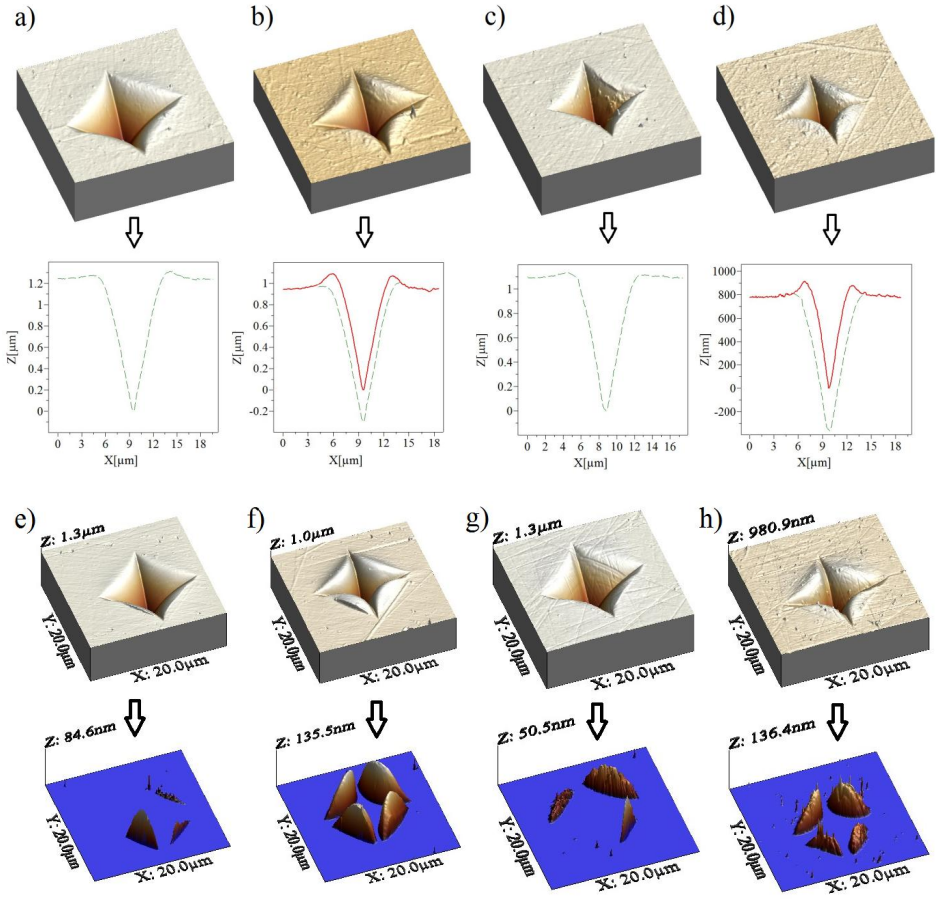

Figure 4.1: Atomic force microscopy (AFM) images of indents and their respective pile-up and cross-section. Material above the surface plane is assigned as pile-up and cross-sections are defined at the narrowest diagonal of the indent. Images a) and b) are obtained for the sample with [MgO]/([MgO]+[BaO]) = 0 before and after annealing at 0.9×T_g (in K), respectively. Images c) and d) are for the sample with [MgO]/([MgO]+[BaO]) = 1 before and after annealing at 0.9×T_g, respectively. Images e) and f) are [Na_2O]/([Na_2O]+[K_2O]) = 0 before and after annealing at 0.9×T_g, respectively. Images g) and h) are [Na_2O]/([Na_2O]+[K_2O]) = 1 before and after annealing at 0.9×T_g, respectively. The dashed lines represent the initial volumes (V_i) and the solid lines indicate the indent volumes after annealing. Data for the figure is reproduced from Papers III and V.

The resistance of a glass to permanent deformation (i.e., Vickers's hardness) is typically dominated by one of the three deformation processes, e.g., in silica glass densification is the dominant

deformation process. In the following sections we will discuss the role of each deformation process in determining hardness and the compositional dependence of hardness on each deformation process.

4.2. Elastic Deformation

Under an applied pressure, the atomic bonds in the glass stretch and bend away from their favorable position, allowing for some elastic deformation. Upon unloading, the bonds return to the state of lowest energy and the material recovers to its original shape. In other words, part of external mechanical energy (given by indentation) causes elastic work in the glass, which in turn leads to an increase of the potential energy of the atoms. When unloading, this increased potential energy is released, resulting in an expansion work. The rest of the mechanical energy causes plastic flow (i.e., a sort of deformation work), permanent densification (a permanent high potential state) and a small amount of dissipation heat. As hardness is calculated as the applied force divided by the indent size, part of the energy which is used for the elastic deformation does not contribute to the glass hardness. Meaning that, the more elastic deformation the glass experiences under indentation, the smaller the permanent indent size become resulting in erroneously high hardness values. As the elastic component of indentation is load dependent until the elastic limit is reached [135,136], indentation hardness is also load dependent up until the elastic limit.

The resistance of the elastic part of the deformation process is not accessed in the approach proposed by Yoshida *et al.* [116]. In order to enable prediction of the compositional dependence on hardness, it is important to account for all three deformation processes and the elastic part is thus equally important. Makishima and Mackenzie wrote in 1973 that the hardness of glass is closely related to the Young's modulus [102]. E is a measure of a materials resistance to axial stress under circumstances where plastic flow is prohibited. The molecular movement is consequently similar to that of elastic deformation and E therefore correlates well with the elastic part of indentation, and under certain circumstances, well with hardness. Hand and Tadjiev [35] proposed a direct one-to-one relation between E and H_v, and found that increasing hardness usually correlated with increasing modulus. However, this one-to-one correlation between E and H_v is not universal amongst glass series, which is realised in Figure 4.2.

Figure 4.2 shows the relation between E and H_v for four mixed modifier glass series. Figure 4.2a) shows H_v and E for a SiO_2-Al_2O_3-MgO-Na_2O/K_2O series, b) for a 60SiO_2-16Al_2O_3-16Na_2O-8MgO/CaO series, c) for a 60SiO_2-16Al_2O_3-16Na_2O-8Li_2O/CaO series, and d) for a 64SiO_2-12Al_2O_3-6B_2O_3-12Na_2O-6MgO/BaO series. All indentation experiments are performed with an indentation load of 0.49 N and an indentation time of 10 s, facilitating comparison between the series. The mixed Mg/Ba series was particularly designed, via the theory proposed by Kirchheim [43], to experience a large difference in E between the end-member compositions. If H_v was largely dependent on E, the compositional scaling of E is imposed on H_v, and H_v and E experience similar compositional scaling. With increasing difference in E between end-member compositions, a possible correlation between H_v and E is more evident. Figure 4.2 shows that no universal correlation between H_v and E exist. A mixed modifier effect (i.e., deviations from linearity) is observed in H_v for all glass series, whereas it is only observed in E for the mixed Na/K series. An effect of increased H_v due to increased E might be superimposed on a mixed modifier effect in

Figure 4.2d). However, as H_v is increasing in Figure 4.2c), while E is decreasing, any direct correlation between E and H_v is discarded. The positive deviation from linearity in H_v for the mixed Na/K series is closely related to the similar deviation observed in ρ (Figure 2.4a)), and the positive deviation in H_v presumably relates to the deviations in ρ and not in E. The non-direct relation is also visualised by comparison between the end-member compositions, as E increases while H_v decreases with increase in [Na_2O].

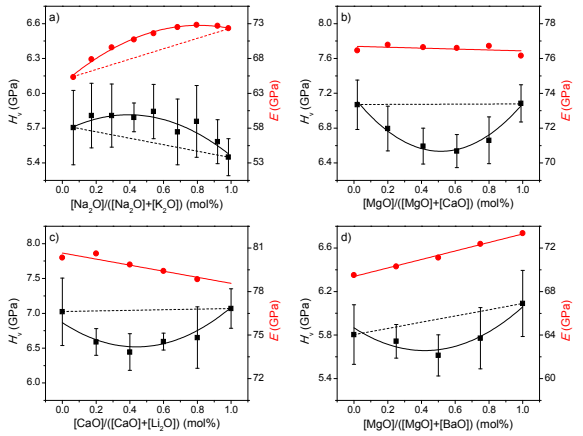

Figure 4.2: Young's modulus (E) and Vickers hardness (H_v) as a function of composition in mixed modifier silicate glasses. Solid lines represent the apparent relation, whereas dashed lines are linear extrapolations between end-member compositions, both intended as guides for the eyes. Data for the figure is reproduced from Papers II-V.

Yamane and Mackenzie [105] have reported that the resistance of glass to elastic deformation is proportional to K. The resistances to plastic flow and densification are proportional to αG and $(\alpha GK)^{½}$, respectively. α is a constant related to bond strength, G is shear modulus, and K is bulk modulus. Since glass is isotropic, E and K are proportional so according to the theory proposed in Ref. [105] the resistance to elastic deformation is proportional to E. If elastic deformation was the determining factor for hardness, we expect an almost direct one-to-one relation between E and H_v. As seen in Figure 4.2 a direct one-to-one relation between E and H_v is not the case.

In four mixed modifier silicate glass series we find no correlation between H_v and E. As the amount of elastic deformation under indentation is closely related to E, we propose that elastic deformation is not the determining deformation mechanism when predicting hardness in mixed modifier glass.

4.3. Densification

Since glasses are regarded as linear elastic materials, the physics of permanent deformation of glass under indentation at ambient temperature is particular intriguing for two reasons [122]; (i) classical plasticity is not expected as glasses lack long range order at the atomic scale. (ii) viscous flow under ambient temperatures requires absurd time scales for observation. Nevertheless, direct evidence of

plastic flow under indentation at ambient temperatures has been shown in several occasions [128,129,131,137].

The first response of a glass upon indentation is immediate elastic sinking of the original surface. In a secondary stage, an irreversible microscopic deformation occurs, aiming at relaxing the contact stress by increasing the density in a zone near the indenter tip. The area of the affected zone beneath the indenter can be approximated using an elastic stress field and is of hemispherical shape.

Via Eqs. (6) and (7) measurements of deformation volumes were conducted on three aluminosilicate glass series. Measurements were performed in tapping mode at 50% relative humidity and room temperature. The AFM cantilever had a silicon tip, the scanning frequency was 0.47 Hz, and the scan size was 20 x 20 μm^2. Following the procedure proposed by Yoshida *et al.* [116], at least ten indentations were examined before and after annealing for 2 h at 0.9*T*g (in K) of the respective composition. AFM images of chosen indents are shown in Figure 4.1. The resulting volumes of densification are plotted in Figure 4.3 together with the respective hardness value. Figure 4.3a) shows V_d and H_v for a $64SiO_2$-$12Al_2O_3$-$6B_2O_3$-$12Na_2O$-6MgO/BaO series, b) for a SiO_2-Al_2O_3-MgO-Na_2O/K_2O series, and c) for a $60SiO_2$-$16Al_2O_3$-$16Na_2O$-8MgO/CaO series.

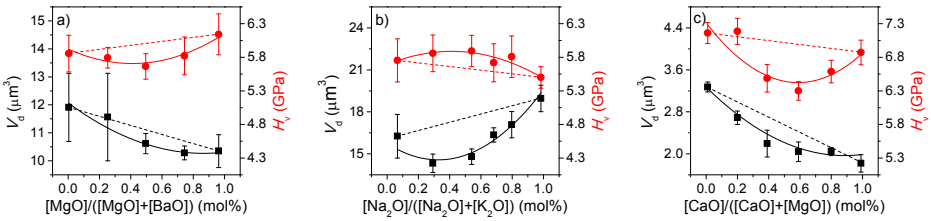

Figure 4.3: Volume of densification under indentation (V_d) and Vickers hardness (H_v) as a function of composition in mixed modifier silicate glasses. Solid lines represent the apparent relation, whereas dashed lines are linear extrapolations between end-member compositions, both intended as guides for the eyes. Data for the figure is reproduced from Papers II, III, and V.

Figure 4.3 shows that both H_v and V_d experiences a mixed network modifier effect, as deviations from linearity are observed in both properties for all three glass series. V_d exhibits negative deviations from linearity in all three series, while H_v experiences negative deviations from linearity in the mixed Mg/Ba and in the mixed Mg/Ca series and a positive deviation from linearity in the mixed Na/K series. From these trends we observe that a direct relation between H_v and V_d in mixed network modifier glasses does not exist. If we assume a linear relation between measured deformation volumes and the resistances to the specific deformation processes, a higher V_d corresponds to a lower resistance to densification. With a lower resistance to densification we expect lower hardness and thus a negative relation between H_v and V_d. This negative relation is only observed for the mixed Na/K series, whereas the mixed Mg/Ca and the mixed Mg/Ba series exhibit positive correlations. The positive deviation from linearity observed in H_v for the mixed Na/K series is probably related to the same trend observed in ρ (Figure 2.4a)), and the compositional scaling of V_d explains the trend of H_v. For both the mixed Mg/Ba and the mixed Mg/Ca series we observe an

increase in the resistance to densification, but a decrease in hardness, and the compositional scaling of V_d is thus universally not able to explain the compositional trend of H_v.

As the three glass series have a variation of hardness values, consequently, they experiences a variation in the size of the indents and thus also the in V_d values. As hardness, via Eq. (5), is negatively related to the size of the indent a smaller hardness value is equivalent to a larger indent size and a larger V_d. The negative correlation between V_d and H_v is also seen in Figure 4.3, where the mixed Na/K series show lowest H_v and highest V_d. In order to eliminate the effect of indent size, we look at V_R, as V_R is the ratio of densification and thus comparable for the three series. In Figure 4.4, V_R is plotted as a function of composition for the same glass series as in Figure 4.3.

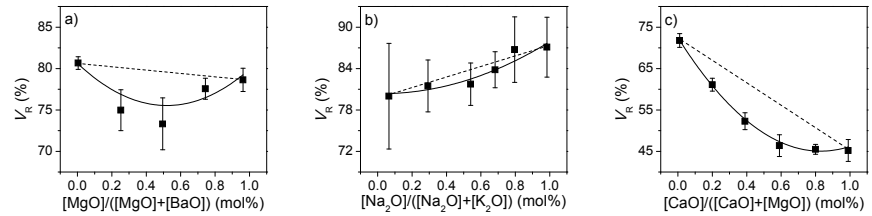

Figure 4.4: Volume of recovery (V_R) as a function of composition in three mixed modifier silicate glass series. V_R is calculated via Eq. (9). Solid lines represent the apparent relation, whereas dashed lines are linear extrapolations between end-member compositions, both intended as guides for the eyes. Data for the figure is reproduced from Papers II, III, and V.

Figure 4.4 shows a negative deviation from linearity in V_R in all three series. The negative deviations from linearity exhibited by V_R implies that the positive deviation from linearity observed in H_v for the mixed Na/K series is overcompensated by the negative deviation from linearity in V_d, resulting in a negative deviation from linearity in V_R. We see that for all glasses in both the mixed Mg/Ba and the mixed Na/K series, $V_R > 70\%$ which is expected as these glasses contain relatively high amount of silica. The same is the case for the magnesium end-member composition of the mixed Mg/Ca series, but not for the mixed compositions, and not for the calcium end-member composition. The compositional scaling observed in Figure 4.4c) indicates that Mg^{2+} is acting more like a network former than Ca^{2+}, as molar substitution of the two results in a V_R change of nearly 30%. In the mixed Mg/Ba series the decrease in V_R is not as drastic and we infer that Ba^{2+} is acting more like Mg^{2+} than Ca^{2+}, i.e., as a network former. V_R is actually increasing as magnesium is substituted for barium. The $\Delta V_R = 30\%$ between the end-member compositions of the mixed Mg/Ba series only result in $\Delta H_v = 0.3$ GPa or a change of ~4%. The small change in hardness is in good agreement with the findings presented in Ref. [116], as they found a $\Delta H_v = 16\%$ and a $\Delta V_R = 38\%$. Based on these findings they conclude that the densification ratio is much more affected by compositional changes than H_v. For the mixed Na/K series we find that $\Delta V_R = 7\%$, while $\Delta H_v = -4\%$, inferring that V_R and H_v supposable are negatively correlated, i.e., opposite trend of the mixed Mg/Ba series. The non-direct relation is also visualised by the end-member compositions, as V_d is decreasing while H_v is increasing with increasing [MgO] (Figure 4.4a)).

It is worth mentioning that the mixed Mg/Ba series, compared to the aluminosilicates, might undergo a larger degree of densification because boron during indentation converts from trigonal to tetrahedral configuration [138,139]. This conversion results in an increased density of the network, enhancing the effect of densification on hardness. However, the larger degree of densification in the boron-containing glasses compared to that of boron-free glasses is not observed, since V_R of the mixed Mg/Ba glasses (Figure 4.3a)) is generally lower than that of a mixed Na/K aluminosilicate series without boron (Figure 4.3b)).

V_d is found to be approximately four times larger than V_p (Figure 4.3), i.e., the resistance to densification is five times lower than that to plastic flow, assuming proportionality between the densification and plastic flow volumes and their specific resistances. If the resistances to the three deformation modes (elastic, plastic deformation, and densification) are perceived as parallel resistances, the largest resistance arise from the dominant deformation mode. As all three deformation processes are activated during indentation, their effects are correlated, i.e., not completely decoupled from each other, and hence the deformation mode with largest resistance (plastic flow in our case) is dominant in determining hardness. This description is in good agreement with Ref. [105], as they propose the total resistance to indentation deformation is equal to the geometrical average of the three deformation resistances, i.e., the deformation process dictating glass hardness is the one with the largest resistance.

In the three mixed modifier silicate glass series we find no correlation between either V_d or V_R and H_v. As the resistance to densification under indentation is closely related to measured volumes of densification, we propose that densification is not the determining deformation mechanism when predicting hardness in mixed modifier glass.

4.4. Plastic Flow

Deformation under indentation was initially proposed to obey the law of classical plasticity, i.e., indentation was perceived as a purely plastic process [121]. It has later been established that stress relaxation under indentation in general occurs both via densification and plastic flow. In the secondary indentation phase, an irreversible microscopic deformation occurs, and the stress relaxes either via densification as described in section 4.3 or via a volume conservative shear flow where material is forced to the surface.

Via Eqs. (6) and (7) measurements of deformation volumes were conducted on three aluminosilicate glass series. AFM images of chosen indents are shown in Figure 4.1. The resulting volumes of plastic flow are plotted in Figure 4.5 together with the respective hardness value. Figure 4.5a) shows V_P and H_v for a $64SiO_2$-$12Al_2O_3$-$6B_2O_3$-$12Na_2O$-6MgO/BaO series, b) for a SiO_2-Al_2O_3-MgO-Na_2O/K_2O series, and c) for a $60SiO_2$-$16Al_2O_3$-$16Na_2O$-8MgO/CaO series.

Figure 4.5 shows that V_P increases when calcium is substituted for magnesium and when potassium is substituted for sodium. A possible explanation is that the stronger oxygen bonding to magnesium compared to calcium and to sodium compared to potassium retards the flow of structural units, i.e., the plastic flow. In other words, the substitution of calcium for magnesium and the substitution of potassium for sodium increase the possibility for slip motion of planar structures or redistribution of non-bridging oxygen ions, resulting in an overall increase of the irreversible shear flow. As V_p of

the magnesium-containing and the barium-containing end-member compositions are similar (Figure 4.5a)), we propose that Mg^{2+} and Ba^{2+} exhibit equal combined bond strength to their surroundings. As Mg^{2+} has higher field strength than Ba^{2+}, Mg^{2+} probably experiences fewer, but stronger bonds, compared to Ba^{2+}. The combined bond strength is however the same.

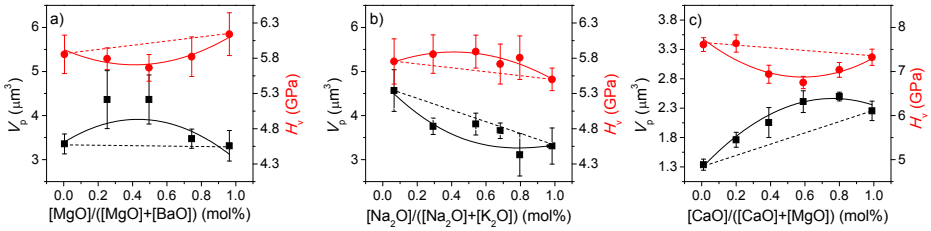

Figure 4.5: Volume of plastic flow under indentation (V_P) and Vickers hardness (H_v) as a function of composition in three mixed modifier silicate glass series. Solid lines represent the apparent relation, whereas dashed lines are linear extrapolations between end-member compositions, both intended as guides for the eyes. Data for the figure is reproduced from Papers II, III, and V.

If the plastic flow volume is assumed to be directly related to the corresponding resistance, an increase in V_P will invoke a decrease in H_v. In other words, a lower resistance to plastic flow results in lower glass hardness. Since the compositional scaling of V_p exhibits a negative deviation from linearity for the mixed Na/K series, the resistance to plastic flow exhibits a positive deviation from linearity. This positive deviation is in good agreement with the positive deviation from linearity observed in H_v (Figure 4.5b)). The compositional scaling of V_p for the mixed Mg/Ba and the mixed Mg/Ca series exhibit positive deviations from linearity and the resistance to plastic flow thus exhibits negative deviations from linearity. The negative deviations are in good agreement with the negative deviations from linearity observed in H_v (Figure 4.5a) and c)).

Above we argued that hardness was compositionally independent of both densification and elastic deformation, and we thus suggest that plastic flow accounts for the nonlinear composition dependence of Vickers hardness. Faivre *et al.* [36] reported that the plastic flow of glass is caused by the hopping of network modifiers, promoting slippage of the rigid parts of the network. This explanation is however not the entire explanation, as we may assume that the plastic low is generated by a more cooperative rearrangement of atoms. Ionic conductivity measurements reveal a minimum in conductivity as one network modifying ion is substituted for another one [31]. Hence, the lowest concentration of mobile ions is at a substitution degree of 0.50 and the plastic flow, according to Faivre *et al.* [36], experiences a minimum at this substitution degree. The minimum in ionic conductivity at equal concentrations of network modifier is also predicted by the dynamic structure model [15,62]. A minimum in ionic conductivity is, however, not consistent with observations of Figure 4.5a) and c), since a minimum in ionic conductivity corresponds to a maximum in hardness.

As mentioned in section 3.3, if we consider viscosity to be linked to the resistance to plastic flow during indentation, the occurrence of deviations from linearity in hardness might be associated with the corresponding deviations in T_g (Figure 2.6). As T_g exhibits negative deviations from linearity in

both the mixed alkali, mixed alkali-alkaline earth, and the mixed alkaline earth series, we expect V_P to exhibit positive deviations from linearity in all three series. This is not the case, as the mixed alkali series (Na/K) exhibits a negative deviation from linearity (Figure 4.5b)). The reasoning for the deviation between T_g and V_p is probably connected to the observed positive deviation from linearity observed in ρ in Figure 2.4a). If a tight-knit structure, caused by pairs of dissimilar alkali ions, creates a tighter and stronger bonding scheme around the network modifiers, it explains both the deviation in ρ and V_p. Nevertheless, one question remains; why does the tight-knit structure only occur for the mixed alkali effect, and not for the mixed alkali-alkaline earth effect?

Based on the Raman spectroscopic data, we find a relatively high concentration of T-O-T bonds in the mixed alkaline earth region (Figure 2.7). The high concentration of T-O-T bonds might be associated with the observed negative deviation from linearity in m, since higher network connectivity generally corresponds to a stronger liquid. However, the low-temperature viscosity of the mixed cation compositions is lower than that of the end-member compositions (Figure 2.6), indicating lower viscosity and less connectivity in the mixed compositions. The Raman spectroscopic data suggest that the network connectivity of the mixed Mg/Ca compositions is higher than that of the two end-members, which normally increases viscosity. Therefore we can infer that the decrease of viscosity is not related to the network connectivity, but instead is mainly related to the local structural environment around the network modifiers causing overall bond weakening.

4.4.1. Poisson's ratio

Considering the measured values of V_R and the previously reported relationship between V_R and ν [116,140], values of V_R are plotted as a function of ν in Figure 4.6. Poisson's ratio (ν) is sensitive to the excess volume in the glass network, and to the behaviour under mechanical loading, i,e., indentation. We expect materials, exhibiting reversible volume changes upon uniaxial testing, also to undergo a volume contraction under point loading. Hence, as ν relates to the ability of a glass to exhibit volume change in the elastic regime it allows for a description of the sensitivity to irreversible volume changes. In other words, ν is a measure of the materials ability to expand in the transverse axes of applied compression, and is consequently close related to V_d and V_p.

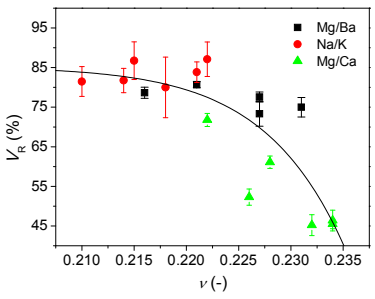

Figure 4.6: Volume recovery of indents (V_R) as a function of Poisson's ratio (ν) for three mixed modifier aluminosilicate glass series. The specific network modifier pairs are indicated in the top right corner with

individual markers. A sigmoid curve is fitted to data. Data for the figure is reproduced from Papers II, III, and V.

A sigmoidal correlation has previously been proposed between v and V_R, and is therefore fitted to data in Figure 4.6. Figure 4.6 shows that the sigmoidal trend is in good agreement with our measurements. As mentioned in chapter 3, the ratio between the deformation processes during indentation differs between different families of glasses, and any correlation between v and H_v is thus not universal, as H_v does not correlate with the elastic part of indentation. Since v relates to the ratio between transverse and axial strain, v is a viable index to discriminate between densification and plastic flow [122]. Higher values of v correspond to a larger ratio of transverse to axial strain, and therefore plastic flow is favored. Within the same glass series, e.g., mixed modifier silicate glasses, we find a good correlation between the dominant deformation mechanism and H_v. Therefore, within mixed modifier silicate glasses, a good correlation exists between v and H_v.

In the three mixed modifier silicate glass series we find a good correlation between V_p, v and H_v. As the resistance to plastic flow under indentation is closely related to measured volumes of plastic flow, we propose that plastic flow is the determining deformation mechanism when predicting hardness in mixed modifier glass. We find that v shows up as a good index to discriminate between densification and plastic flow, and we observe a good correlation between the V_R and v. We propose that in certain glass families, e.g., mixed modifier silicate glass, where either densification of plastic flow is the dominant deformation process under indentation, a good correlation exists between v and H_v.

4.5. Summary

The mixed modifier effect manifest itself in the quantities of all three deformation processes under indentation; densification, plastic flow, and elastic deformation. The elastic part of indentation is closely related to elastic moduli, which scales linearly with composition for both the mixed alkali-alkaline earth effect and the mixed alkaline earth effect. Elastic moduli of the mixed alkali glasses exhibit a positive deviation from linearity. For the entire mixed modifier effect we find negative deviations from linearity in both the densification part of indentation and volume recovery. The plastic part of indentation exhibits a positive deviation from linearity for the mixed alkali-alkaline earth effect and the mixed alkaline earth effect, but a negative deviation from linearity for the mixed alkali effect. We find no correlation between either elastic deformation or densification and hardness. Hardness experiences similar compositional trends as the resistance to plastic flow, and we propose that the hardness of mixed modifier glasses is dominated by the resistance to plastic flow. We also find that v is a viable index to discriminate between densification and plastic flow, and thus in mixed modifier glasses v exhibits a good correlation to hardness.

For the mixed alkali-alkaline earth effect and the mixed alkaline earth effect we find an increase in the connectivity of the network, but a decrease in the viscosity. These results are evident from negative deviations from linearity in viscosity, glass transition temperatures, and liquid fragility indices, but a positive deviation in the amount of tetrahedrally bonded silica units. We infer that the decrease in viscosity is not related to the network connectivity, but instead is mainly related to the local structural environment around the network modifiers causing overall bond weakening. We propose that the overall bond weakening around the network modifiers is responsible for the

negative deviations from linearity in the resistance to plastic flow and thus also the compositional trends of hardness.

The mixed alkali effect is a special case, as it experiences a positive deviation from linearity in H_v, ρ, and E, i.e., dissimilar trends to the mixed alkali-alkaline earth effect and the mixed alkaline earth effect. The compositional trends of H_v, ρ, and E have been explained by a tight-knit structure, caused by pairs of dissimilar alkali ions, creating a tight and strong bonding of the network modifiers. Why the tight-knit structure only occurs for the mixed alkali effect is however not explained, and it does not agree with the negative deviations from linearity in viscosity and glass transition temperatures. We propose that the compositional trends of the mixed alkali effects can be explained by two opposite scenarios; (i) general bond weakening around the network modifiers also occurs for the mixed alkali effect and accounts the negative deviations in viscosity and glass transition temperatures. (ii) The low charge and low ionic radii of the alkali ions enable them to exist in close proximity to each other in the glassy network, creating a dense structure which accounts for the positive deviations in ρ and E. These two effects counterbalance each other and the positive deviation from linearity in the volume of plastic flow, and thus H_v, may be explained by the strong and dense structure formation involving the alkali ions only exists at room-temperature. At elevated temperatures the thermal energy exceeds the bonding energy of the cluster structure and it becomes unfavourable for the alkali ions to participate in the tight-knit structure. The strong and dense tight-knit structure collapses and the glass returns to a structure which resembles that of the mixed alkali-alkaline earth effect and the mixed alkaline earth effect. The temperature dependence of the tight-knit structure explains why the mixed alkali glasses experiences a higher hardness and less plastic flow at room-temperature, but similar compositional scaling of T_g and m as the mixed alkali-alkaline earth and the mixed alkaline earth effects.

5. Impact of Chemical Composition on Electronic Conductivity

In order to get a better understanding of transport processes in inorganic glass and the influence of electron motion in regard to bulk properties and structure of glass we investigate the electronic conduction and its compositional and structural dependences. We chose a vanadium tellurite system as it experiences higher electronic conductivity than other transition metal containing glasses, and thus have high potential for application in electrical devices, memory switching, and gas sensors [141]. We clarify the influence of structural characteristics such as the redox state of the carrier, distance between the carriers, and crystallinity of the network, on electronic conductivity. Therefore, we start with establishing a fundamental understanding of how electrons move in glassy materials. The structural and compositional influences on electronic conductivity were one of the main focuses of Papers I and VI.

5.1. Electronic Conductivity in Glass

If a glass contains transition metal ions of two valences, e.g., V^{4+} and V^{5+}, it can carry a current due to the motion of electrons. An electron can move from the low valence state (V^{4+}) to the high valence state (V^{5+}), just as it can between ions dissolved in water [142]. When an electron occupy a site in its motion through the glass for a time longer than the typical period of vibration, the ions of which the glass is composed of have time to relax into a configuration appropriate to the altered charge [143]. The local structure alteration is largest in the neighbourhood of the host ion and the electron and its accompanying distortion may be treated as a single particle - a polaron [144,145]. The distortion that the electron induces around the host carry a change in the electrons potential energy which traps the electron on the host cation, and the electron is effectively self-trapped. [145]. The change in potential energy caused by the polaron is called the polaron binding energy, W_p. The size of the polaron depends upon the overlap of the electron wave function and on W_p. If the overlap between wave functions is large compared to the polaron binding energy ($W_p < 2J_p$), the distortion expands further than the first sphere of atoms around the host and the polaron is adiabatic and nominated "large". $2J_P$ is the polaron band width. If the overlap between wave functions is small compared to the polaron binding energy ($W_p > 2J_p$), the distortion is restricted to the first sphere of atoms around the host and the polaron is non-adiabatic and nominated "small" [146-148]. A small polaron can occur under two conditions; (i) W_P is particularly large or (ii) the distance between sites is large resulting in a very small overlap of wave functions, i.e., J_P is small. In other words, the small polaron describes both the case of strong electron-lattice interactions and that of strongly localized electrons. The conduction of small polarons features a unique transition between conduction in a polaron band and conduction by thermally activated hopping. The combined electronic conductivity is illustrated for a crystalline material in Figure 5.1.

The transition from conduction in a polaron band to conduction by thermally activated hopping occurs at a critical temperature (T_t) when $h\tau^{-1} \approx J_P$, where τ is the hopping time. At this temperature, in the order of half the Debye temperature ($\frac{1}{2}\Theta_D$), the mean free path (average distance between conductive sites) of the electrons becomes of the order of the interatomic distance and the conduction is properly described as thermally activated hopping [30,142]. Below T_t the conduction take place in a polaron band where the electron tunnels between randomly distributed sites with equivalent energy levels moving with an effective mass considerable larger than that of the electron.

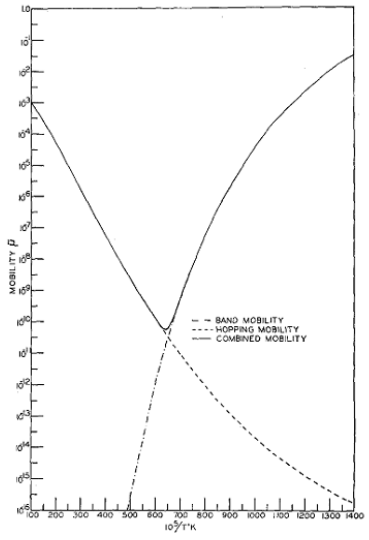

Figure 5.1: Electron mobility as a function of inverse temperature predicted from the Holstein model for a small polaron travelling in a crystalline material [30].

Conduction in a polaron band (also known as variable range hopping) does not involve energy exchange between the electron and the lattice, while conduction by hopping is governed by the energy from normal modes of the lattice. Figure 5.1 shows that in a crystalline material the mobility of the polaron band decreases with decreasing temperature. The decreasing mobility is realized on the basis of a probability picture: the polaron band region describes the transfer of electrons between sites with coincident energy levels and at absolute zero temperature the energy of all sites will coincide, and the probability of the electron transfer will be a maximum. With elevating temperatures the thermal oscillation of the lattice will continuously alter the energy of each site, making the timescale of coincident energy between two sites smaller.

Above $\frac{1}{2}\Theta_D$ the main conductivity process is thermally activated hopping, where the conductivity increases with increasing temperature, as individual jumps are thermally activated processes. Combining the two transport mechanisms yields a local minimum of electron mobility at T_t. Holsteins model of electron mobility was proposed to account for electronic conductivity in crystalline materials, but the theory of small polarons as the conducting mechanism is transferable to glasses.

As mentioned in section 2.1, a glass has a random network structure with a larger distribution of bond angles and bond lengths compared to the corresponding crystal. This difference gives an inherent difference in the potential energy of sites between glass and the corresponding crystal. The average difference in potential energy between sites in glass and those in crystals is nominated as W_D. Below T_t Holstein [30] predicted the conduction in a crystal to happen by variable range hopping with a maximum of conductivity at absolute zero due to all sites having equal potential

energy. The largest electronic conductivity of a glass is not obtained at zero Kelvin as the potential energy of sites is dispersed due to W_D. These energy levels will be randomly distributed around the glass resulting in a very low density of sites with equal potential energy and an even lower density of channels with coincident potential energy that can carry a current, resulting in almost zero conductivity at zero Kelvin. Meaning that, any thermally induced motion of the lattice will carry a percentage of the sites into configurations of equal potential energy, despite the two sites at zero Kelvin had different energy levels. The density of conductive sites in the lattice thereby increases as a function of temperature. How strongly the density of conductive sites increases depends upon W_D, which becomes the activation energy for the electron transfer. As the density of conductive sites increases an exponential increase in the electron conductivity arise due to the exponential increase in overlap of the electrons wave functions thus decreasing the mean free path and ultimately resulting in a higher conductivity.

At T_t the mean free path becomes of the same order as the interatomic distance and at temperatures above thermally activated hopping is the dominating mechanism for electron transfer [142]. The major change from variable range hopping to thermal activated hopping is the concentration of conductive site. The energy from the normal modes increase the energy differential over which a transfer can be made, effectively increasing the density of conductive sites. Below T_t the energy of the electron is insufficient to surpass W_p. Above T_t the thermal energy of the normal modes are high enough to overcome the binding energy and the activation energy changes from W_D to $W_H \pm \frac{1}{2}W_D$ [148,149]. W_H is the polaron hopping energy. One of the most striking differences between conduction in a crystal and conduction in a glass is the glass absence of a local minimum of mobility. The conductivity of the glass has its minimum at zero Kelvin and only increase with temperature. Mott [142] proposed a model for the combined conductivity in glassy materials, and the equation is shown in Eq. (9):

$$\sigma = \left(\frac{v_0 e^2}{R k_b T} \right) c(1-c) e^{-2\alpha R} e^{-\frac{W}{k_b T}} \tag{9}$$

where v_0 is the optical phonon frequency, R is the mean distance between the ions, k_b the Boltzmann constant, c the concentration of one of the two valencies and α the tunnelling factor [141]. The activation energy (W) from Eq. (9) is given in Eq. (10) and split into two terms because of its temperature dependence.

$$W = \begin{cases} W = W_H + \frac{1}{2}W_D & - \quad T < \Theta_D/2 \\ W = W_D & - \quad T < \Theta_D/4 \end{cases} \tag{10}$$

In a glass W_p, W_H and W_D all changes from site to site, which is due to the difference in configurations around the hosts and Eqs. (9) and (10) thus averages over the entire glass. Eq. (9) can be divided into 4 fractions making the understanding of the equation easier. $v_0 e^2 / R k_b T$ is a pre-exponential gathering of constants, $c(1-c)$ the redox state of sites, $e^{-2\alpha R}$ the distance between sites (which for a large polaron equals 1), and $\exp(-W/k_b T)$ the energy barrier and the probability for hopping [142,148]. Viz., Eq. (9) contains three critical parameters; (i) redox state, (ii) distance, and (iii) activation energy. Eq. (9) depicts the conductivity for both large and small polarons and

accounts for the change in dominating mechanism of electron transfer, going from variable range hopping in the low temperature range to thermally activated hopping in the high temperature range.

The electronic conduction of glass is typically evaluated via Eq. (9) and in order to establish a good correlation between structure and property it is important to investigate the influence of critical parameters of electronic conduction.

5.2. Valence State of Transition Metal Ions

In a typical oxide glass containing transition metal, only a fraction of the cation sites are occupied by an ion which can contribute an electron to the electronic conduction process, (i.e., V^{4+}) and in most of these situations the next nearest neighbour ions are oxygen anions [150]. Meaning that, the spacing between conductive cations is large and consequently the overlap between electron wave functions is small, explaining why the small polaron is the normal transport mechanism in glasses containing transition metals. As the redox state of the transition metal approaches 0.5, the probability of finding electron donating and electron accepting sites close enough for charge transfer to occur increases, and theoretically reaches a maximum at 0.5. As the electron relies on this transfer process to propagate, the electronic conduction is largely dependent on the redox state of the charge carrier (c).

Six binary vanadium tellurite glasses were prepared via the normal melt quenching technique and melted for 0.5 h at 700 °C. The glassy state was confirmed by X-ray diffraction and coplanar samples of each composition were polished and sputtered with gold before electronic conductivity was measured by impedance spectroscopy (IS). The electrical measurements were performed in air with a two-point sample holder from 303 to 523 K and with an applied voltage of 100 mV in the frequency range from 10^6 to 1 Hz. By fitting Eq. (9) to each set of conductivity data the parameters of the Mott-Austin equation can be determined. In Figure 5.2a) Eq. (9) is fitted to each set of conductivity data and the derived parameters are shown in Table 1. In order only to have two fitting parameters (i.e. α and ν_0), c and R are determined by electron spin resonance spectroscopy and pycnometry, respectively.

Table 1: Electronic conductivity at 298 K (σ_{298K}), pre-exponential term (σ_0), and activation energy (W) of the Mott equation, tunnelling factor (α), phonon frequency (ν_0) and adjusted sum of squared errors (SSQE) determined via fitting of Eq. (3) to electronic conductivity data. R is the mean distance between vanadium ions (from density data and Eq. (4)) and c is the ratio of V^{4+} to total vanadium (from ESR).

Sample ID	Log(σ_0) [-]	W [eV]	Log(σ_{298K}) [-]	c [%]	R [nm]	α [cm^{-1}]	ν_0 [s^{-1}]	SSQE [-]
VT_10	1.29	0.50	-7.12	4.40	0.64	$1.7 \cdot 10^{-9}$	$1.6 \cdot 10^{10}$	0.9980
VT_20	2.37	0.43	-4.97	5.07	0.52	$1.0 \cdot 10^{-8}$	$1.4 \cdot 10^{11}$	0.9987
VT_30	2.78	0.39	-3.86	5.16	0.47	$7.4 \cdot 10^{-9}$	$3.2 \cdot 10^{11}$	0.9992
VT_40	3.04	0.37	-3.29	5.13	0.45	$2.7 \cdot 10^{-8}$	$5.5 \cdot 10^{11}$	0.9996
VT_50	3.36	0.37	-2.88	4.15	0.43	$1.0 \cdot 10^{-8}$	$1.3 \cdot 10^{12}$	0.9995
VT_65	3.39	0.38	-3.00	1.53	0.42	$1.7 \cdot 10^{-7}$	$3.7 \cdot 10^{12}$	0.9997

Figure 5.2a) shows the electronic conductivity of the vanadium tellurite glasses increases with increasing vanadia concentration. The observed tendency of an increase in electronic conductivity with increasing V_2O_5 is in good agreement with literature [151-153].

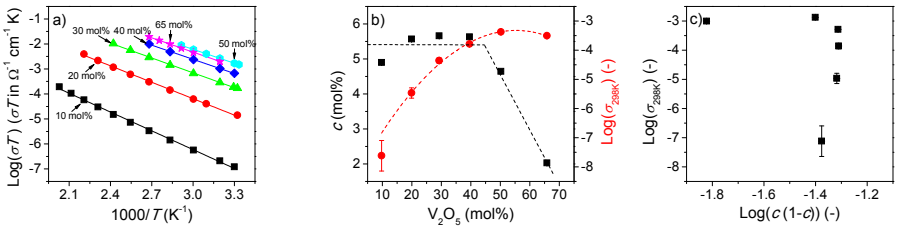

Figure 5.2: a) Logarithm of electronic conductivity times temperature (Log(σT)) as a function of inverse temperature (1000/T) for the vanadium tellurite glasses. The concentration of vanadium is indicated next to each data set and the chemical compositions are tabulated in Table 1. The Mott-Austin equation (Eq. (9)) is fitted to each composition and plotted as solid lines. Regression data is shown in Table 1. b) The valence ratio of c = $[V^{4+}]/[V_{total}]$, where $[V_{total}]$ is the total amount of vanadium ions, and logarithm of electronic conductivity at 298K (Log(σ_{298K})) as a function of vanadia concentration. Dashed lines are guides for the eye. c) Logarithm of electronic conductivity times temperature (Log(σT)) as a function of Log(c(1-c)). Eq. (9) predicts a linear relation between (Log(σT)) and Log(c(1-c)). Data for the figure is reproduced from Paper I.

In order to highlight this correlation the electronic conductivity at 298 K (σ_{298K}), along with c, are in Figure 5.2b) plotted as a function of composition. Log(σ_{298K}) initially increase with V_2O_5, whereas c initially is constant. At high V_2O_5 concentrations Log(σ_{298K}) levels of, whereas c drastically decreases. Eq. (9) predicts a direct proportionality between Log(σT) and Log(c(1-c)), which is why Log(σT) vs. Log(c(1-c)) is plotted in Figure 5.2c). Figure 5.2c) shows that the electronic conductivity of the vanadium tellurite glasses is not as dependent on c as proposed in Ref. [142], as no linear relation is apparent. Theoretically, as c is below 50 mol%, we expect an increase in Log(σ_{298K}) with increase in c. A positive relation between Log(σ_{298K}) and c is, however, not what we observe in Figure 5.2b), as Log(σ_{298K}) increases when c decreases.

An interesting observation is that before V_2O_5 = 45 mol%, properties such as hardness and liquid fragility (both dynamic and thermodynamic) remains constant through compositional change (Figure 2.5 and Figure 3.4), whereas above V_2O_5 = 45 mol%, the compositional scaling is sharp linear deviations from the initial plateau. We thus propose the existence of a critical vanadia concentration equal to 45 mol%. We believe the observed trends in hardness and liquid fragility are closely related to the valence state of the vanadium ions (c). A possible explanation is that the presence of V^{4+} results in a more constraint structure than V^{5+}, thus resulting in fewer constraints per unit volume and therefore lower hardness and higher liquid fragility.

It is noted that the change in c is relatively small, and that a more pronounced tendency might occur if a larger dispersion of c values were accessible. The redox state is normally controlled in the glass-forming melt during the preparation of the glass, where the redox state typically depends on three factors; (i) melting temperature, (ii) furnace atmosphere, and (iii) composition [154]. Decreasing the partial oxygen pressure in the furnace atmosphere or increasing the melting temperature shifts the redox equilibrium toward the reduced state [2]. We tried to regulate c by post heat-treatment of the

as-made glasses in controlled atmospheres, as heat-treatment has proven a valid method to control the redox state of ion [155,156]. However, heat-treatments were unsuccessful for vanadium, probably due to its larger reduction potential (-1.3V for $V^{5+} \rightarrow V^{4+}$ compared to -1.0V for $Fe^{3+} \rightarrow Fe^{2+}$) [157].

We also tried to regulate *c* via the melting temperature of the glass-forming melt, and results for a $2TeO_2$-V_2O_5 glass are shown in Figure 5.3.

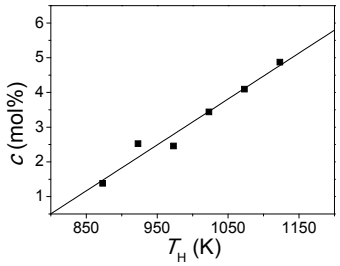

Figure 5.3: Molar ratio of V^{4+} to total vanadium (*c*) as a function of the temperature of the glass-forming melt during preparation of the glass (T_H). The vanadium tellurite compositions used are congruent $2TeO_2$-V_2O_5 compositions.

Figure 5.3 shows that the investigated vanadium tellurite system experiences a good correlation between T_H and *c*, where T_H was melting temperature of the glass-forming melt. Following the linear relation, the optimal redox state of c = 50 mol% is achieved at $T_H \approx 4600$ K, which is far beyond the melting temperature of the gold crucible. Figure 5.3 shows the feasibility of controlling the redox state of vanadium in the glass by variations in the melting temperature of formation. However, the achieved dispersion of *c* values is small and in order to get a high concentration of V^{5+} a different method have to be considered.

In a series of binary vanadium tellurite we find that the valence state of vanadium in the glass is directly proportional to the melting temperature of glass formation. We also find that the electronic conductivity is almost independent on valence state of vanadium, opposing the proposed relation in the Mott-Austin equation (Eq. (9)).

5.3. Distance between Carriers

As the jump frequency for electron hopping is largely dependent on the overlap between the electron wave functions of participating sites, the mean distance between these sites determines the average jump frequency, and thus also the conductivity. The mean spacing between sites (R) can be calculated as per Eq. (11) [141,158]:

$$R = \left(\frac{M_W}{2M_e \rho N_v} \right)^{1/3} \tag{11}$$

where M_W is the molar mass, M_e the molar concentration of conductive sites (i.e. vanadium), ρ the density, and N_v Avogadro's constant. For six binary vanadium tellurite glasses R was calculated via density measurements and Eq. (11), and plotted together with impedance spectroscopy data in Figure 5.4.

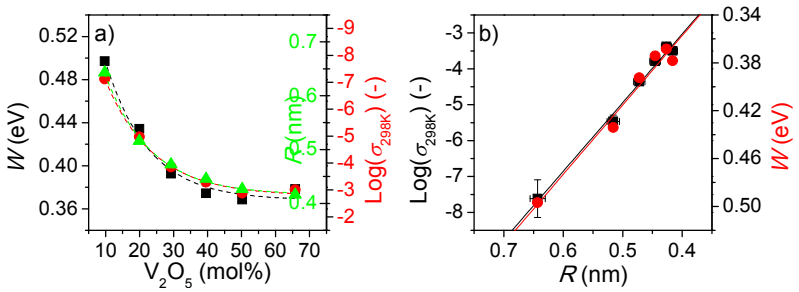

Figure 5.4: a) Logarithm of electronic conductivity at 298K (Log(σ_{298K})), activation energy (W), and mean distance between carriers (R) as a function of composition for the vanadium tellurite glasses. W is determined via data from Figure 5.2a) and Eq. (9), and R is determined via Eq. (11). Dashed lines are guides for the eyes. b) Logarithm of electronic conductivity times temperature (Log(σT)) and W as a function of R. The solid lines are linear fits to data. Data for the figure is reproduced from Paper I.

As shown in Figure 5.4a), the electronic conductivity measured at 298 K (Log(σ_{298K})), initially increases with increase in vanadia, and then levels off above a vanadia concentration of 45 mol%. The compositional scaling of Log(σ_{298K}) matches that of both R and W (Figure 5.4a)), since Eq. (9) predicts R and Log(σ_{298K}) to be inversely proportional and W and Log(σ_{298K}) to be directly proportional. We find a linear relation between W and R and show that the activation energy for hopping is linearly dependent on the jump distance. We see that the electronic conductivity of the vanadium tellurite glasses linearly depends on R, which is in good agreement with the results presented in Table 1 since we find that the electron hopping occurs strictly adiabatic, as $\exp(-2\alpha R) = 1$. In the adiabatic case you expect a direct proportionality between R and Log(σT), supporting Eq. (9).

Figure 5.4b) shows that both Log(σ_{298K}) and W are directly proportional to R, and we thus propose a linear relation between the overlap of the wave functions and the jump frequency. That is, the hopping distance is directly proportional to the activation energy for hopping, and thus to electronic conductivity at a given temperature. An interesting observation is that the electronic conductivity occurs strictly adiabatic and that σ does not follow the expected correlation to c as predicted by the Mott-Austin equation, but instead is showing a good correlation with R. If the decoupling of σ from c also occurs at higher c values, it enables optimization of hardness and liquid fragility independent from σ.

5.4. Crystallinity

As electronic conduction occurs by electron hopping from one site to another with activation energy directly proportional to the jump distance, the highest electronic conductivity is achieved in pure vanadium oxide, simply because R is minimized. The electronic conductivity of a glass is controlled

by temperature, as the available thermal energy determines the possible jump distance. In section 5.3 we show that the activation energy of electron hopping is linearly dependent on the jump distance, and temperature thus determines the largest feasible jump distance. As the temperature increases so does the feasible jump distance and new electron pathways emerge, meaning that the longest jumps are the limiting factor. Crystallisation averages jump distances, and remove any high energy jumps (electron jump between sites relatively far away from each other), and crystallisation thus normally leads to an increase in the electronic conductivity. Hirashima *et al.* [159] proposed that the conductivity of a vanadium tellurite crystal might be as high as that of a vanadium crystal and that both are 2 orders of magnitude larger than that of the corresponding glass. From a technical point of view it is important to achieve the highest possible electronic conductivity, keeping the mechanical strength inherent in the glass [160].

We investigate the dependence of the electronic conductivity on the weight fraction (wt%) of glass in different mixtures of congruent $2TeO_2$-V_2O_5 crystal and glass. Glass samples were prepared via the normal melt quenching technique. Appropriate amounts for obtaining $2TeO_2$-V_2O_5 were mortared, and 12 g was melted in a gold crucible at 700 °C for 1 h. In order to crystallize the glass, heat treatment was conducted at 400 °C for 2 h, and both crystalline and glassy samples were examined with a scanning electron microscope (SEM). Images were taken on the surface of the samples and in fractures (the interior of the samples). Samples with glass fractions (X) ranging from 0 to 100 wt% were made and electrical measurements were performed in air from 303 to 523 K and with an applied voltage of 100 mV in the frequency range from 10^6 to 1 Hz.

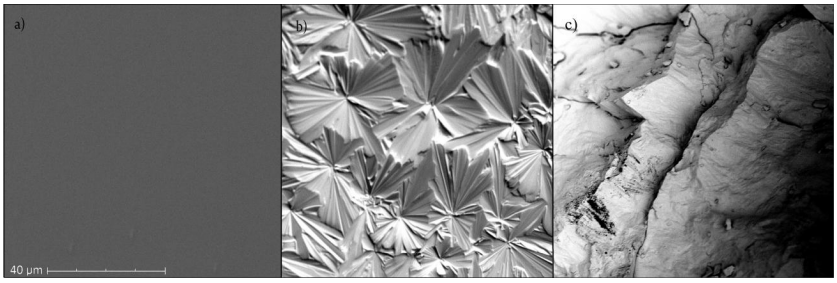

Figure 5.5: Scanning electron microscopy images of a) the surface of $2TeO_2$-V_2O_5 glass, b) the surface of $2TeO_2$-V_2O_5 crystal, and c) a fracture of a $2TeO_2$-V_2O_5 crystal. The three images are taken with similar settings but c) is taken at a lower magnitude compared to a) and b). Data for the figure is reproduced from Paper VI.

Figure 5.5 shows images of a) the surface of $2TeO_2$-V_2O_5 glass, b) the surface of $2TeO_2$-V_2O_5 crystal, and c) a fracture of a $2TeO_2$-V_2O_5 crystal. Figure 5.5a) shows that the glass is fully amorphous and Figure 5.5b) and c) shows that the crystal is fully crystalline. The SEM results are supported by XRD measurements. In Figure 5.6 the electronic conductivity of the glass, the crystal and mixes are plotted as a function of temperature.

The solid lines in Figure 5.6a) are Mott-Austin fits (Eq. (9)), from which the activation energy for electron hopping (W) can be determined. As the slopes of the two lines are similar, so are W. W are determined using electronic conductivity data in a temperature range from 303 to 523 K, which is

higher than ½Θ_D [162], meaning that the electronic conduction occurs by thermally activated hopping (Eq. (10)) [148]. Since the glass and the crystal have similar W, we propose the mechanisms of electron transfer in the two states are identical.

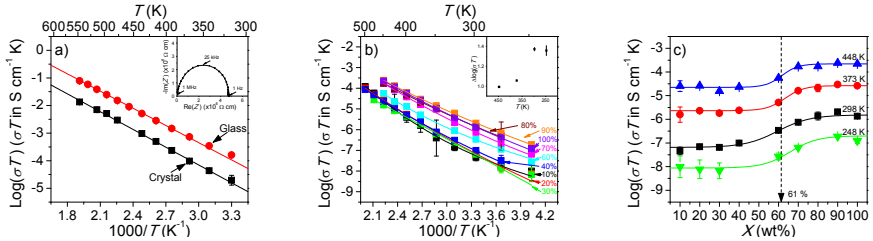

Figure 5.6: a) Log(σT) as a function of the inverse temperature for both bulk 2TeO2-V_2O_5 crystal and glass. Solid lines: Mott-Austin fits (Eq. (9)) [142,148] with a correlation factor of $r^2 = 0.998$ for both lines. Inset: Example of a semicircle obtained for glassy 2TeO_2-V_2O_5 by impedance spectroscopy at 343 K. Note the absence of any low frequency spike attributable to the polarization of the electrode-electrolyte interface. Its absence is characteristic of pure electronic conductivity (no ionic transport) [161]. b) Log(σT) as a function of the inverse temperature for different weight fractions (wt%) of glass (X) in the glass-ceramics (marked on the curves). The solid lines are guides for the eyes. Inset: Δlog(σT) as a function of temperature, where Δlog(σT) is the difference in log(σT) between $X = 90$ wt% and $X = 10$ wt%. c) Log(σT) measured at different temperatures (marked on the curves) as a function of the glass fraction in the 2TeO_2-V_2O_5 glass-ceramics. Solid lines: sigmoid fits; Vertical dashed line: crossover point of the sigmoid curves. Data for the figure is reproduced from Paper VI.

The electronic conductivity of samples with crystallinity ranging from 0 to 100 wt% is plotted against the inverse temperature in Figure 5.6b). The glass-ceramics presented in Figure 5.6 experienced different annealing conditions from those presented in Figure 5.6a), why the electronic conductivities presented in Figure 5.6a) and b) are not comparable. Figure 5.6b) shows that the electronic conductivity of the glass-ceramic samples increases with increasing temperature in a non-Arrhenian way. The Mott–Austin equation is applicable only for monophase structures and not for multi-phase systems, such as glass-ceramics [142]. This limitation is due to possible differences in the temperature dependence of activation energies for different phases. Figure 5.6b) shows that the electronic conductivity increases with an increasing X, which is shown explicitly in Figure 5.6c), where the electronic conductivity measured at given temperatures is plotted against X. All four curves show the same trend of two plateaus separated by a transition zone. The crossover from low to high conductivity occurs at $X \approx 61$ wt%. Another trend is that the enhancement of the electronic conductivity by increasing X is more pronounced at low temperatures compared to high temperatures (inset of Figure 5.6b)). As the activation energy of the glassy phase is slightly higher than that of the crystal, a larger difference in electronic conductivity is expected at low temperatures.

We propose that the crossover in electronic conductivity shown in Figure 5.6c) originate from one of three scenarios: (i) changes in the redox state of vanadium in crystallized samples (reflected by changes in c), or (ii) limitation of the electronic conduction in the grain boundaries. A reduced conduction in grain boundaries has been shown for ionic conductors [163,164] and is attributed to a

constriction effect caused by a small contact area between grains [165]. A reduced conduction in the grain boundary may also occur in the case of mixed crystalline and vitreous grains. (iii) The sigmoid shape of the curves (Figure 5.6c)) indicates a percolation threshold, which might be caused by the lower intrinsic electronic conductivity in the crystal grains compared to that in the glassy grains. Since the electronic conductivity is higher in the glassy grains than in the crystal grains, the glassy phase facilitates the electrons' preferred pathway. Figure 5.6c) suggests that an interconnected pathway of glass grains does not occur until X reaches 61 wt%.

Activation energies for electronic conduction determined in the temperature range from 303 to 523 K in both vitreous and crystallized $2TeO_2$-V_2O_5 are found to be identical within experimental error. IS measurements thus indicate that the mechanisms of electronic conduction are similar, i.e., thermally activated hopping in both the glass and the crystal. We find that the electronic conductivity of vitreous $2TeO_2$-V_2O_5 is up to 1.5 orders of magnitude higher than that of the crystal (inset of Figure 5.6b)), and we thus propose that $2TeO_2$-V_2O_5 glass is more suitable for electrochemical devices than a $2TeO_2$-V_2O_5 glass-ceramic.

5.5. Summary

The structural dependence on electronic conductivity was investigated in two vanadium tellurite series; (i) with changing vanadium-to-tellurium ratio, and (ii) with constant vanadium-to-tellurium ratio but changing crystallinity. We find that the vanadium tellurite glass does not obey the proposed linear relation between σ and c as depicted in the Mott-Austin equation. However, we find a strong correlation between c and properties related to the connectivity of the network, i.e., H_v and m. We propose the existence of a critical vanadia concentration in binary vanadium tellurite equal to 45 mol%. We believe the observed trends in H_v and m are closely related to c and explain the compositional trends by the presence of V^{4+} resulting in a more constrained structure than V^{5+}. The structural change in coordination configuration from V^{4+} to V^{5+} results in fewer constraints per unit volume and therefore lower H_v and higher m.

In order to optimize the electronic conductivity of the vanadium tellurite glasses, we tried to control c via different methods. The most successful method was controlling the melting temperature of the glass-forming melt, as this temperature controls the partial oxygen pressure and thus the redox equilibrium between melt and atmosphere. We find a direct proportionality between c and the melting temperature of glass formation (T_H). If this linear relation between c and T_H persists at higher V^{4+} concentrations, it enables for property tailoring only via the melting temperature of the glass forming melt.

We find a good correlation between the overlap of the electron wave functions between potential jump sites and the electron jump frequency. That is, the electron hopping distance is directly proportional to the activation energy for hopping, and thus to electronic conductivity at a given temperature. The electronic conductivity occurs strictly adiabatic and shows a linear correlation to the average jump distance. If the non-linear tendency between σ and c persists at higher V^{4+} concentrations, it enables optimization of H_v and m independent from σ.

Electronic conductivity of a vanadium tellurite glass system was investigated as a function of crystallinity, as the crystalline structure supposedly increases the electronic conductivity, which is

advantageous from a technical point of view. We find that the electronic conductivity of vitreous $2TeO_2$-V_2O_5 is up to 1.5 orders of magnitude higher than that of the corresponding crystal and thus propose that vanadium tellurite glass is more suitable for electrochemical devices than a glass-ceramic.

The important implication drawn is the existence of a critical vanadia concentration in the vanadium-tellurite glasses, above which the local structure will be subjected to a drastic change, leading to large changes in both physical and dynamic properties. We find that the most important structural characteristic for electronic conductivity is the electron jump distance and thus the spacing between carriers, i.e., not the redox state ratio of the electron carriers. An electrochemical application, e.g., cathode material in secondary lithium batteries, requires optimization of relevant properties such as m, H_v and σ. This work contributes to establishing such knowledge basis for designing battery materials.

6. General Discussion and Perspectives

For technical purposes scientists have spent decades attempting to link both structure and property to composition. The structure-property links are important, as they provide a predictive power, and enable compositional property design for specific applications. The composition-property relations of glass have attracted much attention, from both scientists and industry, but a complete understanding of these relations lacks. In particular, the dynamic properties and properties related to either electronic or ionic motion are challenging, due to the inherent heterogeneity and complicated character of the glass structure. In the present Ph.D. thesis, we investigated composition-property relations in mixed modifier glasses and in mixed former glasses. We applied novel approaches to investigate the composition-property relation, and focused on properties related to transport processes in inorganic glass.

The study of transport processes of glass and glass-forming melts is a crucial subject of glass science due to the importance of transport processes in applications such as electrochemical devices, gas sensors, cover glass for electronics, and architecture. The electron and ion motion in glass has been extensively studied for almost a century, and considerably progress has been made. The ionic transport processes and its influence on dynamic properties in single and mixed modifier glasses are largely explainable by a combination of the modified network theory and the dynamic structure model, whereas the electron motion is described by the Mott-Austin equation. In the present Ph.D. thesis we investigated electronic conduction and ion motion, and their influence on properties and of structure. Despite progress, particularly in the understanding of the deformation processes during indentation and its influence on glass hardness, further investigations are needed to establish a coherent picture of transport processes in inorganic glass.

In the study of the deformation processes under indentation we found that in mixed modifier glasses, the resistance to plastic flow was controlling the compositional scaling behaviour during modifier substitution. We argued that a weakening in overall bond strength around the network modifiers caused the observed deviations in hardness. For the mixed alkaline earth effect we implied that the weakest bonds in the network are those around the network modifiers, however, we found that the resistance to plastic flow was ~4-5 times larger than that to densification. In other words, despite the weak bonds around the network modifiers, the activation energy for plastic flow (which is believed to propagate via the bonds surrounding the network modifier ions) was higher than that for densification. The reasoning for this discrepancy might be twofold; (i) a more collaborative rearrangement of atoms under indentation, and thus a blunt distinction between the deformation processes. (ii) load dependence. As the deformation processes are activated via different atomic bonds, intuitively, the ratios between the deformation processes dependent on the applied pressure. It is of interest to investigate the influence of the three deformation processes on hardness at both lower and higher loads, where the resistances to elastic deformation and to densification are believed to constitute a larger participation in the total resistance to deformation.

Another perspective is to investigate the direct link between the volume of plastic flow and hardness for other glasses than mixed modifier glasses, and hereby validate the universality of the proposed positive relation. If the positive relation between plastic flow and hardness is a universal

trend, it is an important implication for technical applications where optimization of hardness is necessary.

The applied method for determining the different deformation volumes is developed for boron-containing glass, and a proper investigation of the applicability of the method has not been conducted for silica-based glass. If the annealing procedure is not adequate to fully relax the glass and expand the entire densified zone, the method results in erroneously high ratios of plastic flow-to-densification. From a scientific point of view the method is applicable to silica glass, however, its validity is not experimentally verified. Another assumption is that we assume a linear relation between the volumes of deformation and the corresponding resistances. Presumably, for small volume changes this assumption is valid, but we expect load dependence in extreme cases, simply due to the nature of the involved chemical bonds.

In the investigation of the influence of structure on the electronic conductivity of mixed network former glass, we found a strong correlation between the valence state of the vanadium and the properties related to the connectivity of the network, i.e., hardness and liquid fragility. If the decoupling of electronic conductivity from the valence state of vanadium is universal, it enables optimization of hardness and liquid fragility independent from the electronic conductivity. For an electrochemical application, e.g., cathode material in secondary lithium batteries, it is important to optimize both mechanical and dynamic properties. It is of interest to find a method capable of changing the redox state of vanadium, preferentially applicable as a post treatment of the glass. A study of electronic conductivity as a function of redox state at constant vanadium concentration has, to the best knowledge of the author, not yet been conducted. Such study would approve whether the Mott-Austin equation is generally applicable or if the found non-linear relation between valence state and electronic conductivity occurs in other transition metal containing glass systems as well.

The crystallisation experiments showed that the vanadium tellurite glass had an electronic conductivity in the order of 1.5 orders of magnitude larger than that of the corresponding crystal. The crystal structure normally exhibits higher electron conductivity compared to the vitreous one, and a glass-ceramic potentially achieves the high mechanic strength of the glass and the high electronic conductivity of the crystal. However, two problems were encountered during the crystallisation process; (i) crystallisation of the vanadium tellurite glass was dominated by surface crystallisation, and (ii) thermal annealing of the glasses recalibrated the redox equilibrium between oxygen ions in the glass and in the atmosphere, resulting in pockets of oxygen within the glass-ceramics. A way to circumvent these two problems might be to investigate a glass series where homogenous bulk crystallisation is favoured. Electronic conductivity data for another series potentially support the findings of a linear relation between the overlap of the electron wave functions between potential jump sites and the electron jump frequency.

A complete description of the transport properties in glass has hitherto been impossible, mostly due to the non-linear property deviations encountered in both the mixed modifier and the mixed network former glasses. The structure-property relations elucidated in the present Ph.D. thesis provide insights into the transport processes, and help gain a better fundamental understanding of transport mechanisms in glass. However, there is a lot of work to be done in the future in order to obtain a coherent picture of transport processes in inorganic glass.

7. Conclusion

We have achieved a better overall understanding of transport processes in inorganic glass. In detail, we have focused on three main transport processes and; (i) clarified the influence of critical parameters such as degree of crystallinity, redox state of carrier, and carrier concentration on electronic conductivity. (ii) clarified the influence of electron and ion motion in regard to bulk properties and structure of glass, and (iii) investigated the link between Vickers hardness, properties related to structural rearrangement, and deformation processes under indentation.

The structural dependence of electronic conductivity was investigated in two vanadium tellurite series. We found a strong correlation between the valence state of the vanadium (c) and glass properties related to the connectivity of the network, i.e., hardness (H_v) and liquid fragility (m). We proposed the existence of a critical vanadia concentration in binary vanadium tellurite equal to 45 mol%, and explained the compositional trends in H_v and m by the structural arrangement around a V^{4+} resulting in a more constrained structure than that surrounding a V^{5+}. The structural change in coordination configuration of vanadium, going from V^{5+} to V^{4+}, results in fewer constraints per unit volume and therefore lower H_v and higher m.

In an attempt to control c, we found a direct proportionality between c and the melting temperature of glass formation (T_H). If the linear relation between c and T_H persists at higher V^{4+} concentrations, it enables for property tailoring and tuning only via the melting temperature of the glass forming melt.

We found a good correlation between the overlap of the electron wave functions between potential jump sites and the electron jump frequency. That is, the electron hopping distance is directly proportional to the activation energy for hopping, and to electronic conductivity at a given temperature. The electronic conductivity occurred strictly adiabatic and showed a linear relation to the average jump distance, but a non-linear relation to c. If the decoupling of electronic conductivity from c, and the strong influence of c on H_v and m, are universal, they enable optimization of H_v and m independent from the electronic conductivity, which potentially has technical value. Out of the three critical parameters for electronic conduction (redox state of carrier, distance between carriers, and activation energy) we found c to experience the lowest influence on the electronic conductivity.

In an attempt to obtain the theoretical high electronic conductivity of the crystal and the high intercalation strength of the glass in one glass-ceramic, we investigated the electronic conductivity as a function of crystallinity. We found find that the electronic conductivity of vitreous $2TeO_2$-V_2O_5 was up to 1.5 orders of magnitude higher than that of the corresponding crystal and thus proposed that vanadium tellurite glass is more suitable for electrochemical devices than a glass-ceramic.

In the clarification of the influence of electron and ion motion in regard to bulk properties and structure of glass, we found that the structural trademark of the mixed modifier effect results in a universal negative deviation from linearity in glass transition temperatures (T_g) and m, but is not encountered in measurements of elastic moduli. As both T_g and m are measures related viscosity their compositional scaling are explained by structural modifications occurring on a microscopic level. Elastic moduli are macroscopic properties, as their measurements involve constrained movement of the glass. The network formers of the glass are thus forced to budge, facilitating

movement via the strongest bonds of the network. We found that the mixed modifier effect universally creates weaker bonding in the vicinity of the network modifying ions, while it increases the amount of tetrahedrally bonded silica units. We inferred that the decrease in viscosity was not related to the network connectivity, but instead was related to the local structural environment around the network modifiers causing overall bond weakening The negative deviations from linearity in T_g are thus explained by the overall weaker bonding surrounding the network modifiers, while the negative deviations from linearity in m are explained by the increase in linked tetrahedral units. In the mixed network former, i.e., the vanadium tellurite glass, we found a strong correlation between the structure and the resulting properties, evident in the compositional scaling of density, viscosity, and elastic moduli.

In the investigation of links among Vickers hardness, properties related to structural rearrangement, and deformation processes under indentation we found no correlation between hardness and either elastic deformation or densification under indentation. However, we found a positive correlation between hardness and the plastic flow part of indentation and proposed that hardness of mixed modifier glasses was dominated by the resistance to plastic flow. We also found that Poisson's ratio was a viable index to discriminate between densification and plastic flow, and thus in mixed modifier glass, exhibited good correlation to H_v.

The negative deviations from linearity in T_g and m corresponds to negative deviations from linearity in isokom temperatures, and thus also to negative deviations from linearity in isothermal viscosities. We proposed that the overall bond weakening around the network modifiers was responsible for the negative deviations from linearity in viscosity and consequently in the resistances to plastic flow and in H_v. Meaning that, the mixed modifier effect on viscosity was believed to account for the scaling of H_v. The positive viscosity-hardness relation was only valid for the mixed alkali-alkaline earth and the mixed alkaline earth effects, as unique property scaling of density (ρ) and H_v was observed for the mixed alkali effect, where both ρ and H_v exhibited a positive deviation from linearity. We explained the compositional property scaling of the mixed alkali effect by two opposite scenarios; (i) general bond weakening around the network modifiers (universal among the mixed modifier effect), and (ii) a tight-knit structure caused by dissimilar alkali ions only available at relatively low temperatures (unique for the mixed alkali effect). These two effects counterbalance each other and the positive deviations from linearity in the volume of plastic flow, H_v, ρ, and m are explained by phenomena (ii), while phenomena (i) explained the compositional trend in T_g.

The structure-property relations, regarding transport processes in inorganic glass, elucidated in the present Ph.D. thesis, aid both the scientific community in achieving a better overall understanding of transport processes in glass, and aid the technical community in designing glass with tailored properties for specific applications.

8. Bibliography

1. W. Vogel, *Glass Chemistry*, 2nd edition, Springer-Verlag (1994) ISBN: 3-540-57572-3
2. A.K. Varshneya, *Fundamentals of Inorganic Glass*, 2nd edition, Society of Glass Technology (2006) ISBN: 978-0-12-714970-7
3. K.J. Rao, *Structural Chemistry of Glasses*, 1st edition, Elsevier (2002) ISBN: 0-08-043958-6
4. J.E. Shelby, *Introduction to Glass Science and Technology*, 2nd edition, The Royal Society of Chemistry (2005) ISBN: 0-85404-639-9
5. C.A. Angell, Science **267** (1995) 1924.
6. W.H. Zachariasen, J. Am. Ceram. Soc. **54** (1932) 3841.
7. A.C. Wright, G. Etherington, J.A.E. Desa, R.N. Sinclair, G.A.N. Connell, and J.C. Mikkelsen, J. Non.Cryst. Solids **49** (1982) 63.
8. D.B. Miracle, Nature Mat. **3** (2004) 697.
9. M.J. Cliffle, M.T. Dove, D.A. Drabold, and A.L. Goodwin, Phys. Rev. Lett. **104** (2010) 125501.
10. P.Y. Huang, S. Kurasch, A. Srivastava, V. Skakalova, J. Kotakoski, A.V. Krasheninnikov, R. Hovden, Q. Mao, J.C. Meyer, J. Smet, D.A. Muller, and U. Kaiser, Nano Lett. **12** (2012) 1081.
11. A.N. Cormack, and Y. Cao, Molecular Engineering **6** (1996) 183.
12. G. Ori, M. Montorsi, A. Pedone, and C. Siligardi, J. Non-Cryst. Solids **357** (2011) 2571.
13. J.C. Phillips, J. Non-Cryst. Solids **34** (1979) 153.
14. J.C. Mauro, Am. Ceram. Soc. Bull. **90** (2011) 31.
15. A. Bunde, M.D. Ingram, P. Maass, and N. Ngai, J. Non-Cryst. Solids **131-133** (1991) 1109.
16. J.C. Dyre, P. Maass, B. Roling, and D.L. Sidebottom, Rep. Prog. Phys. **72** (2009) 1.
17. G.N. Greaves, J. Non-Cryst. Solids **71** (1985) 203.
18. G. N. Greaves, and K.L. Ngai, Phys. Rev. B **52** (1995) 6358.
19. D.W. McCall, D.C. Douglass, and E.W. Anderson, J. Chem. Phys. **31** (1959) 1555.
20. J.G. Wijmans, and R.W. Baker, J. Membrane Sci. **107** (1995) 1.
21. A. Dietzel, Z. Elektrochem. **48** (1942) 9.
22. K.L. Ngai, J. Non-Cryst. Solids **203** (1996) 232.
23. M.L.F. Nascimento, and S. Watanabe, Mater. Chem. Phys. **105** (2007) 308.
24. S.R. Elliott, Solid State Ionics **27** (1988) 131.
25. K. Funke, Prog. Solid St. Chem. **22** (1993) 111.
26. D. Wolf, J. Phys. Chem. Solids **40** (1979) 757.
27. M.D. Ingram, C.T: Moynihan, and A.V. Lesiker, J. Non-Cryst. Solids **38 & 39** (1980) 371.
28. M.D. Ingram, and A.H.J. Robertson, Solid State Ionics **94** (1997) 49.
29. A. Bunde, M.D. Ingram, P. Mass, J. Non-Cryst. Solids **172–174** (1994) 1222.
30. T. Holstein, Ann. Phys. **281** (2000) 725.
31. Y. Gao and C. Cramer, Solid State Ionics **176** (2005) 921.
32. A. Mohajerani, and J.W. Zwanziger, J. Non-Cryst. Solids **358** (2012) 1474.
33. A.H. Dietzel, Phys. Chem. Glass. **24** (1983) 172.
34. D.E. Day, J. Non-Cryst. Solids **21** (1976) 343.

35. R.J. Hand, and D.R. Tadjiev, J. Non-Cryst. Solids **356** (2010) 2417.
36. A. Faivre, F. Despetis, F. Guillaume, and P. Solignac, J. Am. Ceram. Soc. **93** (2010) 2986.
37. V.G. Gehlhoff, and M. Thomas, Zeitschr. f. techn. Physik **3** (1926) 105.
38. J.E. Shelby, and D.E. Day, J. Am. Ceram. Soc. **53** (1970) 182
39. J.O. Isard, J. Non-Cryst. Solids **1** (1969) 235.
40. V.Y. Hasegawa, Glastech. Ber. **57** (1984) 177.
41. K. Hirao, M. Yoshimoto, N. Sogo, and K. Tanaka, J. Non-Cryst. Solids **130** (1991) 78.
42. M. Solvang, Y.Z. Yue, and S.L. Jensen, J. Non-Cryst. Solids **345 & 346** (2004) 782.
43. R. Kirchheim, J. Non-Cryst. Solids **328** (2003) 157.
44. B. Roling, and M.D. Ingram, J. Non-Cryst. Solids **265** (2000) 113.
45. H.W. Guo, X.F. Wang, Y.X. Gong, and D.N. Gao, J. Non-Cryst. Solids **356** (2010) 2109.
46. A.K. Varshneya, International Journal of Applied Glass Science **1** (2010) 131.
47. M. Badalassi, L. Biolzi, G. Royer-Carfagni, W. Salvatore, Constr. Build. Mater. 55 (2014) 114.
48. J.O. Byun, B.H. Kim, K.S. Hong, H.J. Jung, S.W. Lee, and A.A. Izyneev, J. Non-Cryst. Solids **190** (1995) 288.
49. G. Tammann, and W. Hesse, Z. Anorg. Allg. Chem. **156** (1926) 245
50. V.M. Goldschmidt, Geochemische Verteilungsgesetze der Elemente. Skr. Nor. VIdensk. Akad. Kl. 1 Mat. Naturvidensk Kl. **8** (1926) 7.
51. A. Smekal, Glastech. Ber. **22** (1949) 278
52. J.E. Stanworth, J. Soc. Glass Technol. **36** (1952) 217.
53. X. Yuan, and A.N. Cormack, J. Non-Cryst. Solids **319** (2003) 31.
54. W.J. Malfait, W.E. Halter, and E. Verel, Chem. Geol. **256** (2008) 269.
55. S.K. Lee, and S. Sung, Chem. Geol. **256** (2008) 326.
56. J. Zhong, and P.J. Bray, J. Non-Cryst. Solids **111** (1989) 67.
57. Q. Zheng, M.M. Smedskjaer, R.E. Youngman, M. Potuzak, J.C. Mauro, and Y.Z. Yue, Appl. Phys. Lett. **101** (2012) 041906.
58. Q. Zheng, M. Potuzak, J.C. Mauro, M.M. Smedskjaer, R.E. Youngman, and Y.Z. Yue, J. Non-Cryst. Solids **358** (2012) 993.
59. C.A. Angell, Solid State Ionics **9-10** (1983) 3.
60. R.M. Hakim, and D.R. Uhlmann, Phys. Chem Glasses **8** (1967) 173.
61. J.M. Stevels, Verres. et. Refract. **5** (1951) 4.
62. P. Maass, and R. Peibst, J. Non-Cryst. Solids **352** (2006) 5178.
63. J.F. Stebbins, Solid State Ionics **112** (1998) 137.
64. J. Swenson, A. Matic, C. Karlsson, L. Börjesson, C. Meneghini, and W.S. Howells, Phys. Rev. B **63** (2001) 132202.
65. H. Lammert, and A. Heuer, Rhys. Rev. B **72** (2005) 214202.
66. C. Huang, and A.N. Cormack, J. Mater. Chem. **2** (1992) 281.
67. B. Vessal, G.N. Greaves, P.T. Marten, A.V. Chadwick, R. Mole, and S. Houde-Walter, Nature **356** (1992) 504.
68. J.D. Martin, S.J. Goettler, N. Fossé, and L. Iton, Nature **419** (2002) 318.
69. A. Winkelmann, Ann. Phys. **49** (1893) 401.
70. P.J. Lezzi, and M. Tomozawa, J. Non-Cryst. Solids **357** (2011) 2086.
71. A. Klonkowski, J. Non-Cryst. Solids **57** (1983) 339.

72. K.U. Hess, D.B. Dingwell, C. Gennaro, and V. Mincione, Chem. Geol. **174** (2001) 133.
73. M. Tylkowski, and D.S. Bauer, J. Non-Cryst. Solids **376** (2013) 175.
74. S.C. Waterson, and W.E.S. Turner, J. Soc. Glass Techn. **18** (1934) 268.
75. R. Terai, J. Non-Cryst. Solids **6** (1971) 121.
76. G. Adam, and J.H. Gibbs, J. Chem. Phys. **43** (1965) 139.
77. I. Avramov, and A. Milchev, J. Non-Cryst. Solids **104** (1988) 253.
78. J.C. Mauro, Y.Z. Yue, A.J. Ellison, P.K. Gupta, and D.C. Allan, Proc. Natl. Acad. Sci. U. S. A. **106** (2009) 19780.
79. G.W. Scherer, J. Am. Ceram. Soc. **75** (1992) 1060.
80. Y.Z. Yue, J. Non-Cryst. Solids **354** (2008) 1112.
81. Y.Z. Yue, J. Non-Cryst. Solids **355** (2009) 737.
82. Q. Zheng, J.C. Mauro, A.J. Ellison, M. Potuzak, and Y.Z. Yue, Phys. Rev. B **83** (2011) 212202.
83. D. Huang, and G.B. McKenna, J. Chem. Phys. **114** (2001) 5621.
84. L.M. Wang, V. Velikov, and C.A. Angell, J. Chem. Phys. **117** (2002) 10184.
85. Y.Z. Yue, R. Ohe, and S.L. Jensen, J. Chem. Phys. **120** (2004) 8053.
86. C.T. Moynihan, A.J. Easteal, and M.A. DeBolt, J. Am. Ceram. Soc. 59 (1976) 12.
87. S. Sakida, S. Hayakawa, and T. Yoko, J. Non-Cryst. Solids **243** (1999) 1.
88. L. Baia, M. Bolboaca, E.S. Yousef, C. Rüssel, F.W. Breitbarth, T.G. Mayerhöfer, and J. Popp, Phys. Chem. Glasses **45** (2004) 178.
89. U. Hoppe, E. Yousef, C. Rüssel, J. Neuefiend, and A.C. Hannon, Solid State Commun. **123** (2002) 273.
90. R.E. Mallawany, J. Mater. Res. **18** (2003) 402.
91. M.M. Smedskjaer, J.C. Mauro, S. Sen, and Y.Z. Yue, Chem Mater. **22** (2010) 5358.
92. D.R. Neuville, and P. Richet, Geochim. Cosmochim. Acta **55** (1991) 1011
93. D.R. Neuville, L. Cormier, V. Montouillout, P. Florian, F. Millot, J.C. Rifflet, and D. Massiot, Am. Mineral. **93** (2008) 1721.
94. F.L. Galeener, J. Non-Cryst. Solids **49** (1982) 53.
95. P. McMillan, Am. Mineral. **69** (1984) 622.
96. S.H. Risbud, R.J. Kirkpatrick, A.P. Taglialavore, and B. Montez, J. Am. Ceram. Soc. **70** (1987) 10.
97. A.K. Katz, J.P. Glusker, S.A. Beebe, and C.W. Bock, J. Am. Ceram. Soc **118** (1996) 5752.
98. B.N. Nelson, and G.J. Exarhos, J. Chem. Phys. **71** (1979) 2739.
99. K. Shimoda, T. Nemoto, and K. Saito, J. Phys. Chem. B **112** (2008) 6747.
100. D.R. Neuville, L. Cormier, D. Massiot, Geochim. Cosmochim. Acta 68 (2004) 5071.
101. T. Rouxel, C.R. Mecanique **334** (2006) 743.
102. A. Makishima, and J.D. Mackenzie, J. Non-Cryst. Solids **12** (1973) 35.
103. C.C. Lin, S.F. Chen, L.G. Liu, and C.C. Li, Mater. Chem. Phys. **123** (2010) 569.
104. N. Soga, J. Non-Cryst. Solids **73** (1985) 305.
105. M. Yamane, and J.D. Mackenzie, J. Non-Cryst. Solids **15** (1974) 153.
106. R. Rouxel, H. Ji, T. Hammouda, and A. Moréac, Phys. Rev. Lett. **100** (2008) 225501.
107. H. Sawasato, S. Yoshida, T. Sugawara, Y. Miura, and J. Matsuoka, J. Ceram. Soc. Japan **116** (2008) 864.

108. Y. Kato, H. Yamazaki, S. Yoshida, and J. Matsouka, J. Non-Cryst. Solids **356** (2010) 1768.
109. R. Roesky, and J.R. Varner, J. Am. Ceram. Soc. **74** (1991) 1129.
110. H. Li, and R.C. Bradt, J. Non-Cryst. Solids **146** (1992) 197.
111. W.C. Oliver, and G.M. Pharr, J. Mater. Res. **7** (1992) 1564.
112. L. Ainsworth, J. Soc. Glass Techn. **38** (1954) 501.
113. M.M. Smedskjaer, J.C. Mauro, Y.Z. Yue, Phys. Rev. Lett. **105** (2010) 115503.
114. S. Deriano, T. Rouxel, M. LeFloch, and B. Beuneu, Phys. Chem. Glasses **45** (2004) 37.
115. K. Hirao, M. Yoshimoto, N. Soga, and K. Tanaka, J. Non-Cryst. Solids **130** (1991) 78.
116. S. Yoshida, J.C. Sanglebæuf, and T. Rouxel, J. Mater. Res. **20** (2005) 3404.
117. K. Greene, M.J. Pomeroy, S. Hampshire, and R. Hill, J. Non-Cryst. Solids **325** (2003) 193.
118. B.I. Sharma, P.S. Robi, and A. Srinivasan, Mater. Lett. **57** (2003) 3504.
119. N. Chopra, A. Mansingh, and P. Mathur, J. Non-Cryst. Solids **146** (1992) 261.
120. W.B. Hillig, *Concerning the creation and stability of pyramidal hardness impression on glass* in Proceedings of VIth International Congress on Glass (1963) 51.
121. E.W. Taylor, Nature **163** (1949) 323.
122. T. Rouxel, H. Ji, J.P. Guin, F. Augereau, and B. Rüffle, J. Appl. Phys. **107** (2010) 094903.
123. F.M. Ernsberger, J. Am. Ceram. Soc. **51** (1968) 545.
124. K.W. Peter, J. Non-Cryst. Solids **5** (1970) 103.
125. D.M. Marsh, Proc. Roy. Soc. A **282** (1964) 33.
126. J.E. Neely, and J.D. Mackenzie, J. Mater. Sci. **3** (1968) 603.
127. A.K. Varshneya, D.J. Mauro, B. Rangarajan, and B.F. Bowden, J. Am. Ceram. Soc. **90** (2007) 177.
128. P. Sellapan, T. Rouxel, F. Celarie, E. Becker, P. Houizot, and R. Conradt, Acta Mater. **61** (2013) 5949.
129. S. Yoshida, Y. Hayashi, A. Konno, T. Sugawara, Y. Miura, and J. Matsouka, Phys. Chem. Glasses: Eur. J. Glass Sci. Technol. B **50** (2009) 63.
130. C. Hermansen, J. Matsouka, S. Yoshida, H. Yamazaki, Y. Kato, and Y.Z. Yue, J. Non-Cryst. Solids 364 (2013) 40.
131. M. Hojamberdiev, and H.J. Stevens, Mater. Sci. Eng. A **532** (2012) 456.
132. M.G. Walls, M.M. Chaudhri, and T.B. Tang, J. Phys. D: Appl. Phys. **25** (1992) 500.
133. J.D. Mackenzie, J. Am. Ceram. Soc. **46** (1963) 461 & 470.
134. S. Yoshida, S. Isono, J. Matsouka, and N. Soga, J. Am. Ceram. Soc. **84** (2001) 2141.
135. J. Malzbender, and G.D. With, J. Mater. Res. **17** (2002) 502.
136. S.V. Hainsworth, H.W. Chandler, and T.F. Page, J. Mater. Res. **11** (1996) 1987.
137. Y. Kato, H. Yamazaki, S. Itakura, S. Yoshida, and J. Matsouka, J. Ceram. Soc. Japan **119** (2011) 110.
138. L.S. Du, J.R. Allwardt, B.C. Schmidt, and J.F. Stebbins, J- Non-Cryst. Solids **337** (2004) 196.
139. A. Winterstein-Beckmann, D. Moncke, D. Palles, E. I. Kamitsos, L. Wondraczek, J. Non-Cryst. Solids **401** (2014) 110.
140. T. Rouxel, J.C. Sanglebæuf, C. Moysan, and B. Truffin, J. Non-Cryst. Solids **344** (2004) 26.
141. H. Mori, H. Matsuno, and H. Sakata, J. Non-Cryst. Solids **276** (2000) 78.

142. N.F. Mott, Adv. Phys **16** (1967) 49.
143. L. Murawski, C.H. Chung, and J.D. Mazkenzie, J. Non-Cryst. Solids 32 (1979) 91.
144. J.T. Devreese, Z. Phys. B **104** (1997) 601.
145. D.M. Eagles, Phys. Rev. **145** (1966) 645.
146. N.F. Mott, J. Non-Cryst. Solids **1** (1968) 1.
147. M.I. Klinger, Rep. Prog. Phys. **31** (1968) 225.
148. I.G. Austin, and N.F. Mott, Adv. Phys. **18** (1969) 41.
149. A. Ghosh, and D. Chakravorty, Phys. Rev. B **48** (1993) 5167.
150. A.P. Schmid, J. Appl. Phys. **39** (1968) 3140.
151. M.P. Kumar, T. Sankarappa, and A.M. Awasthi, Physica B **403** (2008) 4088.
152. T. Sankarappa, M.P. Kumar, G.B. Devidas, N. Nagaraja, and R. Ramakrishnareddy, J. Mol. Struct. **889** (2008) 308.
153. V.K. Dhawan, A. Mansingh, and M. Sayer, J. Non-Cryst. Solids **51** (1982) 87.
154. M.D. Dyar, Am. Mineral. **70** (1985) 304.
155. L.F. Kirkegaard, M. Korsgaard, Y.Z. Yue, and S. Mørup, Glass Sci. Technol. **78** (2005) 1.
156. M. Kaasgaard, P.A.L. Jacobsen, and Y.Z. Yue, J. Da. Ceram. Soc. **6** (2004) 12.
157. M.M. Smedskjaer, and Y.Z. Yue, Appl. Surf. Sci. **256** (2009) 2002.
158. H. Hirashima, D. Arai, and T. Yoshida, J. Am. Ceram. Soc. **68** (1985) 486.
159. H. Hirashima, M. Ide, and T. Yoshida, J. Non-Cryst. Solids **86** (1986) 327.
160. M. Levy, and J.L. Souquet, Mat. Chem. Phys. **23** (1989) 171.
161. A. Huanosta, and A.R. West, J. Appl. Phys. **61** (1987) 5386.
162. M.A. Sidkey, R.E. Mallawany, R.I. Nakhla, and A.A.E. Moneim, J. Non-Cryst. Solids **215** (1997) 75.
163. N.M. Beekmans, and L. Heyne, Electrochim. Acta **2** (1976) 303.
164. J.E. Bauerle, J. Phys. Chem. Solids **30** (1969) 2657.
165. P.G. Bruce, and A.R. West, J. Electrochem. Soc. **130** (1983) 662.

9. List of Publications

9.1. Conference contributions

- Fragility–structure–conductivity relations in vanadium tellurite glass. / Kjeldsen, Jonas; Rodrigues, Ana Candida Martins; Yue, Yuanzheng. Poster presented at 1st Joint Meeting of DGG – ACerS GOMD, Aachen, Germany, May 25-30, 2014.
- Mixed cation effect in sodium aluminosilicate glasses. / Kjeldsen, Jonas; Smedskjær, Morten Mattrup; Mauro, John C.; Youngman, Randall E.; Huang, Liping; Yue, Yuanzheng. Oral presentation at 1st Joint Meeting of DGG – ACerS GOMD, Aachen, Germany, May 25-30, 2014.
- Enhancing the Electronic Conductivity of Vanadium-tellurite Glasses by Tuning the Redox State. / Kjeldsen, Jonas; Yue, Yuanzheng. Oral presentation at 10th Pacific Rim Conference on Ceramic and Glass Technology, San Diego, United States, June 2-6, 2013.
- Crystallisation behavior and electronic conductivity of vanadium tellurite glass-ceramics. / Kjeldsen, Jonas; Yue, Yuanzheng; Rodrigues, Ana Candida Martins. Oral Presentation at XIII PNCS: Thirteenth International Conference on the Physics of Non-Crystalline Solids, Yichang, China, Sept. 16-20, 2012.

9.2. Journal articles

I: J. Kjeldsen, A.C.M. Rodrigues, S. Mossin, and Y.Z. Yue, "Critical V_2O_5/TeO_2 Ratio Inducing Abrupt Property Changes in Vanadium Tellurite Glasses," *J. Phys. Chem. B* **118** (2014) 14942-14948.

II: J. Kjeldsen, M.M. Smedskjaer, J.C. Mauro, and Y.Z. Yue, "Hardness and Incipient Plasticity in Silicate Glasses: Origin of the Mixed Modifier Effect," *Appl. Phys. Lett.* **104** (2014) 051913

III: J. Kjeldsen, M.M. Smedskjaer, J.C. Mauro, and Y.Z. Yue, "On the Origin of the Mixed Alkali Effect on Indentation in Silicate Glasses," *J. Non-Cryst. Solids* **406** (2014) 22-26.

IV: J. Kjeldsen, M.M. Smedskjaer, J.C. Mauro, R.E. Youngmann, L. Huang, and Y.Z. Yue, "Mixed Alkaline Earth Effect in Sodium Aluminosilicate Glasses," *J. Non-Cryst. Solids* **369** (2013) 61-68.

V: J. Kjeldsen, M.M. Smedskjaer, M. Potuzak, and Y.Z. Yue, "Role of Elastic Deformation in Determining the Mixed Alkaline Earth Effect of Hardness in Silicate Glasses," *J. Appl. Phys.* **117** (2014) 034903.

VI: J. Kjeldsen, Y.Z. Yue, C.B. Bragatto, and A.C.M. Rodrigues, "Electronic Conductivity of Vanadium-Tellurite Glass-Ceramics," *J. Non-Cryst. Solids* **378** (2013) 196-200.

VII: M.M. Smedskjær, J.C. Mauro, J. Kjeldsen, and Y.Z. Yue, "Microscopic Origins of Compositional Trends in Aluminosilicate Glass Properties," *J. Am. Ceram. Soc.* **96** (2013) 1436-1443.

Paper I

THE JOURNAL OF PHYSICAL CHEMISTRY B

Article

pubs.acs.org/JPCB

Critical V_2O_5/TeO_2 Ratio Inducing Abrupt Property Changes in Vanadium Tellurite Glasses

Jonas Kjeldsen,[†] Ana C. M. Rodrigues,[‡] Susanne Mossin,[§] and Yuanzheng Yue*[,†,∥]

[†]Section of Chemistry, Aalborg University, DK-9000 Aalborg, Denmark

[‡]Department of Materials Engineering, Federal University of São Carlos, C.P. 676, 13565-905 São Carlos, SP, Brazil

[§]Department of Chemistry, Technical University of Denmark, 2800 Kongens Lyngby, Denmark

[∥]State Key Laboratory of Silicate Materials for Architecture, Wuhan University of Technology, Wuhan 430070, China

ABSTRACT: Transition metal containing glasses have unique electrical properties and are therefore often used for electrochemical applications, such as in batteries. Among oxide glasses, vanadium tellurite glasses exhibit the highest electronic conductivity and thus the high potential for applications. In this work, we investigate how the dynamic and physical properties vary with composition in the vanadium tellurite system. The results show that there exists a critical V_2O_5 concentration of 45 mol %, above which the local structure is subjected to a drastic change with increasing V_2O_5, leading to abrupt changes in both hardness and liquid fragility. Electronic conductivity does not follow the expected correlation to the valence state of the vanadium as predicted by the Mott−Austin equation but shows a linear correlation to the mean distance between vanadium ions. These findings could contribute to designing optimum vanadium tellurite compositions for electrochemical devices. The work gives insight into the mechanism of electron conduction in the vanadium tellurite systems.

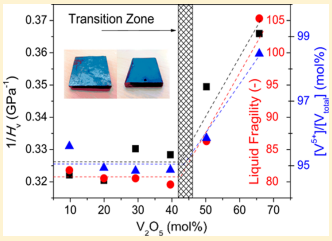

1. INTRODUCTION

Transition metal containing oxide glasses exhibit a unique set of optical and electrical properties.[1−7] Owing to their high electronic conductivity, they have often been applied in electrochemical devices.[8−15] In particular, vanadium tellurite glasses show higher electronic conductivity than other vanadium containing oxide glasses such as phosphates, borates, and silicates[16−21] and therefore have attracted much attention of scientists.[3−9,11−13] The compositional dependence of hardness in the TeO_2−V_2O_5 glass system has been studied to some extent.[22,23] The structure of this glass system has been determined using nuclear magnetic resonance spectroscopy, neutron and X-ray diffraction, and Raman spectroscopy.[24−26] In the vanadium tellurite system, the effect of the composition on glass transition temperature (T_g) has been explored,[3,27,28] and the liquid fragility index (m), i.e., the speed of the viscosity change at T_g upon cooling or heating, has been determined.[3,4] More recently, the electronic conductivity of $2TeO_2$−V_2O_5 glass ceramics was studied as a function of the degree of crystallinity.[29] To the best of our knowledge, a systematic study has not been reported concerning the compositional dependence of both static and dynamic properties of vanadium tellurite glasses. In order to better understand the composition−structure−property relationship of this glass system and thereby tailor its electrochemical performance, it is necessary to perform a thorough study of the dynamic, electrical, and physical properties. Another interesting aspect of this study is to verify whether the vanadium tellurite liquids are indeed so fragile as reported in previous studies.[3,4,29] If this is the case, we should explore the structural origin of the high fragility of these glass liquids.

In this study, we determine the valence state ratio of vanadium (c), m, T_g, Vickers hardness (H_v), density (ρ), electronic conductivity (σ), and glass stability via the Hrüby parameter (K_H) of vanadium tellurite glasses. We focus on the compositional dependences of these properties and explain their structural origin. The knowledge gained from this work could be used for designing vanadium tellurite glass compositions for electrochemical devices.

2. EXPERIMENTAL SECTION

Glass samples were prepared via the melt quenching technique, using reagent grades of ≥99.6% V_2O_5 and ≥99.5% TeO_2. A series of V_2O_5−TeO_2 glasses with various V_2O_5 contents were synthesized by mixing and milling the batches of both oxide materials for 0.25 h, melting them at 800 °C for 0.5 h, quenching the melt on a brass plate, and finally annealing the formed glasses for 2 h at their respective T_g. The amorphous state of all glasses was verified by X-ray diffraction (Rigaku, Ultima IV) using Cu Kα radiation, and their final chemical compositions were determined by energy dispersive X-ray spectroscopy (Phenom). The analyzed chemical compositions are given in Table 1. Compositions are described by the molar percentage of vanadia, namely, $X = [V_2O_5]/([V_2O_5] +$

Received: September 3, 2014
Revised: October 22, 2014
Published: November 27, 2014

Table 1. Chemical Composition of the Six Vanadium Tellurite Glasses with Various V_2O_5 Contents[a]

sample name	V_2O_5 [mol %]
VT_10	9.7
VT_20	19.9
VT_30	29.2
VT_40	39.6
VT_50	50.2
VT_65	65.8

[a]The compositions were analyzed by energy dispersive X-ray spectroscopy (±0.3 mol %).

$[TeO_2]$). Room-temperature density was determined by gas pycnometry (Quantachrome, Ultrapyc 1200e) using helium as pressure gas.

Coplanar samples of each composition were polished and sputtered with gold before electronic conductivity was measured by impedance spectroscopy (Solartron, SI1260). The electrical measurements were performed in air with a two-point sample holder from 303 to 523 K and with an applied voltage of 100 mV in the frequency range from 10^6 to 1 Hz. Impedance data were plotted in an impedance complex plane (Nyquist diagram) and fitted by an equivalent circuit consisting of one resistor in parallel with one capacitor. The dc resistances (R_s) were thus determined by the intercept of the semicircle to the real axis at low frequency. σ was calculated as $\sigma = (1/R_s)(l/S)$ (l and S are the thickness and the surface area of the sample in contact with the electrode, respectively). H_v was measured via a Knoop pyramid indenter (Duramin, Struers). A total of 30 indents were made on each sample using an indentation time of 10 s and an indentation load of 0.25 N. The measurements were performed in air at room temperature.

The liquid fragility indices were determined by a linear fitting of the viscosity data around T_g. The viscosities in the range of $\eta = 10^{11}-10^{13}$ Pa s were measured using a ball penetration viscometer (Bähr, Vis 405). For each data point, a minimum of five penetrations were made at a specific temperature. The pressing ball was made of silica. Press depth was 300 μm, and the press load was between 2 to 9 N.

Calorimetric measurements were performed on a differential scanning calorimeter (DSC) (Jupiter 449C, Netzsch) in order to determine the calorimetric glass transition temperature (T_g), the crystallization onset temperature (T_c), the melting onset temperature (T_m), and the isobaric heat capacity jump during the glass transition (ΔC_p). Each sample was initially subjected to an upscan to 700 °C at 10 K/min in order to determine T_c and T_m. Subsequently each composition is subjected to a downscan and an upscan at 10 K/min to approximately 100 K above T_g. The first upscan curves reflect the thermal history of an unknown cooling rate, whereas the second upscan curves reflects the standard thermal history of a cooling of 10 K/min during the first downscan.[30] A flow of 40 mL/min argon was used as protective gas, and gold crucibles were used for both sample and reference. Both T_g and ΔC_p were determined from the second upscan. In order to calculate the isobaric heat capacity (C_p) of the vanadium tellurite glasses, a 63 mg sapphire standard was utilized.

The concentration of V^{4+} was determined by electron paramagnetic resonance (EPR) spectroscopy. For each sample approximately 20 mg of powder was measured at room temperature in a Bruker EMX X-band EPR spectrometer with an ER 4102ST cavity and a Gunn-diode microwave bridge. The spectra were obtained from 2850 to 3500 G at microwave frequency 9.58 GHz, microwave power 6.31 mW, modulation frequency 100 kHz, and modulation width 8 G and were accumulated over 10 sweeps. Identical settings were used for five standards containing known concentrations of $VO(SO_4)\cdot 3H_2O$ (Sigma-Aldrich) in K_2SO_4 (Sigma-Aldrich).

3. RESULTS

Figure 1 shows the first DSC upscans of the vanadium tellurite glasses. T_c is defined as the crystallization onset temperature,

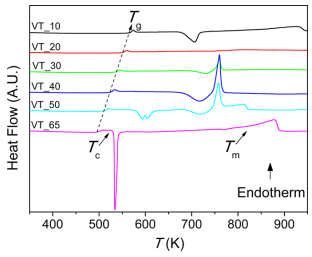

Figure 1. Differential scanning calorimetry upscans at 10 K/min of the vanadium tellurite glasses. Curves are translated on the ordinate for comparison. An example of the determination of the characteristic calorimetric temperatures (T_g, T_c, and T_m) is shown in the inset of Figure 2

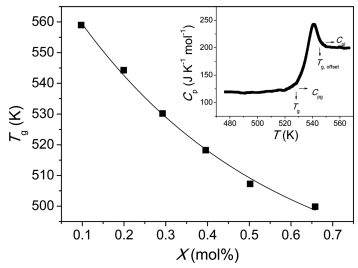

Figure 2. Glass transition temperature (T_g) as a function of X ($=[V_2O_5]/([V_2O_5] + [TeO_2])$) of the vanadium tellurite glasses. The solid line is a guide for the eye showing the compositional scaling of T_g. Inset: Determination of the C_p jump during the glass transition, i.e., $\Delta C_p = C_{pl} - C_{pg}$,[30] taking the 30 mol % V_2O_5 glass as an example. The error range of the T_g values is ±2−3 K.[31]

whereas T_m is determined as the onset temperature of the melting peak. Figure 2 demonstrates the nonlinear dependence of T_g on the V_2O_5 content of the vanadium tellurite glasses. The inset illustrates how to determine the C_p jump during the glass transition, i.e., $\Delta C_p = C_{pl} - C_{pg}$, where C_{pl} and C_{pg} respectively are the isobaric heat capacities of the liquid and the glass at T_g. ΔC_p is a measure of the thermodynamic liquid fragility.[31] The C_p curves for all glasses are shown in Figure 3. On the basis of the characteristic temperatures obtained in Figure 1, the Hrüby parameter (K_H) is determined. K_H is a measure of the glass stability against crystallization as determined by the following equation, which has a positive relation with the glass forming ability of a given system:[32−34]

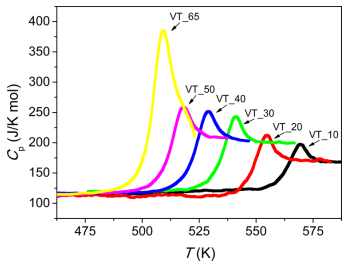

Figure 3. Isobaric heat capacity (C_p) as a function of temperature (T), which was determined during the second DSC upscans at 10 K/min following the prior downscan at 10 K/min for the six vanadium tellurite glasses under study (see Table 1).

$$K_H = \frac{T_c - T_g}{T_m - T_c} \quad (1)$$

K_H and ΔC_p values are listed in Table 2. The dependence of K_H on X obeys a gauss distribution with a maximum very close to the congruent composition of V_2O_5–$2TeO_2$.[35]

Table 2. Glass Transition Temperature (T_g), Crystallization Onset Temperature (T_c), Melting Onset Temperature (T_m), Glass Stability Parameter (K_H), and Heat Capacity Jump at T_g (ΔC_p) Obtained from Differential Scanning Calorimetry

sample name	T_g [K]	T_c [K]	T_m [K]	K_H [−]	ΔC_p [J mol^{-1} K^{-1}]
VT_10	559	679	858	0.7	41.2
VT_20	544	688	740	2.8	58.3
VT_30	530	704	750	3.7	82.6
VT_40	518	682	746	2.6	97.1
VT_50	507	578	743	0.4	96.4
VT_65	500	531	746	0.1	191.6

In Figure 4 $c = [V^{4+}]/[V_{total}]$ is plotted as a function of X ($[V_{total}]$ is the total concentration of vanadium, i.e., equal to $[V^{4+}] + [V^{5+}]$). Initially as X increases, $[V^{4+}]/[V_{total}]$ remains constant at around 5%. At $X = 0.45$ an abrupt change in slope occurs, and the $[V^{4+}]/[V_{total}]$ ratio drastically decreases with

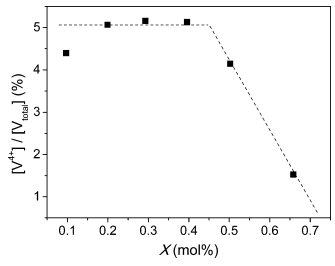

Figure 4. Redox ratio of $[V^{4+}]/[V_{total}]$, where $[V_{total}]$ is the total amount of vanadium ions, as a function of X (=$[V_2O_5]/([V_2O_5] + [TeO_2])$). $[V^{4+}]/[V_{total}]$ is expressed as parameter c in the Mott–Austin equation (eq 3). The dashed line is a guide for the eyes.

further increase in X. $[V^{4+}]/[V_{total}]$ is defined as c of the Mott–Austin equation (eq 3).

Liquid fragility index (m) of the glass systems is determined by a linear fit of the viscosity data around T_g (see inset of Figure 5), i.e., through the following relation:[36]

$$m \equiv \left.\frac{\partial(\log \eta(T))}{\partial(T_g/T)}\right|_{T=T_g} \quad (2)$$

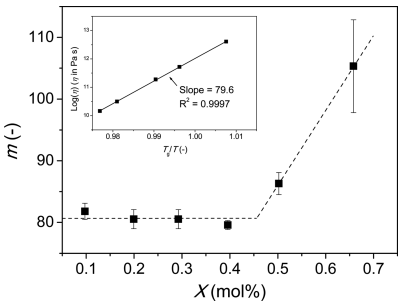

Figure 5. Liquid fragility index (m) as a function of the molar concentration X (=$[V_2O_5]/([V_2O_5] + [TeO_2])$). Inset: Determination of m using eq 2 by taking the 40 mol % V_2O_5 containing glass as an example. The dashed line is a guide for the eyes showing the compositional scaling of m.

The dependence of m on V_2O_5 content is illustrated in Figure 5. m remains unchanged at ∼80 for X between 0.1 and 0.45 but drastically increases linearly up to m = 105 when X increases from 0.45 to 0.65. Supposing that this trend continues, vitreous V_2O_5 would have an m value of 147.

Since H_v strongly depends on the condition of indentation,[37,38] all microindentation experiments were performed with the same indentation load and time (0.25 N and 10 s), ensuring crack free indents. The H_v values are plotted in Figure 6 as a function of X. H_v remains constant when X increases from 0.1 to 0.45, followed by a linear decrease with further increasing X from 0.45 to 0.65. Considering the experimental error associated with the hardness determinations, the compositional hardness scaling agrees with that reported in

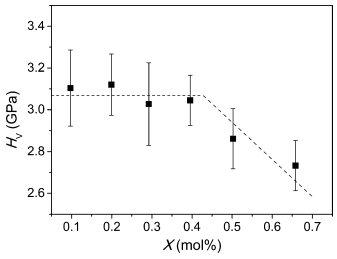

Figure 6. Vickers hardness (H_v) as a function of X (=$[V_2O_5]/([V_2O_5] + [TeO_2])$) of the six vanadium tellurite glasses. The dashed line is a guide for the eye.

literature,[22,23] viz., a decrease in H_v with increasing X. The compositional behavior of H_v (Figure 6) resembles that of c (Figure 4), i.e., an initial plateau followed by a decrease with further increase in X.

Room temperature density and molar volume (V_m) are presented in Figure 7. V_m is calculated as the molar mass divided by the glass density. Density exhibits a linear decrease with increasing X, whereas the molar volume increases nonlinearly.

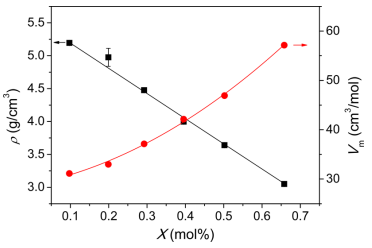

Figure 7. Room temperature density (ρ) and molar volume (V_m) as a function of X (=$[V_2O_5]/([V_2O_5] + [TeO_2])$) for the six vanadium tellurite glasses. Solid lines represent the trends in the respective properties.

Electronic conductivity of glasses containing transition metal oxide is evaluated via the Mott−Austin equation (eq 3).[42,43]

$$\sigma = \left(\frac{\nu_0 e^2}{Rk_bT}\right) c(1-c)\, e^{-2\alpha R}\, e^{-W/(k_bT)} \tag{3}$$

where ν_o is the optical phonon frequency, R is the mean distance between the ions where the electron transfer occurs (vanadium ions in this case), α is the tunneling factor, and W is the activation energy. The parameters of the Mott−Austin equation can be determined by plotting $\log(\sigma T)$ vs $1000/T$ and fitting eq 3 to each set of conductivity data. This is performed in Figure 8, and the derived parameters are shown in Table 3. In order only to have two fitting parameters (namely, α and ν_0),

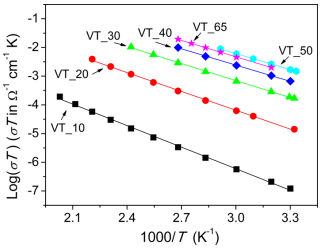

Figure 8. Logarithm of electronic conductivity times temperature ($\log(\sigma T)$) as a function of inverse temperature ($1000/T$) for the vanadium tellurite glasses. The sample identities are indicated in the figure, and the compositions are tabulated in Table 1. The Mott−Austin equation (eq 3) is fitted to each composition via the least-squares method and plotted as solid lines. Regression data are shown in Table 3.

c and R are determined by EPR and pycnometry, respectively. R is calculated as per eq 4:[44,45]

$$R = \left(\frac{M_W}{2M_e\rho N_v}\right)^{1/3} \tag{4}$$

where M_W is the molar mass, M_e the molar concentration of conductive sites (i.e., vanadium), ρ the density, and N_v Avogadro's constant. R is plotted in the inset of Figure 9 and c values are plotted in Figure 4. In Figure 8 it is seen that the electronic conductivity of the vanadium tellurite glasses increases with X. The observed increase in electronic conductivity with increasing V_2O_5 is in good agreement with that reported elsewhere.[3,5,7−9] In order to better visualize this correlation, electronic conductivity data at 298 K (σ_{298K}), along with W, are plotted in Figure 9 as a function of X. The $\log(\sigma_{298K})$ initially increases with X, while W decreases. Both quantities reach a plateau when X surpasses the critical value of about 0.45.

4. DISCUSSION

The decrease in ρ with increasing X (Figure 7) indicates a looser packing of the atoms, since the molar mass of V_2O_5 is higher than that of TeO_2. The observed increase in V_m implies that V_2O_5 constitutes a less compact structural arrangement. The structural expansion with increasing X causes a decrease in the bond numbers per unit volume, i.e., a decrease of constraints, and hence a decrease in T_g (Figure 2 and Table 2).[46−48] The decrease of ρ and T_g with increasing X has also been reported in previous studies,[3,28,39−41] e.g., T_g drops from 560 to 505 K when V_2O_5 is raised from 10 to 50 mol %.[26] In contrast, the onset temperature of crystallization (T_c) first decreases with X and then increases (Table 2). The melting temperature (T_m) only slightly varies in an irregular manner. Consequently, according to eq 1, the glass stability parameter (K_H) first increases and then decreases with increasing X. The trend manifests itself as a Gaussian distribution of K_H over X with a maximum around X = 0.3 (Table 2). This is consistent with a previous study,[27] but different from another study,[28] where the glass stability is found to linearly increase with increasing X.

Vanadium tellurite glasses have been reported to contain both VO_4 and VO_5 polyhedra,[22−26,46] where V^{4+} primarily exists in tetragonally distorted octahedral coordination,[22,25] and V^{5+} mainly exists in a trigonal bipyramidal configurational (~80%) at low V_2O_5 concentrations. As the V_2O_5 concentration increases, the energetically preferred coordination geometry of V^{5+} however changes from a trigonal bipyramidal coordination at low V_2O_5 concentrations to a 50/50 mixture of trigonal bipyramidal and tetrahedral configuration at high V_2O_5 concentrations.[24,28] By comparison of ρ and c obtained in this work with the structural environment of vanadium in vanadium tellurite glass obtained in literature,[22−26,28] an increase in tetrahedral sites could cause an expansion of the glass network (Figure 7) and consequently decrease the amount of bonds per unit volume (decrease in connectivity and T_g; see Figure 2).[23,28] If all V^{4+} ions are assumed to occupy tetragonally distorted octahedral sites, from Figure 4 we can infer that the fraction of distorted tetrahedral sites starts to drop at X = 0.45.

At a certain c value, the V^{4+} ions start to contribute more constraints to the network than V^{5+}, leading to the onset of both the increase in m (Figure 5) and the drop in H_v (Figure 6) at about X = 0.45. When the fraction of tetragonal V^{4+} sites

Table 3. Electronic Conductivity at 298 K (σ_{298K}), Pre-Exponential Term (σ_0), and Activation Energy (W) of the Mott Equation, Tunneling Factor (α), Phonon Frequency (ν_0), and Adjusted Sum of Squared Errors (SSQE) Determined via Fitting of Eq 3 to Electronic Conductivity Data[a]

sample identification	$\log(\sigma_0)$ [σ_0 in Ω^{-1} cm^{-1}]	W [eV]	$\log(\sigma_{298K})$ [σ_{298K} in Ω^{-1} cm^{-1}]	c [%]	R [nm]	α [cm^{-1}]	ν_0 [s^{-1}]	SSQE [−]
VT_10	1.29	0.50	−7.12	4.40	0.64	1.7×10^{-9}	1.6×10^{10}	0.9980
VT_20	2.37	0.43	−4.97	5.07	0.52	1.0×10^{-8}	1.4×10^{11}	0.9987
VT_30	2.78	0.39	−3.86	5.16	0.47	7.4×10^{-9}	3.2×10^{11}	0.9992
VT_40	3.04	0.37	−3.29	5.13	0.45	2.7×10^{-8}	5.5×10^{11}	0.9996
VT_50	3.36	0.37	−2.88	4.15	0.43	1.0×10^{-8}	1.3×10^{12}	0.9995
VT_65	3.39	0.38	−3.00	1.53	0.42	1.7×10^{-7}	3.7×10^{12}	0.9997

[a] R is the mean distance between vanadium ions (from density data and eq 4), and c is the ratio of V^{4+} to total vanadium (from EPR measurements).

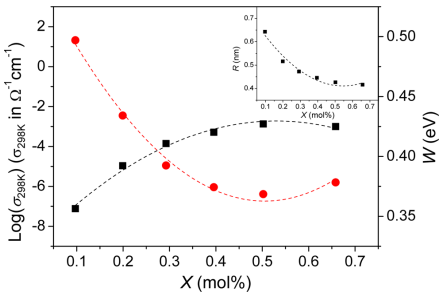

Figure 9. Logarithm of electronic conductivity at 298 K ($\log(\sigma_{298K})$) and activation energy of electronic conduction (W) as a function of X (=$[V_2O_5]/([V_2O_5] + [TeO_2])$). The $\log(\sigma_{298K})$ is plotted in the primary ordinate and W on the secondary. Inset: Mean distance between vanadium ions (R) as a function of X. The dashed lines are guides for the eyes.

starts to decrease, the quantity of the most constrained network diminishes, leading to a decrease in H_v and an increase in m. Sharma et al.[23] measured H_v and c of vanadium phosphate, vanadium tellurite, and vanadium borate glasses and found that in these systems the c value decreases with an increase in X, almost parallel to a 1:1 decrease in H_v. As demonstrated in Figures 5 and 6, the ratio of V^{4+} to total vanadium is seen to have significant impact on both H_v and m. According to Figures 4−6 and a previous work,[23] c is believed to impact the physical and dynamic properties of the studied glass, since it affects the structure of these glasses. For the three different vanadium systems, an approximate 1:1 correlation is found between H_v, m, and c.

A change of c affects the local structural arrangements in the studied glasses and hence results in a mismatch in constraints between the two involved structural arrangements (i.e., V^{4+} in tetragonally distorted octahedral coordination and V^{5+} in a trigonal bipyramidal coordination). As both H_v and m have been shown to linearly depend on the total amount of constraints in the network,[47,48] a direct link might occur between H_v, m, and c. H_v and m are measured at different temperatures, but the structural arrangements that c differentiates between might exhibit a constraint mismatch both at room temperature and at T_g. The m value of the vanadium tellurite glass with 40 mol % V_2O_5 was found by Souri to be 70.[4] This m value is only slightly lower than that shown in Figure 5 considering the relatively large error range of m.

Consistent with the change of the kinetic fragility (m), the C_p jump across the glass transition (ΔC_p) (see Table 2) also increases with increasing X. ΔC_p is a measure of the thermodynamic fragility. This implies that the change of the configurational entropy during the glass transition is associated with that of the valence state of the vanadium. This means that the change of the local structural environment scales with the change in the configurational entropy.

In contrast, electronic conductivity does not show the same compositional trend as H_v and m, indicating that other structural factors rather than c dictates the electronic conductivity. As shown in Figure 9, the electronic conductivity measured at 298 K ($\log(\sigma_{298K})$) initially increases with X and then remains almost unchanged above $X = 0.45$, exactly where c drastically drops. This is surprising, as eq 3 predicts an increase in $\log(\sigma_{298K})$ with increasing c (for $c < 0.5$). The compositional scaling of $\log(\sigma_{298K})$ matches that of the mean distance between vanadium ions (R) (see inset of Figure 9), since eq 3 predicts R and $\log(\sigma_{298K})$ to be inversely proportional. The exact same trend is observed for W (Figure 9), and the linear relation between W and R is well documented for vanadium tellurite glasses.[7,9,49,50] On the basis of Figures 8 and 9, we can infer that the electronic conductivity of the vanadium tellurite glasses depends linearly on R. This is not surprising, as the electron hopping is strictly adiabatic, as $\exp(-2\alpha R) = 1$ for all compositions (see Table 3). In the adiabatic case we expect a linear influence of R on σ. The fact that electron hopping occurs adiabatically in vanadium tellurite glass is in good agreement with former measurements.[44,51,52] In order to achieve higher conductivity, the vanadium ions must thus be brought closer to each other, i.e., an increase in density. This implies that the electronic conductivity is not so dependent on c as predicted by the Mott−Austin equation (eq 3). When c varies, VO_4 and VO_5 polyhedra are interchanging, leading to changes in R. It might be this change in R that facilitates the changes in $\log(\sigma_{298K})$.[9,11,19−21,49,50] For an electrochemical application, e.g., cathode materials in secondary lithium batteries, it is important to optimize the relevant properties such as m, H_v, and σ of the vanadium tellurite glass. This work contributes to establishing the knowledge basis for designing battery materials. Certainly, further studies still need to be done in order to clarify the detailed microscopic mechanism of the abrupt change of the studied properties at the critical V_2O_5 concentration. In particular, a detailed structure analysis by small angle neutron/X-ray diffraction techniques and molecular dynamic modeling will provide additional information on the role of the structure in determining the properties of the vanadium tellurite glass systems.[53,54]

5. CONCLUSION

We have observed a critical V_2O_5 concentration in the vanadium tellurite glasses, above which the local structure undergoes a drastic change, leading to an abrupt change in both physical and dynamic properties.

Hardness and liquid fragility of the studied glasses remain almost unchanged with X when $X < 0.45$. However, when X exceeds 0.45, hardness drops whereas the liquid fragility rises. This means that there is a critical V_2O_5 concentration of $X = 0.45$, above which an abrupt change of the glass properties takes place. The observed trends in hardness and liquid fragility are closely related to the valence ratio of the vanadium ions (c), as c shows the same trend. The reason for this coincidence could be that V^{4+} results in a more constrained structure than V^{5+}, i.e., in fewer constraints per unit volume and hence in lower hardness and higher fragility.

The electronic conduction of vanadium tellurite glasses occurs strictly adiabatically, and σ does not follow the expected correlation to c as predicted by the Mott–Austin equation; instead it exhibits a linear correlation to R. If the decoupling of σ from c also occurs at higher c values, it enables optimization of hardness and liquid fragility without influencing σ.

AUTHOR INFORMATION

Corresponding Author

*Phone: +45 9940 8522. E-mail: yy@bio.aau.dk.

Notes

The authors declare no competing financial interest.

ACKNOWLEDGMENTS

S.M. gratefully acknowledges Carlsbergfondet and the Danish Independent Research Council (Grants DFF-09-070250 and DFF-1335-00175) for supporting the EPR facility at DTU Chemistry. A.C.M.R. acknowledges Fapesp-Cepid, Process No. 2013/07793-6.

REFERENCES

(1) Levy, M.; Souquet, J. L. Amorphous and Vitreous Materials as Electrodes in Electrochemical Cells. *Mater. Chem. Phys.* **1989**, *23*, 171–188.

(2) Lebrun, N.; Levy, M.; Souquet, J. L. Electrical Conductivity in Glasses of the TeO_2-V_2O_5-MoO_3 System. *Solid State Ionics* **1990**, *40/41*, 718–722.

(3) Kumar, M. P.; Sankarappa, T.; Awasthi, A. M. Thermal and Electrical Properties of Some Single and Mixed Transition-Metal Ions-Doped Tellurite Glasses. *Physica* **2008**, *B403*, 4088–4095.

(4) Souri, D. Glass Transition and Fragility of Telluro-Vanadate Glasses Containing Antimony Oxide. *J. Mater. Sci.* **2012**, *47*, 625–631.

(5) Sankarappa, T.; Kumar, M. P.; Devidas, G. B.; Nagaraja, N.; Ramakrishnareddy, R. AC Conductivity and Dielectric Studies in V_2O_5–TeO_2 and V_2O_5–CoO–TeO_2 Glasses. *J. Mol. Struct.* **2008**, *889*, 308–315.

(6) Chopra, N.; Mansingh, A.; Chadha, G. K. Electrical, Optical and Structural Properties of Amorphous V_2O_5-TeO_2 Blown Films. *J. Non-Cryst. Solids* **1990**, *126*, 194–201.

(7) Souri, D. Small Polaron Hopping Conduction in Tellurium Based Glasses Containing Vanadium and Antimony. *J. Non-Cryst. Solids* **2010**, *356*, 2184–2184.

(8) Levy, M.; Rousseau, F.; Duclot, M. J. Electrochemical Properties of Glasses in the TeO_2-V_2O_5 System. *Solid State Ionics* **1988**, *28–30*, 736–738.

(9) Dhawan, V. K.; Mansingh, A.; Sayer, M. DC Conductivity of V_2O_5-TeO_2 Glasses. *J. Non-Cryst. Solids* **1982**, *51*, 87–103.

(10) Chung, C. H.; Mackenzie, J. D. Electrical Properteis of Binary Semiconducting Oxide Glasses Containing 55 Mole % V_2O_5. *J. Non-Cryst. Solids* **1980**, *42*, 357–370.

(11) El-Desoky, M. M. Potassium Doping of Semiconducting Vanadium Tellurate Glasses. *Mater. Chem. Phys.* **2002**, *73*, 259–262.

(12) Jayasinghe, G. D. L. K.; Dissanayake, M. A. K. L.; Careem, M. A.; Souquet, J. L. Electronic to Ionic Conductivity of Glasses in the Na_2O-V_2O_5-TeO_2 System. *Solid State Ionics* **1997**, *93*, 291–295.

(13) Montani, R. A.; Lorente, A.; Vincenzo, M. A. Effect of Ag_2O on the Conductive Behaviour of Silver Vanadium Tellurite Glasses. *Solid State Ionics* **2000**, *130*, 91–95.

(14) Montani, R. A.; Levy, M.; Souquet, J. L. An Electrothermal Model for High-Field Conduction and Switching Phenomena in TeO_2-V_2O_5 Glasses. *J. Non-Cryst. Solids* **1992**, *149*, 249–256.

(15) Kumar, M. P.; Sankarappa, T. DC Conductivity in Some Alkali Doped Vanadotellurite Glasses. *Solid State Ionics* **2008**, *178*, 1719–1424.

(16) Ghosh, A.; Chakravorty, D. Semiconducting Properties of Sol-Gel Derived Vanadium Silicate Glasses. *Appl. Phys. Lett.* **1991**, *59*, 855–856.

(17) Sayer, M.; Mansingh, A. Transport Properties of Semiconducting Phosphate Glasses. *Phys. Rev.* **1972**, *B6*, 4629–4643.

(18) Sharma, B. K.; Dube, D. C.; Mansingh, A. Preparation and Characterization of V_2O_5-B_2O_3 Glasses. *J. Non-Cryst. Solids* **1984**, *65*, 39–51.

(19) Bandyopadhyay, A. K.; Isard, J. O.; Perke, S. Polaronic Conduction and Spectroscopy of Borate Glasses Containing Vanadium. *J. Phys. D: Appl. Phys.* **1978**, *11*, 2559–2576.

(20) Linsley, G. S.; Owen, A. E.; Hayatee, F. M. Electronic Conduction in Vanadium Phosphate Glasses. *J. Non-Cryst. Solids* **1970**, *4*, 208–219.

(21) Munakata, M. Electrical Conductivity of High Vanadium Phosphate Glass. *Solid-State Electron.* **1960**, *1*, 159–163.

(22) Chopra, N.; Mansingh, A.; Mathur, P. Electron Paramagnetic Resonance and Microhardness of Binary Vanadium Tellurite Glasses. *J. Non-Cryst. Solids* **1992**, *146*, 261–266.

(23) Sharma, B. I.; Robi, P. S.; Srinivasan, A. Microhardness of Ternary Vanadium Pentoxide Glasses. *Mater. Lett.* **2003**, *57*, 3504–3507.

(24) Hoppe, U.; Yousef, E.; Rüssel, C.; Neuefeind, J.; Hannon, A. C. Structure of Vanadium Tellurite Glasses Studied by Neutron and X-ray Diffraction. *Solid State Commun.* **2002**, *123*, 273–278.

(25) Baia, L.; Bolboaca, M.; Kiefer, W.; Yousef, E. S.; Rüssel, C.; Breitbarth, F. W.; Mayerhöfer, T. G.; Popp, J. Spectroscopic Studies on the Structure of Vanadium Tellurite Glasses. *Phys. Chem. Glasses* **2004**, *45*, 178–182.

(26) Sakida, S.; Hayakawa, S.; Yoko, T. ^{125}Te and ^{51}V Static NMR Study of V_2O_5–TeO_2 Glasses. *J. Phys.: Condens. Matter* **2000**, *12*, 2579–2595.

(27) El-Moneim, A. A. DTA and IR Absorption Spectra of Vanadium Tellurite Glasses. *Mater. Chem. Phys.* **2002**, *73*, 318–322.

(28) El-Mallawany, R. Glass Transformation Temperature and Stability of Tellurite Glasses. *J. Mater. Res.* **2003**, *18*, 402–406.

(29) Kjeldsen, J.; Yue, Y. Z.; Bragatto, C. B.; Rodrigues, A. C. M. Electronic Conductivity of Vanadium-Tellurite Glass-Ceramics. *J. Non-Cryst. Solids* **2013**, *378*, 196–200.

(30) Yue, Y. Z.; Christiansen, J. D.; Jensen, S. L. Determination of the Fictive Temperature for a Hyperquenched Glass. *Chem. Phys. Lett.* **2002**, *357*, 20–24.

(31) Zheng, Q.; Potuzak, M.; Mauro, J. C.; Smedskjaer, M. M.; Youngman, R. E.; Yue, Y. Z. Composition–Structure–Property Relationships in Boroaluminosilicate Glasses. *J. Non-Cryst. Solids* **2012**, *358*, 993–1002.

(32) Hrüby, A. Evaluation of Glass-Forming Tendency by Means of DTA. *J. Phys. (Paris)* **1972**, *B22*, 1187–1193.

(33) Marques, T. V. R.; Cabral, A. A. Influence of the Heating Rates on the Correlation Between Glass-Forming Ability (GFA) and Glass Stability (GS) Parameters. *J. Non-Cryst. Solids* **2014**, *390*, 70–76.

(34) Nascimento, M. L. F.; Souza, L. A.; Ferreira, E. B.; Zanotto, E. D. Can Glass Stability Parameters Infer Glass Forming Ability? *J. Non-Cryst. Solids* **2005**, *351*, 3296−3308.
(35) Chase, G. A.; Phillips, C. J. Equilibrium in the Glass-Forming System TeO_2-V_2O_5. *J. Am. Ceram. Soc.* **1964**, *47*, 467.
(36) Angell, C. A. Formation of Glasses from Liquids and Biopolymers. *Science* **1995**, *267*, 1924−1935.
(37) Kavetskyy, T.; Borc, J.; Sangwal, K.; Tsmots, V. Indentation Size Effect and Vickers Microhardness Measurement of Metal-Modified Arsenic Chalcogenide Glasses. *J. Optoelectron. Adv. Mater.* **2010**, *12*, 2082−2091.
(38) Schneider, J.-M.; Bigerelle, M. Statistical Analysis of the Vickers Hardness. *Mater. Sci. Eng., A* **1999**, *262*, 256−263.
(39) El-Mallawany, R. Specific Heat Capacity of Semiconducting Glasses: Binary Vanadium Tellurite. *Phys. Status Solidi* **2000**, *177*, 439−444.
(40) Rada, S.; Rada, M.; Cuela, E. Infrared Spectroscopic and DFT Investigations of the Vanadate-Tellurate Glasses Structures. *Spectrochim. Acta* **2010**, *A75*, 846−851.
(41) Sidkey, M. A.; El-Mallawany, R.; Nakhla, R. I.; El-Moneim, A. A. Ultrasonic Studies of $(TeO_2)_{1-x}$-$(V_2O_5)_x$ glasses. *J. Non-Cryst. Solids* **1997**, *215*, 75−82.
(42) Mott, N. F. Electrons in Disordered Structures. *Adv. Phys.* **1967**, *16*, 49−144.
(43) Austin, I. G.; Mott, N. F. Polarons in Crystalline and Non-Crystalline Materials. *Adv. Phys.* **1969**, *18*, 41−102.
(44) Mori, H.; Matsuno, H.; Sakata, H. Small Polaron Hopping Conduction in V_2O_5-Sb-TeO_2 Glasses. *J. Non-Cryst. Solids* **2000**, *276*, 78−94.
(45) Hirashima, H.; Arai, D.; Yoshida, T. Electrical Conductivity of PbO-P_2O_5-V_2O_5 Glasses. *J. Am. Ceram. Soc.* **1985**, *68*, 486−489.
(46) Mauro, J. C. Topological Constraint Theory of Glass. *Am. Ceram. Soc. Bull.* **2011**, *90*, 31−37.
(47) Smedskjaer, M. M.; Mauro, J. C.; Sen, S.; Yue, Y. Z. Quantitative Design of Glassy Materials Using Temperature-Dependent Constraint Theory. *Chem. Mater.* **2010**, *22*, 5358−5365.
(48) Smedskjaer, M. M.; Mauro, J. C.; Yue, Y. Z. Prediction of Glass Hardness Using Temperature-Dependent Constraint Theory. *Phys. Rev. Lett.* **2010**, *105*, 115503.
(49) Mori, H.; Kitami, T.; Sakata, H. Electrical Conductivity of V_2O_5-Bi_2O_3-TeO_2 Glasses. *J. Ceram. Soc. Jpn.* **1992**, *101*, 338−343.
(50) Sakata, H.; Amano, M.; Yagi, T. DC Conductivity of V_2O_5-PbO-TeO_2 Glasses and the Effect of Pressure. *J. Non-Cryst. Solids* **1996**, *194*, 198−206.
(51) Mori, H.; Kitami, T.; Sakata, H. Electrical Conductivity of V_2O_5-Sb_2O_3-TeO_2 Glasses. *J. Non-Cryst. Solids* **1994**, *168*, 157−166.
(52) Moawad, H. M. M.; Jain, H.; Mallawany, R. E.; Ramadan, T.; Sharbiny, M. E. Electrical Conductivity of Silver Vanadium Tellurite Glasses. *J. Am. Ceram. Soc.* **2002**, *85*, 2655−2659.
(53) Matsumoto, H.; Mabuchi, T.; Shigesato, Y.; Yasui, I. Structure Analysis of ZnO-TeO_2 Glasses by Means of Neutron Diffraction and Molecular Dynamics. *Jpn. J. Appl. Phys.* **1996**, *35*, 694−698.
(54) Ori, G.; Montorsi, M.; Redone, A.; Siligardi, C. Insight into the Structure of Vanadium Containing Glasses: A Molecular Dynamics Study. *J. Non-Cryst. Solids* **2011**, *357*, 2571−2579.

Paper II

APPLIED PHYSICS LETTERS **104**, 051913 (2014)

Hardness and incipient plasticity in silicate glasses: Origin of the mixed modifier effect

Jonas Kjeldsen,[1] Morten M. Smedskjaer,[1] John C. Mauro,[2] and Yuanzheng Yue[1,a)]
[1]*Section of Chemistry, Aalborg University, DK-9000 Aalborg, Denmark*
[2]*Science and Technology Division, Corning Incorporated, Corning, New York 14831, USA*

(Received 20 December 2013; accepted 24 January 2014; published online 7 February 2014)

The scaling of Vickers hardness (H_v) in oxide glasses with varying network modifier/modifier ratio is manifested as either a positive or negative deviation from linearity with a maximum deviation at the ratio of about 1:1. In an earlier study [J. Kjeldsen *et al.*, J. Non-Cryst. Solids **369**, 61 (2013)], we observed a minimum of H_v in CaO/MgO sodium aluminosilicate glasses at CaO/MgO = 1:1 and postulated that this minimum is linked to a maximum in plastic flow. However, the origin of this link has not been experimentally verified. In this work, we attempt to do so by exploring the links among H_v, volume recovery ratio (V_R) and plastic deformation volume (V_P) under indentation, glass transition temperature (T_g), Young's modulus (E), and liquid fragility index (m) in CaO/MgO and CaO/Li_2O sodium aluminosilicate glasses. We confirm the negative deviations from linearity and find that the maximum deviation (i.e., the so-called mixed modifier effect) of H_v, T_g, and m is at the modifier ratio of 1:1. These deviations increase in intensity as the total modifier concentration increases. We find a strong correlation between V_P and H_v for the CaO/MgO series, implying that the minimum in H_v originates primarily from an increased shear flow in the mixed modifier glasses.
 [http://dx.doi.org/10.1063/1.4864400]

Hardness is a measure of the ability of a material to resist permanent deformation. It is one of the most important mechanical properties for many applications, such as superhard crystalline abrasive materials[1] and scratch-resistant glass covers for personal electronic devices.[2] However, in glasses, the deformation processes under indentation are complex and not yet fully understood, involving both reversible and irreversible displacements of matter.[3] The study of indentation deformation processes originated in 1962 when Hillig[4] discovered that no single operative process is responsible for the deformation. Later, Neely and Mackenzie[5] found that a portion of the densified volume is recoverable by sub-T_g annealing of the indented glass. According to Yamane and Mackenzie,[6] the resistance of a glass to deformation is a result of three distinct deformation processes: plastic flow, densification, and elastic deformation. Plastic (or shear) flow is a volume conservative displacement of matter, while densification is a non-volume conservative irreversible compression that creates a hemispherical area of increased density beneath the indentation, and elastic deformation a reversible compression that recovers after unloading.[7] Another set of terminology has been proposed by Varshneya *et al.*,[8] separating the deformation into two distinct processes (hydrostatic and deviatoric) each with an elastic component. Yoshida *et al.*[9] have proposed a method to quantify the recoverable part of the indented volume (i.e., densified volume), which in turn provides an indirect measure of the plastic flow. Several studies have applied this method to investigate the link between densification and plastic deformation in borate, phosphate, and silicate glasses, but simultaneous measurements of deformation volumes and Vickers hardness have been performed in only a few studies.[9–15]

Mixed modifier glasses exhibit non-additive variations of certain properties when one modifier oxide species is substituted by another one at constant total modifier content. The composition dependence of Vickers hardness of oxide glasses with varying network modifier/modifier ratio has been reported in the literature as either a positive or negative deviation from linearity with a maximum deviation at the ratio of about 1:1.[16–19] That is, the mixed alkali effect manifests itself as a positive deviation from linearity in hardness,[17] while we have recently reported a minimum in Vickers hardness when substituting Mg for Ca in a series of sodium aluminosilicate glasses.[16] We postulated that this minimum is linked to a maximum in plastic flow. However, the origin of this link has not been experimentally verified and only Yoshida *et al.*[9] have hitherto performed measurements of deformation volumes in a mixed alkaline earth system. In this work, we investigate this possible link in two new series of mixed modifier sodium aluminosilicate glasses by measuring both mechanical and dynamic properties. The measured mechanical properties include Vickers hardness (H_v), Poisson's ratio (ν), elastic moduli (E and G), densification, and plastic flow during indentation, whereas the determined dynamic properties are the glass transition temperature (T_g) and liquid fragility (m). We discuss the origin of the compositional scaling of H_v with varying modifier/modifier ratio in relation to previous literature results and propose an explanation for the observed behavior.

The nominal compositions of the studied mixed modifier aluminosilicate glasses are 60SiO_2-12Al_2O_3-12Na_2O-(16-x)MgO-xCaO where x = {0, 3.2, 6.4, 8, 9.6, 12.8, 16} and 60SiO_2-16Al_2O_3-16Na_2O-(8-y)Li_2O-yCaO where y = {0, 1.6, 3.2, 4.8, 6.4, 8}. The glasses were prepared according to the

a)Author to whom correspondence should be addressed. Electronic mail: yy@bio.aau.dk. Tel.: +45 9940 8522.

TABLE I. Analyzed chemical composition of the 13 sodium aluminosilicate glasses under study. Compositions were analyzed by X-ray fluorescence (±0.1 mol. %).

Glass ID	Composition (mol. %)					
	SiO_2	Al_2O_3	Na_2O	MgO	CaO	Li_2O
Ca-Mg0	59.9	11.9	11.9	0.2	16.0	…
Ca-Mg3.2	60.0	12.0	11.9	3.2	12.7	…
Ca-Mg6.4	59.9	12.0	11.8	6.6	9.6	…
Ca-Mg8	60.2	12.0	11.9	7.9	7.9	…
Ca-Mg9.6	59.6	11.9	11.8	10.0	6.5	…
Ca-Mg12.8	60.2	12.0	11.9	12.6	3.2	…
Ca-Mg16	59.6	11.9	11.8	16.4	0.1	…
Ca-Li0	59.8	16.0	15.8	…	8.1	0.0
Ca-Li1.6	60.0	15.9	15.8	…	6.4	1.6
Ca-Li3.2	59.8	15.9	15.9	…	4.9	3.2
Ca-Li4.8	60.0	15.9	15.9	…	3.2	4.8
Ca-Li6.4	60.1	15.9	15.9	…	1.6	6.4
Ca-Li8	60.0	15.9	15.9	…	0.0	8.0

procedure described in Ref. 16, and the analyzed compositions are given in Table I. The chemical compositions of the glasses were determined using X-ray fluorescence and they were all within 0.5 mol. % of the nominal targets. Measurements of H_v, E, G, ν, m, and T_g are all performed according to the procedures described in Ref. 16. Indentations were performed for 10 s at loads of 0.49 N (Ca-Li series) and 0.25 N (Ca-Mg series). The two different loads were chosen in order to avoid cracking around the indents but still achieve a sufficiently high load to improve measurement accuracy. The indentation impressions were observed using a Ntegra (NT-MDT) atomic force microscope (AFM). Measurements of deformation volumes were conducted only for the Ca-Mg series and performed in tapping mode at 50% relative humidity and room temperature. The AFM cantilever had a silicon tip, the scanning frequency was 0.47 Hz, and the scan size was $20 \times 20\ \mu m^2$. Following the procedure of Yoshida *et al.*,[9] at least ten indentations were examined before and after annealing for 2 h at $0.9T_g$ (in K) of the respective composition. The composition dependences of H_v and E are plotted in Fig. 1 for both series of glasses. H_v exhibits a minimum value (i.e., largest mixed modifier effect) at the substitution degree of 50% for both Ca-Mg and Ca-Li series, which is in good agreement with our previously reported finding in Ref. 16. For the Ca-Mg series, H_v of the magnesium end-member composition is about 0.3 GPa higher than that of the calcium end-member composition (Fig. 1(a)), whereas for the Ca-Li series, the two end-member compositions have similar values of H_v (Fig. 1(b)). The elastic moduli E and G are in both series found to be independent of composition, since the differences in E and G between the compositions are only about 1% (Fig. 1), i.e., within the measurement errors and thus considered negligible. The experimental viscosity data are fitted to the Mauro–Yue–Ellison–Gupta–Allan (MYEGA) equation[20] to obtain the liquid fragility index m.[21] The composition dependencies of m and T_g (measured by differential scanning calorimetry (DSC)) are shown in Fig. 2. Both m and T_g deviate the most from linearity at equal modifier contents, viz., [CaO]/([CaO] + [MgO]) ∼ 0.5 and [CaO]/ ([CaO] + [Li_2O]) ∼ 0.5. For the Ca-Mg series, both T_g and m decrease until reaching a minimum with increasing Ca content (Fig. 2(a)), whereas for the Ca-Li series, the two values increase with increasing concentration of Ca (Fig. 2(b)). Such difference between the two series is likely related to the scenario that Mg^{2+} compared to Li^+ is able to bind to two non-bonding oxygens, thereby creating a more connected network, and thus increasing T_g.[16,22] Therefore, in Fig. 2(a), we see a decrease in T_g as [CaO]/([CaO] + [MgO]) increases.

Based on AFM measurements done on indented Ca-Mg samples, we have determined both the size of the indentation

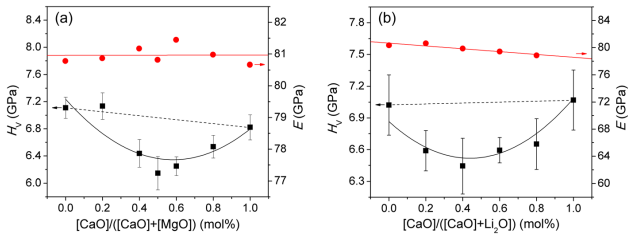

FIG. 1. Composition dependence of Vickers hardness (H_v) and Young's modulus (E) for (a) Ca-Mg and (b) Ca-Li glass series. Solid lines represent the apparent relation, whereas dashed lines are linear extrapolations between end-member compositions, both intended as guides for the eye. H_V is plotted on the primary ordinate and E on the secondary. The error associated with Young's modulus is approximately ±0.2 GPa.

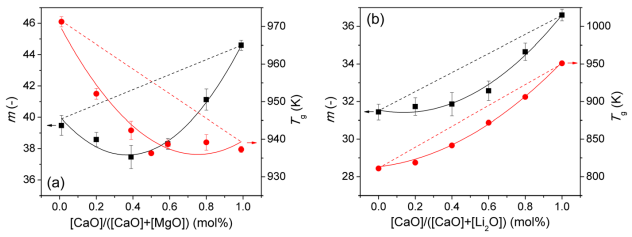

FIG. 2. Composition dependence of liquid fragility index (m) and glass transition temperature (T_g) for (a) Ca-Mg and (b) Ca-Li glass series. m is determined by fitting the MYEGA equation[20] to viscosity data and T_g is obtained from DSC measurements. Solid lines represent the apparent relation, whereas dashed lines are linear extrapolations between end-member compositions, both intended as guides for the eye. m is plotted on the primary ordinate and T_g on the secondary.

and the amount of pile-up before and after annealing. From these results, the volume recovery (V_R) after annealing can be calculated as[9]

$$V_R = \frac{(V_i^- - V_a^-) + (V_a^+ - V_i^+)}{V_i^-}, \quad (1)$$

where subscripts i and a indicate initial volumes and volumes after annealing, respectively. Superscripts $-$ and $+$ indicate indentation volumes and pile-up volumes, respectively. V_R is defined as the ratio of the recovered volume during annealing relative to the initial volume of the indentation, i.e., the ratio of the densified volume relative to the initial indentation volume. The volume of plastic flow (V_P) during indentation is calculated as

$$V_P = V_i^- - ((V_i^- - V_a^-) + (V_a^+ - V_i^+)). \quad (2)$$

V_P and V_R are plotted as a function of the Ca/Mg ratio in Fig. 3. We generally find an increase of V_P and a decrease of V_R as the molar ratio of Ca/Mg increases. In other words, the mixed modifier effect manifests itself as a positive deviation from linearity in V_P and a negative deviation from linearity in V_R. This is visualized in Fig. 4 in which AFM images of indentations before and after annealing of the two end-member compositions are shown. Fig. 4 illustrates that the magnesium end-member composition (Ca-Mg16) experiences a larger pile-up volume after annealing than the calcium end-member composition (Ca-Mg0) does. According to Eq. (2), this results in a lower plastic flow volume, in agreement with the results presented in Fig. 3.

For the studied Ca-Mg and Ca-Li glass series, we find that the mixed modifier effect manifests itself as a positive deviation from linearity in V_P and negative deviation from linearity in T_g, m, V_R, and H_v. In another Ca-Mg glass series,[16] we have also observed that the mixed alkaline earth effect appears as a negative deviation from linearity in T_g, m, and H_v, although those deviations from linearity were not as deep as those reported in this Letter. As shown in Figs. 1 and 2, the observed negative deviations from linearity are not limited to the mixed alkaline earth effect, as they are also found for the Ca-Li series. Considering the size of the

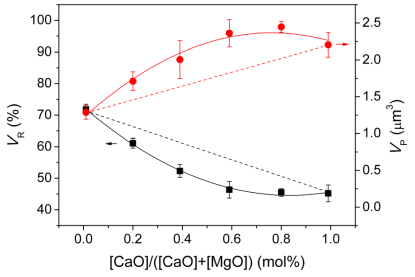

FIG. 3. Composition dependence of volume recovery ratio (V_R) and volume of plastic deformation (V_P) for the Ca-Mg glass series. V_R and V_P are calculated from Eqs. (1) and (2), respectively. Solid lines represent the apparent relation, whereas dashed lines are linear extrapolations between end-member compositions, both intended as guides for the eye. V_R is plotted on the primary ordinate and V_P on the secondary.

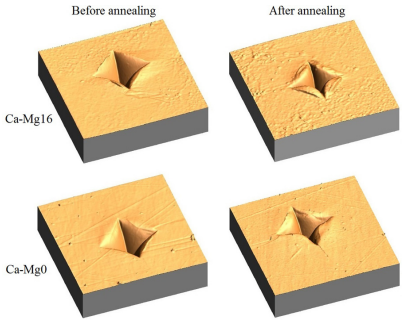

FIG. 4. Atomic force microscopy images of samples Ca-Mg16 and Ca-Mg0 (see Table I) before and after annealing for 2 h at $0.9T_g$ (in K). Images are recorded in tapping mode with a scan size of $20 \times 20\ \mu m^2$.

modifiers, Li^+ is likely to occupy similar positions within the glassy network as Mg^{2+}.[22] When Ca^{2+} ions are exchanged either for Mg^{2+} or Li^+ ions, a difference in site energy arises according to the dynamic structure model[23] and creates the observed negative deviation from linearity in most of the measured properties (Figs. 1–3). The detailed structural origins of these negative deviations from linearity are still under debate, but promising results have been achieved by using topological constraint theory.[24–28] Via constraint theory, Mauro and Varshneya[27] have related the average coordination number of a glass to the physics of indentation with respect to both elasticity and plasticity. Later, Smedskjaer *et al.*[24,25] were able to predict the hardness of borosilicate glasses using temperature-dependent constraint theory.

Fig. 3 shows that V_P increases when Ca is substituted for Mg. This could be due to the stronger oxygen bonding to Mg^{2+} compared to Ca^{2+}, which retards the flow of structural units, i.e., the plastic flow.[22] In other words, the substitution of Ca for Mg may increase the possibility for slip motion of planar structures or redistribution of non-bridging oxygens, which results in an overall increase of the irreversible shear flow (V_P). Considering the measured values of Poisson's ratio (Table II) and the previously reported inverse relationship between Poisson's ratio (ν) and indentation volume recovery (V_R),[7,9] the observed trend in Fig. 3 is in good agreement with those of previous studies.[9,10] As Ca is substituted for Mg, we find that V_P increases approximately linearly with increasing ν (Table II).

TABLE II. Compositional dependence of Poisson's ratio (ν), initial volume of indents (V_i^-), volume of densification (V_d), and volume of plastic flow (V_P) for the Ca-Mg series. ν is calculated from the measured bulk and shear moduli and V_P from atomic force microscopy results. The error associated with volume determinations is approximately $\pm 0.1\ \mu m^3$.

Glass ID	ν (−)	V_P (μm^3)	V_d (μm^3)	V_i^- (μm^3)
Ca-Mg0	0.232	2.2	1.8	4.0
Ca-Mg3.2	0.234	2.4	2.0	4.5
Ca-Mg6.4	0.234	2.4	2.0	4.4
Ca-Mg9.6	0.226	2.0	2.2	4.2
Ca-Mg12.8	0.228	1.7	2.7	4.4
Ca-Mg16	0.222	1.3	3.3	4.6

Yamane and Mackenzie[6] have reported that the resistance of glass to densification is proportional to $(\alpha GK)^{1/2}$, where α is a constant related to bond strength, G is shear modulus, and K is bulk modulus. The resistances to plastic flow and elastic deformation are proportional to αG and K, respectively. In our previous study of a series of mixed Ca-Mg glasses, we postulated that a maximum in V_P should account for the observed minimum in H_v since both densification and elastic deformation were compositionally independent.[16] In this Letter, we also observe that E and ν vary only slightly with composition for both Ca-Mg and Ca-Li series, i.e., K can be regarded as constant for the two studied glass series. Thus, we can regard the elastic deformation contribution to be independent of composition. Furthermore, since V_R is calculated as the densified volume (V_d) divided by the initial indentation volume,[9] V_R is proportional to V_d. As the initial indentation volumes are approximately constant ($V_i^- = 4.3 \pm 0.2\,\mu m^3$, see Table II), the composition dependence of V_R corresponds to that of V_d (Fig. 3). Yoshida *et al.*[9] have argued that V_R is much more sensitive to compositional variations than Vickers hardness, i.e., a relatively large change in V_d (or V_R) results in a relatively small change in H_v. This is in good agreement with the results presented in Figs. 1(a) and 3, as the end-member compositions have values of V_R between 45% and 72% (i.e., 38% relative difference) and of H_v between 7.1 GPa and 6.8 GPa (i.e., 4% relative difference). Hence, densification is not the dominant deformation process in the studied sodium aluminosilicate glasses.

According to Yamane and Mackenzie,[6] the total resistance to indentation deformation is equal to the geometrical average of the three deformation resistances, i.e., the deformation process dictating glass hardness is the one with the largest resistance. As argued above, V_d does not exhibit any correlation with H_v and densification is thus not the dominant deformation process.[6,9] In addition, the elastic deformation is believed to be compositionally invariant. Therefore, the origin of the mixed modifier effect in H_v must be ascribed to the non-linear composition dependence of the resistance to plastic flow. If the plastic flow volume is assumed to be directly related to the corresponding resistance, an increase in V_P will invoke a decrease in H_v. In other words, a lower resistance to plastic flow results in lower glass hardness. This is what has been observed in Figs. 1 and 3, since the minimum in hardness is located at the composition where we find the largest deviation from linearity in V_P. This finding is supported by the previous work of Varshneya *et al.*,[8] who proposed a similar relation to account for the composition dependence of hardness in Ge-Se glasses. The relation between H_v and V_P is further supported by comparing the V_P values of the two end-member compositions in the Ca-Mg series. The Ca end-member composition has a larger V_P than the Mg end-member composition (Fig. 3), which is why H_v of the Ca end-member composition is lower than that of the Mg end-member composition (Fig. 1(a)).

In summary, we have observed negative deviations from linearity in T_g, m, and H_v for two series of Ca-Mg and Ca-Li sodium aluminosilicate glasses. The intensities of these deviations, i.e., the mixed modifier effect, increase when the total modifier concentration increases. By performing AFM analyses of the indented Ca-Mg samples, we have clarified the composition dependences of the indentation volumes (plastic flow vs. densification). We have found a direct link between the volume of plastic flow and the Vickers hardness, suggesting that the origin of the mixed modifier effect of hardness in aluminosilicate glasses is a result of the non-linear composition dependence of the ability of the mixed modifier glasses to resist plastic flow.

We thank the Characterization and Materials Processing Directorate at Corning Incorporated for help with glass preparation and characterization. We also thank C. Hermansen (Aalborg University) for helpful discussions.

[1]Y. Tian, B. Xu, D. Yu, Y. Ma, Y. Wang, Y. Jiang, W. Hu, C. Tang, Y. Gao, K. Luo, Z. Zhao, L.-M. Wang, B. Wen, J. He, and Z. Liu, Nature **493**, 385 (2013).
[2]A. K. Varshneya, Int. J. Appl. Glass Sci. **1**, 131 (2010).
[3]K. I. Nomura, Y. C. Chen, R. V. Kalia, A. Nakano, and P. Vashishta, Appl. Phys. Lett. **99**, 111906 (2011).
[4]W. B. Hillig, "Concerning the creation and stability of pyramidal hardness impression on glass," in *Proceedings of VIth International Congress on Glass,* Washington, July 8–14, 1962 (Am. Ceram. Soc., Westerville, OH, 1963), p. 51.
[5]J. E. Neely and J. D. Mackenzie, J. Mater. Sci. **3**, 603 (1968).
[6]M. Yamane and J. D. Mackenzie, J. Non-Cryst. Solids **15**, 153 (1974).
[7]T. Rouxel, H. Ji, J. P. Guin, F. Augereau, and B. Rufflé, J. Appl. Phys. **107**, 094903 (2010).
[8]A. K. Varshneya, D. J. Mauro, B. Rangarajan, and B. F. Bowden, J. Am. Ceram. Soc. **90**, 177 (2007).
[9]S. Yoshida, J.-C. Sanglebæuf, and T. Rouxel, J. Mater. Res. **20**, 3404 (2005).
[10]P. Sellappan, T. Rouxel, F. Celarie, E. Becker, P. Houizot, and R. Conradt, Acta Mater. **61**, 5949 (2013).
[11]M. Hojamberdiev and H. J. Stevens, Mater. Sci. Eng., A **532**, 456 (2012).
[12]Y. Kato, H. Yamazaki, S. Itakura, S. Yoshida, and J. Matsuoka, J. Ceram. Soc. Jpn. **119**, 110 (2011).
[13]S. Yoshida, Y. Hayashi, A. Konno, T. Sugawara, Y. Miura, and J. Matsuoka, Phys. Chem. Glasses: Eur. J. Glass Sci. Technol., Part B **50**, 63 (2009).
[14]Y. Kato, H. Yamazaki, S. Yoshida, and J. Matsuoka, J. Non-Cryst. Solids **356**, 1768 (2010).
[15]C. Hermansen, J. Matsuoka, S. Yoshida, H. Yamazaki, Y. Kato, and Y. Z. Yue, J. Non-Cryst. Solids **364**, 40 (2013).
[16]J. Kjeldsen, M. M. Smedskjaer, J. C. Mauro, R. E. Youngman, L. Huang, and Y. Z. Yue, J. Non-Cryst. Solids **369**, 61 (2013).
[17]R. J. Hand and D. R. Tadjiev, J. Non-Cryst. Solids **356**, 2417 (2010).
[18]K. Hirao, M. Yoshimoto, N. Soga, and K. Tanaka, J. Non-Cryst. Solids **130**, 78 (1991).
[19]S. Deriano and T. Rouxel, Phys. Chem. Glasses **45**, 37 (2004).
[20]J. C. Mauro, Y. Z. Yue, A. J. Ellison, P. K. Gupta, and D. C. Allan, Proc. Natl. Acad. Sci. U.S.A. **106**, 19780 (2009).
[21]C. A. Angell, Science **267**, 1924 (1995).
[22]R. Kirchheim, J. Non-Cryst. Solids **328**, 157 (2003).
[23]A. Bunde, M. D. Ingram, P. Maas, and K. L. Ngai, J. Non-Cryst. Solids **131–133**, 1109 (1991).
[24]M. M. Smedskjaer, J. C. Mauro, and Y. Z. Yue, Phys. Rev. Lett. **105**, 115503 (2010).
[25]M. M. Smedskjaer, J. C. Mauro, R. E. Youngman, C. L. Hogue, M. Potuzak, and Y. Z. Yue, J. Phys. Chem. B **115**, 12930 (2011).
[26]J. C. Mauro, P. K. Gupta, and R. J. Loucks, J. Chem. Phys. **130**, 234503 (2009).
[27]J. C. Mauro and A. K. Varshneya, J. Am. Ceram. Soc. **90**, 192 (2007).
[28]J. C. Mauro, Am. Ceram. Soc. Bull. **90**, 31 (2011).

Paper III

Journal of Non-Crystalline Solids 406 (2014) 22–26

Contents lists available at ScienceDirect

Journal of Non-Crystalline Solids

journal homepage: www.elsevier.com/ locate/ jnoncrysol

On the origin of the mixed alkali effect on indentation in silicate glasses

Jonas Kjeldsen [a], Morten M. Smedskjaer [a], John C. Mauro [b], Yuanzheng Yue [a,*]

[a] Section of Chemistry, Aalborg University, DK-9000 Aalborg, Denmark
[b] Science and Technology Division, Corning Incorporated, Corning, NY 14831, USA

ARTICLE INFO

Article history:
Received 16 August 2014
Received in revised form 16 September 2014
Accepted 19 September 2014
Available online xxxx

Keywords:
Mixed alkali effect;
Silicate glass;
Vickers hardness;
Indentation;
Plastic flow;
Density

ABSTRACT

The compositional scaling of Vickers hardness (H_v) in mixed alkali oxide glasses manifests itself as a positive deviation from linearity as a function of the network modifier/modifier ratio, with a maximum deviation at the ratio of 1:1. In this work, we investigate the link between the indentation deformation processes (elastic deformation, plastic deformation, and densification) and H_v in two mixed sodium–potassium silicate glass series. We show that the mixed alkali effect in H_v originates from the nonlinear scaling of the resistance to plastic deformation. We thus confirm a direct relation between the resistance to plastic flow and H_v in mixed modifier glasses. Furthermore, we find that the mixed alkali effect also manifests itself as a positive deviation from linearity in the compositional scaling of density for glasses with high alumina content. This trend could be linked to a compaction of the network when two types of alkali ions co-exist.

1. Introduction

Glasses exhibit permanent deformation when subjected to indentation under sharp contact loading (e.g., Vickers diamond indenter). Hardness, which is defined as the applied load divided by the projected area of the deformed region, is the measure of the ability of the glass to resist this permanent deformation. Understanding and predicting the compositional dependence of glass hardness are important for many applications, such as construction materials for architectural purposes [1] and scratch-resistant glass covers for personal electronic devices [2].

One of the most challenging problems in oxide glass science is the understanding of the microscopic origin of the so-called mixed modifier effect. Despite much progress, this problem is still not fully solved [3–7]. The mixed modifier effect refers to non-additive changes of certain properties when one modifier oxide species is substituted by another, keeping the total modifier concentration constant [8]. The compositional dependence of Vickers hardness of mixed modifier oxide glass has been reported as either a positive or negative deviation from linearity with a maximum deviation at the modifier ratio of 1:1 [9–16]. Specifically, the mixed alkali effect of hardness manifests itself as a positive deviation from linearity [9,10,14,15], while the mixed alkaline earth effect and mixed cation effect (the presence of both an alkali and an alkaline earth ion) cause negative deviations from linearity [10–13,16]. Yamane and Mackenzie [17] have proposed a model to account for the composition dependence of hardness, which predicts linear scaling of Vickers hardness with the modifier mixing ratio for all three glass systems (mixed alkali, mixed alkaline earth, and mixed cation). However, this predicted scaling is not in agreement with the experimental observations [9,18].

Recently, Kjeldsen et al. [18] have proposed a new approach for predicting the compositional scaling of Vickers hardness in mixed modifier oxide glasses. In this approach, the compositional dependence of Vickers hardness is assumed to be directly related to the ability of the glass network to resist isochoric structural rearrangement, i.e., plastic flow. The direct correlation between plastic flow and Vickers hardness has been found for various mixed alkaline earth and mixed cation glasses. Bond weakening in the local structural environment around the network modifiers could be responsible for a minimum in the plastic flow volume and thus a minimum in Vickers hardness around the composition with equimolar concentrations of modifier [18]. To examine the validity of the proposed correlation between Vickers hardness and plastic flow further, it is interesting to investigate glass systems exhibiting positive deviation from linearity in Vickers hardness. As mentioned above, this is the case for mixed alkali glasses, and therefore their mechanical and dynamical properties are investigated in this study in order to reveal whether the proposed relation between plastic flow and Vickers hardness is generally applicable for all mixed modifier oxide glass systems. In addition, to the best of our knowledge, the indentation deformation mechanisms in mixed alkali glasses have not yet been elucidated by direct quantification of plastic flow and densification volumes.

In this work, we study two series of mixed Na_2O–K_2O aluminosilicate glasses to reveal the possible relation between plastic flow and Vickers hardness in mixed alkali glasses. We measure Vickers hardness

* Corresponding author.
E-mail address: yy@bio.aau.dk (Y. Z. Yue).

http://dx.doi.org/10.1016/j.jnoncrysol.2014.09.036
0022-3093/

(H_v) by micro-indentation and quantify the volumes of plastic flow and densification by recording atomic force microscopy (AFM) images of the indented areas before and after annealing. Moreover, to understand the observed trends of densification and plastic flow further, we measure properties that are related to each of the deformation processes (elastic deformation, plastic deformation and densification). In particular, we determine the composition dependence of liquid fragility index (m) and glass transition temperatures (T_g), since both of these properties are related to shear motion and thus to plastic flow. The composition dependence of Young's modulus (E) and shear modulus (G) is determined in order to obtain indirect measures of the elastic component of indentation. Finally, the composition dependence of density (ρ) is measured, since ρ is closely related to the densification part of indentation.

2. Experimental

2.1. Sample preparation

The two mixed sodium–potassium aluminosilicate glass series are standard aluminosilicate glass (SiO_2–Al_2O_3–MgO–Na_2O/K_2O) [19] and soda lime float glass (SiO_2–Al_2O_3–MgO–CaO–Na_2O/K_2O) [20] compositions. The standard aluminosilicate series contains relatively high concentration of alumina (>10 mol%), whereas the float glass series contains considerable less alumina (<2 mol%). The total concentration of Na_2O and K_2O was kept constant at ~15 mol% in each glass series. The low-alumina and high-alumina series are referred to as the S and AS series, respectively. The raw materials used for preparing the batches include silica sand, alumina, sodium carbonate, sodium nitrate, potassium carbonate, potassium nitrate, magnesia, limestone, and tin (IV) oxide as a fining agent. The nitrate materials are used to provide an oxidizing environment for tin fining. A total of 15 kg of glass was melted for each composition using a large, platinum-lined melter. The glasses were melted with continuous stirring for 16 h at 1650 °C and delivered through a platinum downcomer at a viscosity of approximately 70 Pa-s. The glasses were pressed in 5 in. × 5 in. × 1 in. graphite molds and transferred to an annealing oven, where they were annealed for at least 8 h at their respective annealing points.

2.2. Indentation

All of the prepared glass samples were polished to mirror image finish and H_v was measured using a Duramin 5 indenter (Struers A/S). A total of 30 indents were conducted on each sample using an indentation time of 10 s and an indentation load of 0.49 N. The measurements were performed in air at room temperature. The indentation impressions were observed using a Ntegra (NT-MDT) atomic force microscope (AFM). Measurements of deformation volumes were performed in tapping mode at 50% relative humidity and room temperature. The AFM cantilever had a silicon tip, the scanning frequency was 0.47 Hz, and the scan size was 20 × 20 μm^2. Following the procedure of Yoshida et al. [16], at least ten indentations were examined before and after annealing for 2 h at 0.9T_g (in K) of the respective composition.

2.3. Temperature dependence of viscosity

The temperature dependence of equilibrium viscosity was measured by performing beam bending, parallel plate, and concentric cylinder experiments. The viscosity curve of each composition is represented by data points at $10^{6.6}$ Pa·s (obtained via parallel plate viscometry), 10^{11} Pa·s (obtained via beam bending viscometry), and 12–20 data points in the range of 10^1 to 10^6 Pa·s (obtained via the concentric cylinder method). For beam bending experiments, bars of 55 mm length and 2.5 × 2.5 mm^2 cross section were cut from the bulk glasses. For parallel plate experiments, cylinders of 6.0 mm diameter and 5.0 mm thickness were core drilled, and afterwards the flats were polished to an optical finish. For concentric cylinder experiments, ~600 g of crushed glass was remelted. The temperature errors associated with determining the 10^{11} Pa·s point by the beam-bending method and the $10^{6.6}$ Pa·s point by the parallel plate method are ±1 and ±2 °C, respectively. The estimated error in viscosity for the high-temperature measurements (by the concentric cylinder method) is $\log(\eta) = \pm 0.02$ (η in Pa·s).

2.4. Elastic moduli and density

The elastic properties (Young's and shear moduli) were measured at room temperature using resonant ultrasound spectroscopy. Prisms of dimensions 10 mm × 8 mm × 6 mm were used to gather resonance spectra from 100 to 300 kHz. For each sample, the first five resonant peaks as a function of frequency resulting from excited resonant eigenmodes were used to calculate the elastic properties. Room-temperature densities of the glasses were determined by Archimedes' principle using water as the immersion liquid.

3. Results

The composition dependences of H_v for the two aluminosilicate glasses series are shown in Fig. 1. Both series exhibit an initial increase followed by a decrease of H_v with increasing Na/K ratio, i.e., the mixed alkali effect of hardness. The largest positive deviation from linearity and the maximum value of H_v are observed at around $[Na_2O] = [K_2O]$. The overall trend shows that glasses from the AS series are harder than those from the S series.

According to Yamane and Mackenzie [17], the resistance of a glass to deformation during indentation is a result of three distinct processes: plastic flow, densification, and elastic deformation. Plastic (or shear) flow is a volume conservative displacement of matter, while densification is a non-volume conservative irreversible compression that creates a hemispherical area of increased density beneath the indent. Elastic deformation is a reversible compression that recovers after unloading [21]. Based on AFM measurements, the size of the indents and the amount of pile-up both before and after annealing are determined. Examples of the measured indents are illustrated in Fig. 2(a–d), along with the calculated pile-up for each indent in Fig. 2(e–h). From these results, the volume

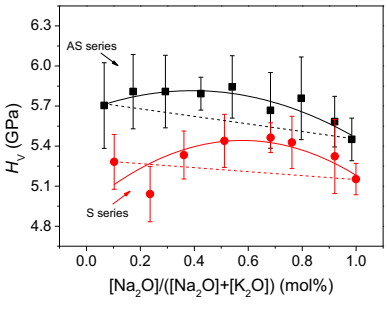

Fig. 1. Vickers hardness (H_v) as a function of the molar ratio of sodium to total alkali content, $[Na_2O]/([Na_2O] + [K_2O])$. The solid lines represent the compositional scaling of H_v, whereas the dashed lines depict a linear relation between the two end-member compositions. Both lines are guides for the eye. Compositions depicted by squares are from the high-alumina series (AS), while compositions depicted by circles are from the low-alumina series (S).

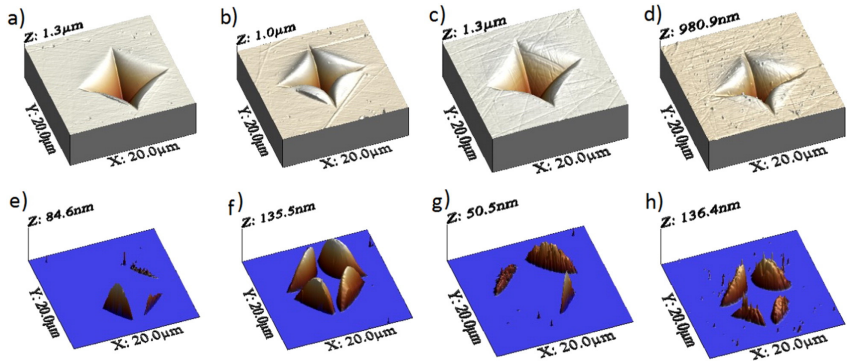

Fig. 2. Atomic force microscopy (AFM) images of indents and their respective pile-ups for the AS series. Material above the surface plane is assigned as pile-up. Images a and b are $[Na_2O]/([Na_2O] + [K_2O]) = 0$ before and after annealing at $0.9\times T_g$ (in K), respectively. Images c and d are $[Na_2O]/([Na_2O] + [K_2O]) = 1$ before and after annealing at $0.9\times T_g$, respectively. Images e–h illustrate the pile-up of the respective indent and are shown for comparison. All images have the same scanning area (20 µm × 20 µm), but the height of the images (z) is different and indicated on each image.

of densification (V_d) and volume of plastic flow (V_p) are calculated as [18]:

$$V_d = \left(V_i^- - V_a^-\right) + \left(V_a^+ - V_i^+\right) \quad (1)$$

$$V_p = V_i^- - \left(\left(V_i^- - V_a^-\right) + \left(V_a^+ - V_i^+\right)\right) \quad (2)$$

where subscripts *i* and *a* indicate initial volumes and volumes after annealing, respectively, and superscripts − and + indicate indentation volumes and pile-up volumes, respectively. Quantification of plastic flow and densification have only been performed on the AS series, and the derived volumes are plotted in Fig. 3. As the $[Na_2O]/([Na_2O] + [K_2O])$ ratio increases, V_d generally increases, whereas V_p generally decreases (Fig. 3). Both V_d and V_p exhibit a mixed alkali effect, viz., negative deviation from linearity with a maximum deviation at around $[Na_2O]/([Na_2O] + [K_2O]) = 0.5$. It is notable that V_d is ~4–5 times larger than V_p. In the inset of Fig. 3, the initial indent volume (V_i^-) is plotted as a function of the Na/K ratio. V_i^- generally increases with increasing $[Na_2O]/([Na_2O] + [K_2O])$, while V_i^- experiences a negative deviation from linearity, largest at around $[Na_2O]/([Na_2O] + [K_2O]) = 0.4$.

To determine the liquid fragility index, *m*, and the glass transition temperature, T_g, we use the measured viscosity data in the range of 10^1 to 10^{11} Pa·s. Those data are fitted to the equation proposed in Ref. [22]:

$$\log \eta(T) = \log \eta_\infty + (12 - \log \eta_\infty)\frac{T_g}{T} \exp\left[\left(\frac{m}{12 - \log \eta_\infty} - 1\right)\left(\frac{T_g}{T} - 1\right)\right] \quad (3)$$

where η_∞ is the high-temperature limit of liquid viscosity. The derived T_g and *m* values are plotted against composition in Figs. 4 and 5, respectively. It is seen in Fig. 4 that T_g decreases with increasing $[Na_2O]/([Na_2O] + [K_2O])$ ratio for both the AS series and the S series. The

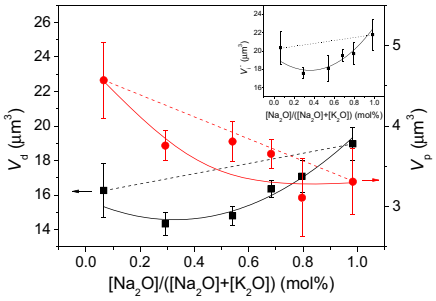

Fig. 3. Volume of densification (V_d) and volume of plastic flow (V_p) as a function of the molar ratio of sodium to total alkali content of the AS series. V_d and V_p are calculated as per Eqs. (1) and (2), respectively. The solid lines represent the compositional scaling, whereas the dashed lines depict a linear relation between the two end-member compositions. Both lines are guides for the eye. Inset: Initial volume (V_i^-) as a function of the molar ratio of sodium to total alkali content of the AS series.

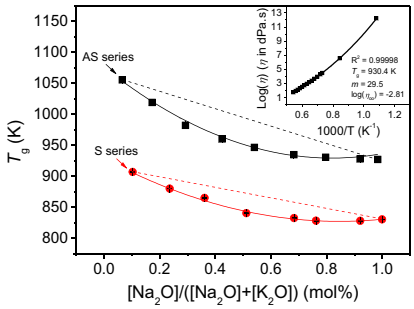

Fig. 4. Glass transition temperature (T_g) as a function of the molar ratio of sodium to total alkali content; $[Na_2O]/([Na_2O] + [K_2O])$. T_g values are determined by fitting the MYEGA-equation (Eq. (3)) to viscosity data. An example of this determination is shown in the inset. The solid lines represent the compositional scaling of T_g, whereas the dashed lines depict a linear relation between the two end-member compositions. Both lines are guides for the eye. Compositions depicted by squares are from the high-alumina series (AS), while compositions depicted by circles are from the low-alumina series (S).

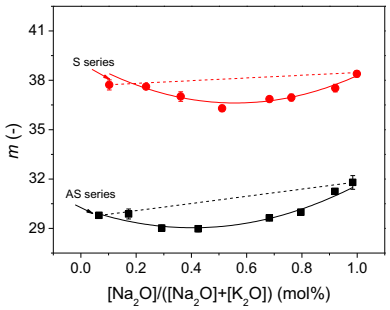

Fig. 5. Liquid fragility indices (m) as a function of the molar ratio of sodium to total alkali content; $[Na_2O]/([Na_2O] + [K_2O])$. m values are determined by fitting the MYEGA-equation (Eq. (3)) to viscosity data. An example of this determination is shown in the inset of Fig. 4. The solid lines represent the compositional scaling of m, whereas the dashed lines depict a linear relation between the two end-member compositions. Both lines are guides for the eye. Compositions depicted by squares are from the high-alumina series (AS), while compositions depicted by circles are from the low-alumina series (S).

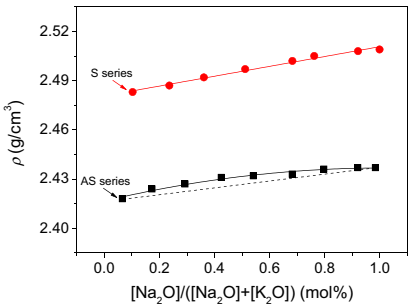

Fig. 7. Density (ρ) as a function of the molar ratio of sodium to total alkali content; $[Na_2O]/([Na_2O] + [K_2O])$. The solid lines represent the compositional scaling of ρ, whereas the dashed line represents a linear relation between the two end-member compositions. Both lines are guides for the eye. Compositions depicted by squares are from the high-alumina series (AS), whereas compositions depicted by circles are from the low-alumina series (S).

decrease is in both cases non-linear and exhibits a negative deviation from linearity, the maximum of which is located around $[Na_2O] = [K_2O]$. Fig. 5 shows that m initially decreases with increasing Na/K ratio, but at equimolar modifier concentration, the compositional trend changes, i.e., m increases with Na/K ratio. The largest negative deviation from linearity is for both series observed at $[Na_2O]/([Na_2O] + [K_2O]) \approx 0.6$. Generally, the glasses from the AS series have higher T_g values (Fig. 4) but lower m values (Fig. 5) than those from the S series.

In Fig. 6, E and G are plotted against the molar concentration of $[Na_2O]/([Na_2O] + [K_2O])$. These elastic moduli generally increase with increasing $[Na_2O]/([Na_2O] + [K_2O])$, showing positive deviations from linearity with maxima at $[Na_2O]/([Na_2O] + [K_2O]) \approx 0.5$. Poisson's ratio ν is calculated as $\nu = E / 2G - 1$ and plotted in the inset of Fig. 6.

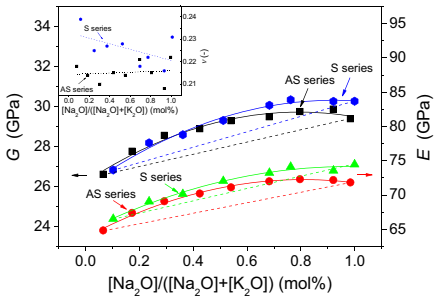

Fig. 6. Shear modulus (G) and Young's modulus (E) as a function of the molar ratio of sodium to total alkali content; $[Na_2O]/([Na_2O] + [K_2O])$. The solid lines represent the compositional scaling of G and E, whereas the dashed lines represent a linear relation between the two end-member compositions. Both lines are guides for the eye. Compositions depicted by squares are from the high-alumina series (AS), while compositions depicted by circles are from the low-alumina series (S). In the inset is Poisson's ratio (ν) as a function of the molar ratio of sodium to total alkali content; $[Na_2O]/([Na_2O] + [K_2O])$. ν is calculated as $\nu = E / 2G - 1$ and the dashed lines are linear fits to data.

Both the AS and the S series are presented with a linear fit, although data are scattered.

Fig. 7 shows the composition dependence of density ρ. ρ is found to increase with increasing Na/K ratio. For the S series, the increase is linear with composition, whereas for the AS series, a small but significant positive deviation from linearity is observed. The glasses from the S series are generally more dense than those from the AS series.

4. Discussion

4.1. Density

We have found that the mixed alkali effect occurs for all of the measured properties (m, T_g, ρ, H_v, V_p, V_d, E, and G), but to a different extent. Interestingly, the densities of the glasses in the AS series exhibit a positive deviation from linearity with the Na/K ratio, whereas densities of the glasses in the S series scale linearly with composition (Fig. 7). ρ is regarded as a static property and thus expected to scale linearly with the ratio of mixed modifiers, unlike the dynamic properties such as conductivity, viscosity, and hardness [8,9]. The linear composition dependence of ρ observed for the S series is in agreement with that reported for some mixed alkali silicate systems [10,23]. However, several studies of both mixed alkali silicate and aluminosilicate systems have shown a positive deviation from linearity in ρ, i.e., similar to what has been observed here for the AS series [8,24–30]. It is noteworthy that the observed positive deviation from linearity is not limited to the mixed sodium–potassium system, but applies to all mixed alkali systems whereas it does not apply to mixed alkaline earth systems [10,26,27,31].

It has been proposed that the positive deviation from linearity in ρ is linked to a tight-knit structure caused by pairs of dissimilar alkali ions [24]. This link, however, does not explain why some systems do not exhibit this mixed alkali effect. The positive deviation from linearity must be directly linked to a compactness of the network when two types of alkali ions co-exist, but the origin of this structural compactness needs to be further explored.

4.2. Indentation

The observed negative deviation from linearity in T_g (Fig. 4) and m (Fig. 5), and the positive deviation from linearity in H_v (Fig. 1) are all in good agreement with previously reported results [8,10,24,26, 29–35]. The maximum in H_v is also in good agreement with the

minimum in V_i^{-} (inset of Fig. 3), since hardness is directly linked to the size of the indent and thus also to its volume [13,17]. In an earlier study, we have proposed that the origin of the mixed modifier effect in H_v is a result of a non-linear composition dependence of the ability of the mixed modifier glasses to resist plastic flow [18]. Since the compositional scaling of V_p exhibits a negative deviation from linearity (Fig. 3), the resistance to plastic flow exhibits a positive deviation from linearity. This positive deviation is in good agreement with the positive deviation from linearity observed in H_v, supporting the ideas proposed in Ref. [18]. Based on the V_d and ρ data (Figs. 3 and 7), the non-linear compositional scaling of H_v (Fig. 1) can be explained by a non-linear increase in the resistance to densification. However, it has been shown that the resistance to densification is not the dominant mechanism when predicting compositional H_v scaling [16,18]. In this study, V_d is found to be approximately four to five times larger than V_p, i.e., the resistance to densification is five times lower than that to plastic flow, assuming proportionality between the densification and plastic flow volumes and their specific resistances. If the three deformation modes (elastic, plastic deformation, and densification) are thought of as parallel springs, the largest resistance should arise from the dominant deformation mode. As all three deformation processes are activated during indentation, their effects are correlated, i.e., not completely decoupled from each other, and hence the deformation mode with largest resistance (plastic flow in our case) is dominant in determining the glass hardness.

The degrees of elastic deformation and densification are not negligible, as it can be realized by comparing the indent volumes of the end-member compositions (i.e., glasses with only one alkali ion present). V_p is higher for the potassium end-member composition than the sodium end-member composition, whereas H_v values for the two end-member compositions are similar. Yoshida et al. [16] have proposed that the ratio between densification and plastic flow is connected with ν (inset of Fig. 6), viz., a higher value of ν results in a higher V_p-to-V_d ratio [13]. The proposed relation between ν and the V_p-to-V_d ratio follows a sigmoidal curve, but for small changes in ν, the relation can be approximated with a proportionality constant (i.e., 1:1 scaling between ν and the V_p-to-V_d ratio). For the AS series, ν slightly increases with increasing $[Na_2O]/([Na_2O] + [K_2O])$, and the V_p-to-V_d ratio is thus also expected to increase with Na/K ratio. This is in contrast to the trend shown in Figs. 2 and 3, where the V_p-to-V_d ratio is found to decrease as $[Na_2O]/([Na_2O] + [K_2O])$ increases.

5. Conclusion

We have shown that in two sodium–potassium aluminosilicate glass series, the mixed alkali effect manifests itself as positive deviations from linearity in hardness and elastic moduli but negative deviations from linearity in glass transition temperature, fragility, and volumes of densification and plastic flow. We show that the maximum in hardness is associated with a minimum in the resistance to plastic flow. This supports the conclusion reported in Ref. [18] concerning the origin of the mixed modifier effect of glass hardness. For the glass series with high alumina concentration, a positive deviation from linearity in density is also found, which should be related to structural compactness around the alkali ions.

References

[1] M. Badalassi, L. Biolzi, G. Royer-Carfagni, W. Salvatore, Constr. Build. Mater. 55 (2014) 114.
[2] A.K. Varshneya, Int. J. Appl. Glass Sci. 1 (2010) 131.
[3] G. Gehlhoff, M. Thomas, Z. Tech. Phys. 3 (1926) 105.
[4] H.W. Guo, X.F. Wang, Y.X. Gong, D.N. Gao, J. Non-Cryst. Solids 356 (2010) 2109.
[5] M.L.F. Nascimento, E. Nascimento, S. Watanabe, Mater. Chem. Phys. 96 (2006) 55.
[6] B. Roling, M.D. Ingram, J. Non-Cryst. Solids 265 (2000) 113.
[7] J.C. Dyre, P. Maass, B. Roling, D.L. Sidebottom, Rep. Prog. Phys. 72 (2009) 046501.
[8] D.E. Day, J. Non-Cryst. Solids 21 (1976) 343.
[9] J. Kjeldsen, M.M. Smedskjaer, J.C. Mauro, R.E. Youngman, L. Huang, Y.Z. Yue, J. Non-Cryst. Solids 369 (2013) 61.
[10] R.J. Hand, D.R. Tadjiev, J. Non-Cryst. Solids 356 (2010) 2417.
[11] K. Hirao, M. Yoshimoto, N. Soga, K. Tanaka, J. Non-Cryst. Solids 130 (1991) 78.
[12] S. Deriano, T. Rouxel, Phys. Chem. Glasses 45 (2004) 37.
[13] P. Sellappan, T. Rouxel, F. Celarie, E. Becker, P. Houizot, R. Conradt, Acta Mater. 61 (2013) 5949.
[14] A. Mohajerani, J.W. Zwanziger, J. Non-Cryst. Solids 358 (2012) 1474.
[15] A. Faivre, F. Despetis, F. Guillaume, P. Solignac, J. Am. Ceram. Soc. 93 (2010) 2986.
[16] S. Yoshida, J.-C. Sanglebæuf, T. Rouxel, J. Mater. Res. 20 (2005) 3404.
[17] M. Yamane, J.D. Mackenzie, J. Non-Cryst. Solids 15 (1974) 153.
[18] J. Kjeldsen, M.M. Smedskjaer, J.C. Mauro, Y.Z. Yue, Appl. Phys. Lett. 104 (2014) 051913.
[19] M.J. Dejneka, A.J. Ellison, J.C. Mauro, Ion Exchangeable Glass with High Compressive Stress, US Patent Application 20130004758 A1 (2013).
[20] A.I. Fu, J.C. Mauro, J. Non-Cryst. Solids 363 (2013) 199.
[21] T. Rouxel, H. Ji, J.P. Guin, F. Augereau, B. Rufflé, J. Appl. Phys. 107 (2010) 094903.
[22] J.C. Mauro, Y.Z. Yue, A.J. Ellison, P.K. Gupta, D.C. Allan, Proc. Natl. Acad. Sci. U. S. A. 106 (2009) 19780.
[23] P.J. Lezzi, M. Tomozawa, J. Non-Cryst. Solids 357 (2011) 2086.
[24] A. Klonkowski, J. Non-Cryst. Solids 57 (1983) 339.
[25] K.U. Hess, D.B. Dingwell, C. Gennaro, V. Mincione, Chem. Geol. 174 (2001) 133.
[26] M. Tylkowski, D.S. Brauer, J. Non-Cryst. Solids 376 (2013) 175.
[27] R.M. Hakim, D.R. Uhlmann, Phys. Chem. Glasses 8 (1967) 174.
[28] R.V. Caporali, J. Am. Ceram. Soc. 47 (1964) 412.
[29] J.O. Isard, J. Non-Cryst. Solids 1 (1969) 235.
[30] S.C. Waterton, W.E.S. Turner, J. Soc. Glass Technol. 18 (1934) 268.
[31] R. Terai, J. Non-Cryst. Solids 6 (1971) 121.
[32] A. Makishima, J.D. Mackenzie, J. Non-Cryst. Solids 12 (1973) 35.
[33] J. Shen, D.J. Green, J. Non-Cryst. Solids 344 (2004) 66.
[34] L. Ainsworth, J. Soc. Glass Technol. 38 (1954) 501.
[35] P.F. Green, R.K. Brow, J.J. Hudgens, J. Chem. Phys. 109 (1998) 7907.

Paper VI

Journal of Non-Crystalline Solids 369 (2013) 61–68

Contents lists available at SciVerse ScienceDirect

Journal of Non-Crystalline Solids

journal homepage: www.elsevier.com/ locate/ jnoncrysol

Mixed alkaline earth effect in sodium aluminosilicate glasses

Jonas Kjeldsen [a], Morten M. Smedskjaer [a], John C. Mauro [b], Randall E. Youngman [b], Liping Huang [c], Yuanzheng Yue [a,*]

[a] Section of Chemistry, Aalborg University, DK-9000 Aalborg, Denmark
[b] Science and Technology Division, Corning Incorporated, Corning, NY 14831, USA
[c] Department of Mat. Sci. Eng., Rensselaer Polytechnic Institute, Troy, NY 12180, USA

ARTICLE INFO

Article history:
Received 4 January 2013
Received in revised form 25 February 2013
Available online xxxx

Keywords:
Aluminosilicate glasses;
Mixed alkaline earth effect;
Hardness;
Viscosity;
Dynamic structure model

ABSTRACT

While the mixed alkali effect has received significant attention in the glass literature, the mixed alkaline earth effect has not been thoroughly studied. Here, we investigate the latter effect by partial substitution of magnesium for calcium in sodium aluminosilicate glasses. We use Raman and NMR spectroscopies to obtain insights into the structural and topological features of these glasses, and hence into the mixed alkaline earth effect. We demonstrate that the mixed alkaline earth effect manifests itself as a maximum in the amount of bonded tetrahedral units and as a minimum in liquid fragility index, glass transition temperature, Vickers microhardness, and isokom temperatures (viz., the temperatures at $\eta = 10^{13.5}$ and $10^{12.2}$ Pa s). The observed minima in fragility, glass transition temperature, and isokom temperature are ascribed to bond weakening in the local structural environment around the network modifiers. We suggest that, since the elastic properties of the investigated system are compositionally independent, the minimum in Vickers microhardness is closely correlated to the minimum in isokom temperatures. Both of these properties are related to plastic flow and the translational motion of structural units, and hence both may be related to the same underlying topological constraints. This indicates that there might not be any significant difference in the onset of the rigid sub-T_g constraints for the investigated compositions.

1. Introduction

Most alkali-containing oxide glasses exhibit non-additive variations of certain properties when one alkali ion is substituted by another one. This phenomenon is known as the "mixed alkali effect" and is one of the most intriguing unsolved phenomena in glass science [1,2]. The mixed alkali effect especially manifests itself in non-additive discrepancies in transport properties, such as diffusion, conductivity, and viscosity. These properties are commonly referred to as dynamic properties, in contrast to static properties such as density, refractive index, and molar volume, all of which exhibit relatively small deviations from linearity [3,4].

The mixed alkali effect has been known for decades, yet over the past few years it is still drawing significant attention [1,5–10]. In contrast, the mixed alkaline earth effect has received relatively little attention. The mixed alkaline earth effect is phenomenologically analogous to the mixed alkali effect, i.e., it concerns substitution of one alkaline earth ion by another one. The influence of the mixed alkaline earth effect on glass properties is also analogous to that of the mixed alkali effect, i.e., deviations from linearity are observed for certain glass properties upon substitution of alkaline earth ions [4,11–14]. Since the mixed alkaline earth effect can affect the glass properties in a non-predictive manner, it is important to study this effect from both scientific and technological points of views.

Although the structural and topological origins of the mixed alkali effect have been the subject of much experimental and modeling work, a thorough understanding of the effect is still lacking [9,15,16]. Despite making progress in interpreting the mixed alkali effect by establishing phenomenological and physical models such as the strong [17,18] and the weak [19–23] electrolyte models, the diffusion controlled relaxation model [24,25], and the jump diffusion model [26], the experimental findings can still not be completely explained by theory. Recently, the introduction of the dynamic structure model [27–30] has helped to establish a more coherent picture [9,10,31–33]. The dynamic structure model is based on an energy landscape approach, in which the unoccupied cationic sites initially are associated with a relatively high potential energy. As the previously unoccupied sites become occupied, the surrounding atoms in the glassy network are ordered. Consequently, different potential energies for these sites are created. When an ion leaves its site, the associated potential energy relaxes back to that of the unoccupied site. Thus, there exists a time window during which the occupation of this site by a similar ion is energetically favored. As the relaxation time and the potential energy associated with the ion site depend on the type of ion, each ion creates its own preferred pathway in the network, and participates in the evolution of the energy landscape [27,30]. Several studies have demonstrated that the mixed alkali effect has a structural origin associated with a cationic potential energy mismatch effect. Such evidence is

* Corresponding author. Tel.: +45 9940 8522.
E-mail address: yy@bio.aau.dk (Y.Z. Yue).

0022-3093/$ – see front matter © 2013 Elsevier B.V. All rights reserved.
http://dx.doi.org/10.1016/j.jnoncrysol.2013.03.015

obtained from X-ray absorption spectroscopy [34,35], nuclear magnetic resonance (NMR) spectroscopy [36,37], infrared spectroscopy [38,39], and neutron and X-ray scattering [40] measurements. The dynamic structure model has been supported by results from both reverse Monte Carlo modeling [40] and molecular dynamics simulations [29,41,42].

The mixed alkaline earth effect has primarily been investigated in silicate and aluminosilicate glasses due to the industrial importance of these systems, e.g., as chemically strengthened cover glasses in personal electronic devices [43] and for modern design purposes [5]. In silicate systems, the glass transition temperature exhibits a negative deviation from linearity when calcium is substituted for magnesium [11,44–46]. Also, in the same system, Vickers hardness has been shown to deviate positively from linearity and the liquid fragility index negatively [5,14,47]. Density, molar volume and the coefficient of thermal expansion all exhibit a linear dependence on composition [5,11]. These results qualitatively agree with those of mixed alkali glasses [4].

In a systematic investigation of glass properties and their dependence of the mixed cationic effect (i.e., when both alkali and alkaline earth ions co-exist), Byun et al. [48] conclude that no "simple mechanism" can be responsible for the observed nonlinearities. Moreover, they point out that the deviation from linearity of certain properties must be intimately connected with microscopic structural changes [48]. Hence, in order to reveal the origin of the observed deviations of glass properties from linearity, the accompanying structural changes must be known [48]. In literature, the mixed alkaline earth effect has been observed as nonlinearities in properties of various silicate [11,13,14,44–47,49,50], phosphate [12,51], and borate glasses [52]. However, to our best knowledge, the correlation between the mixed alkaline earth effect and structural changes has not yet been studied.

In this paper, we investigate both static and dynamic properties of sodium aluminosilicate glasses containing calcium and/or magnesium with respect to the mixed alkaline earth effect. We prepare eight glass compositions with a molar ratio between calcium and magnesium varying from 0 to 1. We measure static properties such as density, molar volume, refractive index, coefficient of thermal expansion, elastic moduli, and Vickers hardness, as well as dynamic properties such as glass transition temperature, configurational heat capacity, and liquid fragility index. The influence of the mixed alkaline earth effect on these properties is discussed based on structural information obtained from room temperature Raman and NMR spectroscopy measurements. Finally, we discuss the mixed alkaline earth effect in terms of topological changes of the networks by considering the dynamic structure model.

2. Experimental procedure

2.1. Sample preparation

The analyzed compositions of the sodium aluminosilicate glasses under study are given in Table 1. All glasses included ~0.16 mol% SnO_2 as a fining agent. To prepare the glasses, the raw materials were first melted in a covered platinum crucible for 5 h in air at a temperature between 1450 and 1600 °C, depending on composition. In order to ensure chemical homogeneity, the melts were first quenched in water, and the resulting glass pieces were crushed and remelted for 6 h at 1650 °C and finally cast onto a stainless steel plate in air. The glasses were annealed for 2 h at their respective annealing points. The chemical compositions of the final glasses were determined using X-ray fluorescence, and the analyzed compositions were all within 0.5 mol% of the nominal targets (Table 1). Room-temperature densities of the glasses were determined by Archimedes' principle using water as immersion liquid.

2.2. Thermal expansion and strain, annealing, and softening points

Analysis of annealing and strain points involves heating a glass fiber of specific dimensions under a specific load (ASTM C336). The fibers were heated to approximately 25 K above their estimated annealing point and then cooled at a rate of 4 K/min. Annealing and strain points ($\eta = 10^{12.2}$ Pa s and $\eta = 10^{13.5}$ Pa s) were then determined as the temperatures that correspond to specific elongation rates, which have been identified by prior analysis of NIST standard glasses. Softening points ($\eta = 10^{6.6}$ Pa s) were determined by heating glass fibers and monitoring their elongation rate under their own weight (ASTM C338). The heating rate was set to 5 K/min and the softening point was defined as the temperature at which the elongation rate was 1 mm/min. Coefficients of thermal expansion (α) were also determined from this experiment, averaged over a temperature range of 25–300 °C.

Table 1
Analyzed chemical composition of the eight sodium aluminosilicate glasses under study. Compositions were analyzed by X-ray fluorescence (±0.1 mol%).

Glass ID	Composition (mol%)				
	SiO_2	Al_2O_3	Na_2O	MgO	CaO
Mg–Ca0	59.92	15.98	15.77	8.08	0.09
Mg–Ca0.8	59.93	15.98	15.83	7.33	0.78
Mg–Ca1.6	60.11	15.96	15.82	6.39	1.57
Mg–Ca2.4	59.91	15.99	15.79	5.76	2.40
Mg–Ca3.2	59.73	16.00	15.75	5.14	3.23
Mg–Ca4.8	59.81	16.02	15.70	3.41	4.90
Mg–Ca6.4	59.85	15.97	15.85	1.65	6.52
Mg–Ca8	59.83	16.01	15.79	0.13	8.08

2.3. Temperature dependence of viscosity

The temperature dependence of equilibrium viscosity was measured by performing beam bending, parallel plate, and concentric cylinder experiments. The viscosity curve of each composition is represented by data points at $10^{6.6}$ Pa s (obtained via parallel plate viscometry), 10^{11} Pa s (obtained via beam bending viscometry), and 12–20 data points in the range of 10^{1} to 10^{6} Pa s (obtained via the concentric cylinder method). For beam bending experiments, bars of 55 mm length and 2.5 × 2.5 mm^2 cross section were cut from the bulk glasses. For parallel plate experiments, cylinders of 6.0 mm diameter and 5.0 mm thickness were core drilled, and afterwards the flats were polished to an optical finish. For concentric cylinder experiments, ~600 g of crushed glass was remelted. The temperature errors associated with determining the 10^{11} Pa s point by the beam-bending method and the $10^{6.6}$ Pa s point by the parallel plate method are ±1 and ±2 °C, respectively. The estimated error in viscosity for the high-temperature measurements (by the concentric cylinder method) is $\log\eta = \pm 0.02$ (η in Pa s).

2.4. Vickers microhardness

All of the prepared glass samples were polished to mirror image finish and Vickers microhardness (H_V) was measured using a Duramin 5 indenter (Struers A/S). A total of 30 indents were conducted on each sample using an indentation time of 10 s and an indentation load of 0.49 N. The measurements were performed in air at room temperature.

2.5. Elastic moduli

The elastic properties (Young's and shear moduli) were measured at room temperature using resonant ultrasound spectroscopy. Prisms of dimensions 10 mm × 8 mm × 6 mm were used to gather resonance spectra from 100 to 300 kHz. For each sample, the first five resonant peaks as a function of frequency resulting from excited resonant eigenmodes were used to calculate the elastic properties.

2.6. Refractive indices

Refractive index (n) measurements were performed at the sodium D-line (589.3 nm) using a low range Precision Refractometer (Bausch & Lomb) with a sodium arc lamp. The measurements were performed on 1.0 mm thick samples with polished surfaces that were cleaned prior to measurements with high purity ethanol. The standard deviation of n is around ± 0.0003.

2.7. Glass transition temperature and isobaric heat capacity

Calorimetric measurements were performed on a differential scanning calorimeter (DSC 449C, Netzsch) to determine the calorimetric glass transition temperature (T_g) and the jump in heat capacity during the glass transition (ΔC_p). Each sample was subjected to two up and downscans at 10 K/min to approximately 100 K above the glass transition temperature. The first scan reflects an unknown thermal history whereas the second scan reflects the standard thermal history of a cooling of 10 K/min [53]. A flow of 40 ml/min argon was used as protective gas and platinum crucibles were used for both sample and reference. In order to calculate the isobaric heat capacity (C_p) of the sodium aluminosilicate glasses, a sapphire standard of approximately the same weight was measured before the measurement of each sample.

2.8. Structural aspects

Raman spectra were collected at room temperature on glass samples that were optically polished to a thickness of 50–80 μm with parallel top and bottom surfaces. Grinding and polishing were done using 600 grit SiC sand paper and cerium oxide slurry. A LabRAM HR800 Raman microscope (Horiba Jobin Yvon) was used to collect the spectra by using a 532 nm Verdi V2 DPSS green laser as the probing light source. The experimental setup is described in detail by Guerette and Huang [54]. Following Refs. [55,56], we have removed the spectral background by fitting a second order polynomial to the spectral region between 1250 and 1550 cm^{-1} (where no Raman bands are present), extrapolating it to lower frequencies and subtracting it from each spectrum.

^{27}Al magic angle spinning (MAS) NMR experiments were conducted at 11.7 T (130.22 MHz resonance frequency) using a commercial spectrometer (VNMRS, Agilent) and a commercial 3.2 mm MAS NMR probe (Varian/Chemagnetics). Powdered glasses were packed into aluminum-free 3.2 mm zirconia rotors with sample spinning at 20 kHz. 0.6 μs radio-frequency pulses, corresponding to a π/12 tip angle, were used to excite the ^{27}Al central transitions uniformly and thus provide quantitatively accurate Al speciation. The ^{27}Al MAS NMR spectra were processed without additional line broadening and referenced to aqueous aluminum nitrate at 0.0 ppm. ^{27}Al MAS NMR spectra were analyzed using the Dmfit program [57]. This program provides a means by which to simulate second-order quadrupolar lineshapes, and in the case of ^{27}Al NMR spectra, an additional parameter (Czjzek distribution) to account for distributions in the quadrupolar interaction [58]. ^{27}Al MAS NMR spectra were fit using this approach and relative peak intensities were determined from numerical integration of the simulated AlO_4 and AlO_5 lineshapes.

3. Results

3.1. Dynamic properties

The viscosity–temperature relationship has been the focus of several models [59–62]. Recently, Mauro et al. [61] proposed a new and improved model. This model is referred to as the "MYEGA" equation. It is founded upon the temperature dependence of configurational entropy [60] via the Adam–Gibbs equation of viscosity [59] and is derived based on topological constraint theory. The model is able to account for the configurational entropy both at the high temperature limit (a problem with the Avramov–Milchev model [60]) and at the low temperature limit (a problem with the Vogel–Fulcher–Tammann model [62]). Another important feature is that all three fitting parameters of the MYEGA model bear a physical meaning. The model is given by Eq. (1),

$$\log\eta(T) = \log\eta_\infty + (12 - \log\eta_\infty)\frac{T_g}{T}\exp\left[\left(\frac{m}{12-\log\eta_\infty} - 1\right)\left(\frac{T_g}{T} - 1\right)\right] \quad (1)$$

where η_∞ is the high-temperature limit of liquid viscosity, T_g is the glass transition temperature, and m is the liquid fragility index. m is defined as the slope of an Angell plot at T_g (Eq. (2)) [63].

$$m \equiv \left.\frac{\partial(\log\eta(T))}{\partial(T_g/T)}\right|_{T=T_g} \quad (2)$$

By fitting Eq. (1) to the experimental viscosity data using a Levenberg–Marquardt algorithm [64,65] (see inset of Fig. 1), we obtain the liquid fragility index and glass transition temperature.

In Fig. 1, m is plotted as a function of the molar ratio of magnesium to total alkaline earth content [MgO] / ([MgO] + [CaO]). We note that two distinct compositional regimes exist. Initially, as calcium is substituted for magnesium, the liquid fragility index decreases. This trend continues until a substitution degree of 0.70 after which the fragility increases upon further substitution. The largest deviation from linearity (the dashed line) is observed at a substitution degree of ~0.63, i.e., the largest mixed alkaline earth effect is observed at a composition close to the one with equal concentrations of the two alkaline earth ions.

Fiber elongation data are presented in Figs. 2 and 3. In Fig. 2, the coefficient of thermal expansion (α), calculated as an average from 25 to 300 °C, is plotted as a function of the molar ratio of magnesium to total alkaline earth content. α exhibits a linear decrease over the entire composition range, with a minimum at a ratio of magnesium to total alkaline earth content equal to 1. The fitted linear tendency has an adjusted coefficient of determination (R^2) equal to 0.960. Isokom temperatures at the softening ($\eta = 10^{6.6}$ Pa s), annealing ($\eta = 10^{12.2}$ Pa s), and strain points ($\eta = 10^{13.5}$ Pa s) are plotted as a function of the molar ratio of magnesium to total alkaline earth content in Fig. 3. The dashed lines are guides for the eye and represent linear tendencies between the end-member glasses, whereas the solid lines represent polynomial fits

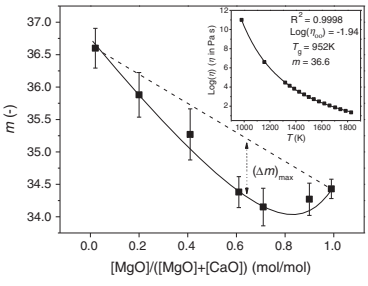

Fig. 1. Liquid fragility index (m) as a function of the molar ratio of magnesium to total alkaline earth content [MgO] / ([MgO] + [CaO]). m is determined by fitting the MYEGA equation (Eq. (1)) to the measured $\log\eta$ vs. T data. The inset shows an example of this determination using data for Mg–Ca8 [61]. The solid line represents the apparent relation between m and the molar ratio of [MgO] / ([MgO] + [CaO]), whereas the dashed line represents a linear relation between the two end-member compositions. Both lines are guides for the eye. $(\Delta m)_{max}$ is equal to the maximum discrepancy in fragility between the linear relation and the apparent relation, i.e., the largest mixed alkaline earth effect.

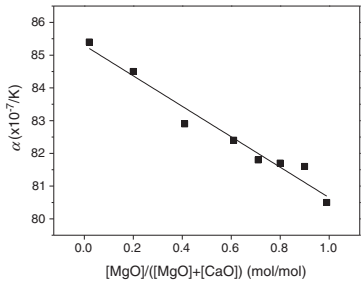

Fig. 2. Coefficient of thermal expansion (α) as a function of the molar ratio [MgO] / ([MgO] + [CaO]). α is taken as the average value between 25 and 300 °C. The solid line is a linear fit to data ($R^2 = 0.960$) and the accuracy of α is approximately $\pm 0.6 \times 10^{-7}$/K.

to all data points. Both the strain and the annealing points generally lie beneath the dashed line, since they exhibit a more parabolic shape, whereas the softening temperatures exhibit linear composition dependence and thus lie on the dashed line. Furthermore, both the straining and annealing isokoms have the largest deviation from linearity at a substitution degree of approximately 0.51. For all three points, the isokom temperature increases as magnesium is substituted for calcium. With an increase in isokom temperature, i.e., a decrease in viscosity, the deviation from linearity becomes less pronounced and approaches zero (Fig. 3). In other words, the mixed alkaline earth effect is declining as the temperature increases.

3.2. Physical properties

Vickers hardness (H_V) is determined by using the microindentation method. Experimental H_V values depend on the measurement conditions [66–69]. Consequently all microindentation experiments have been performed on the same indenter with the same indentation load and time (0.49 N and 10 s), ensuring crack free indents. Fig. 4 shows Vickers microhardness plotted as a function of the molar ratio of magnesium to total alkaline earth content. The dashed line represents a linear relationship between the end-member compositions. A parabolic fit

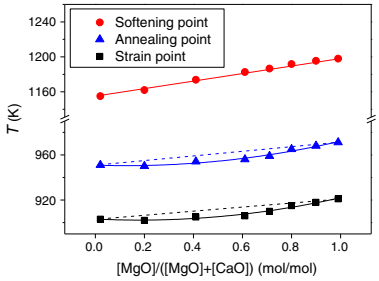

Fig. 3. Strain ($\eta = 10^{13.5}$ Pa s), annealing ($\eta = 10^{12.2}$ Pa s), and softening point ($\eta = 10^{6.6}$ Pa s) as a function of the molar ratio [MgO] / ([MgO] + [CaO]). Data is measured by fiber elongation. The dashed lines represent linear relations between the isokom temperatures and the magnesium to total alkaline earth content. The solid lines are polynomial fits [64,65]. The uncertainty in the determinations of the straining and annealing points are ±2 K and ±3 K for the determination of softening points, i.e., errors are smaller than the size of the symbols.

matches the data well, and the largest deviation from linearity is found at a substitution degree of 0.50.

According to the Yamane and Mackenzie model [70] the elastic moduli control the deformation of glasses during microindentation. Therefore, shear modulus (G) and Young's modulus (E) have been determined and the results are shown in Fig. 5. It is seen that elastic moduli are compositionally invariant within the measured set of glasses, since both shear modulus and Young's modulus are constant within the error range for all measured compositions. Since the glass is isotropic, this means that the bulk modulus and Poisson's ratio must also be constant. In Fig. 6, density and molar volume at room temperature are plotted as a function of the molar ratio of [MgO] to [CaO] + [MgO]. The molar volume is calculated as the molar mass is divided by the glass density. Both density and molar volume exhibit a linear decrease as magnesium is substituted for calcium. The measured refractive indices (n) at 589.3 nm reveal the same linear tendency, i.e., n decreases as magnesium is exchanged with calcium (Fig. 7).

3.3. Thermodynamic fragility

The measured differential scanning calorimetry (DSC) curves are shown in Fig. 8. The composition dependence of the measured difference in heat capacity between supercooled liquid and glass (ΔC_p, an indirect measure of thermodynamic fragility) and glass transition temperatures (T_g) are shown in Figs. 9 and 10, respectively. These values were determined from the C_p–T curves obtained during the second DSC upscan as shown in the inset of Fig. 10 [52]. The dependence of T_g on [MgO] / ([MgO] + [CaO]) deviates negatively from linearity (dashed line), with the largest deviation at a substitution degree of 0.54 (Fig. 10). T_g increases with increasing substitution of calcium for magnesium. The thermodynamic fragility exhibits two regions of composition dependence. At low magnesium concentration, ΔC_p decreases as calcium is substituted for magnesium, whereas at low calcium concentrations, ΔC_p increases. The slope changes from negative to positive at [MgO] / ([MgO] + [CaO]) = 0.70 and the largest deviation from linearity is at [MgO] / ([MgO] + [CaO]) = 0.49.

3.4. Structural aspects

Raman spectra of representative sodium aluminosilicate glasses are shown in Fig. 11, where the Raman intensity is plotted as a function of wavenumber (ν). The two low-wavenumber peaks are both unaffected by composition variations, i.e., all samples have peaks positioned at ~498 cm^{-1} and ~570 cm^{-1}, respectively. According to Galeener [71]

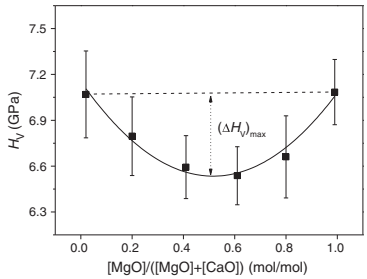

Fig. 4. Vickers microhardness (H_V) as a function of the molar ratio [MgO] / ([MgO] + [CaO]). The solid line represents the apparent relation between H_V and the molar ratio of [MgO] / ([MgO] + [CaO]) whereas the dashed line is a linear extrapolation between the end-member compositions; both are guides for the eye. $(\Delta H_V)_{max}$ is marked on the figure as where the largest discrepancy is between linear relation and apparent relation, i.e., the largest mixed alkaline earth effect.

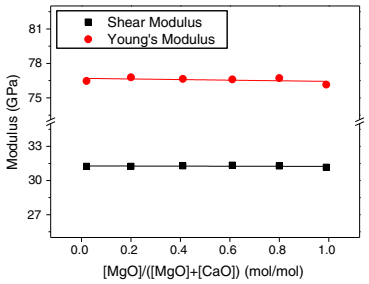

Fig. 5. Elastic moduli as a function of the molar ratio [MgO] / ([MgO] + [CaO]). The solid lines are linear fits. Both Young's modulus and shear modulus are determined by resonant ultrasound spectroscopy experiments. The uncertainty of this method is approximately ±0.2 GPa.

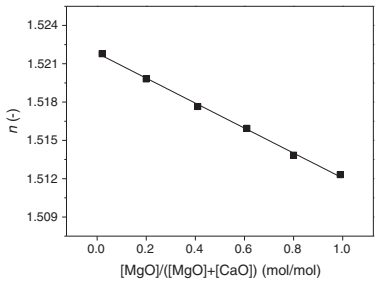

Fig. 7. Refractive index (n) measured at 589.3 nm as a function of the molar ratio [MgO] / ([MgO] + [CaO]). The solid line is a linear fit to data with $R^2 = 0.998$. The standard deviation of n is around ±0.0003.

these peaks are caused by silicon–oxygen–silicon bending vibrations of threefold and fourfold silica ring structures embedded in the glass network. The position of the high-wavenumber band, ~1000 cm^{-1}, varies as magnesium is exchanged with calcium (Fig. 12). According to McMillan [72], this peak is associated with silicon–oxygen stretching vibrations of tetrahedral silicate units. The dashed line in Fig. 12 represents a linear relation between the end-member compositions. We find that the peak position diverges positively from a linear tendency, with the largest deviation found at [MgO] / ([MgO] + [CaO]) = 0.63.

MAS NMR spectra of ^{27}Al in representative sodium aluminosilicate glasses under study are shown in Fig. 13. The spectra all exhibit a narrow asymmetric peak centered around + 50 ppm, consistent with tetrahedral aluminum groups (Al^{IV}) [73]. The aluminum speciation of these glasses is thus very similar to each other, since both position and shape of the ^{27}Al resonance exhibit only minor composition dependence. Only the spectrum of the magnesium end-member composition is slightly broader and more asymmetric on the more shielded side (lower shift). This is due to the presence of higher Al coordination in this sample, such as five-fold coordinated aluminum (Al^{V}).

4. Discussion

4.1. Effect of alkaline earth field strength

In this section, we discuss the effects of completely substituting magnesium for calcium on selected physical properties, i.e., we focus on the difference between the two single alkaline earth-containing end-member compositions.

The high wavenumber vibrational modes of Raman spectroscopy could be associated with higher network connectivity because more energy is required to induce atomic vibrations (shifts in the Q^n-value of the tetrahedral SiO_4 units). Since the oxygen coordination number of Mg^{2+} is probably lower than that of Ca^{2+} [74–76], the number of affected oxygen ions in the SiO_4 network decreases when substituting Mg^{2+} for Ca^{2+}. This explains why the concentration of T – O – T bonds (T = tetrahedral unit) increases as magnesium is substituted for calcium (Fig. 12). It is also well established that tetrahedrally coordinated Mg^{2+} can act as a network former, contributing to an increased population of T – O – T bonding at higher magnesium contents [77].

The magnesium-containing glass has lower density and smaller molar volume compared to the calcium-containing glass (Fig. 6). This difference in molar volume reflects a modification of the glass network structure. The smaller molar volume is caused by tighter binding of oxygen to magnesium, as expected from the larger field strength and smaller size of magnesium compared to calcium [12,78]. It should be noted that a smaller molar volume does not correspond to a denser structure. In contrast, the structure becomes less dense indicated by a decrease in the refractive index when substituting calcium for magnesium (Fig. 7). Hence, although Mg^{2+} has shorter and stronger cation–oxygen bonds, the overall atomic densities of these glasses are lower than that of the ones containing Ca^{2+}.

Vickers hardness is a measure of the resistance towards mechanical deformation of the glass and is phenomenologically related to

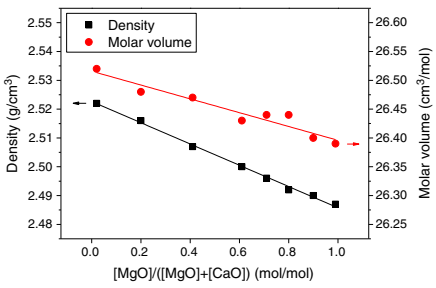

Fig. 6. Density and molar volume as a function of the molar ratio [MgO] / ([MgO] + [CaO]). The solid lines are linear fits to data with R^2 equal to 0.996 and 0.912 for density and molar volume, respectively. Uncertainties in both values are smaller than the symbol sizes.

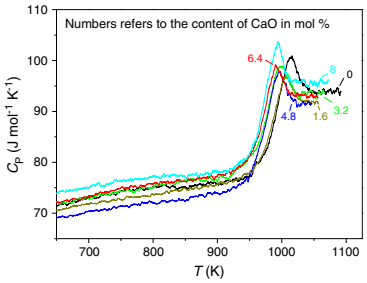

Fig. 8. Heat capacity as a function of temperature for the six samples with different CaO contents (in mol%) as indicated in the figure. The composition of each sample is given in Table 1. The heat capacities are determined by differential scanning calorimetry at a heating rate of 10 K/min subsequent to a cooling of 10 K/min.

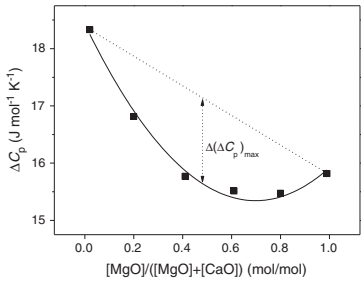

Fig. 9. ΔC_p as a function of the molar ratio of [MgO] / ([MgO] + [CaO]). ΔC_p is the jump in heat capacity occurring at the glass transition and it is calculated as the heat capacity at the glass transition offset (C_{pl}) minus the heat capacity at the glass transition (C_{pg}). An illustration of how to determine these characteristic heat capacities is shown in the inset of Fig. 10. The uncertainty of this method is around ± 0.3 J mol^{-1} K^{-1}. The solid line represents the apparent relation between ΔC_p and the molar ratio of [MgO] / ([MgO] + [CaO]), whereas the dashed line represents a linear extrapolation between the end-member compositions. Both lines are guides for the eye. $\Delta(\Delta C_p)_{max}$ is equal to the maximum discrepancy in ΔC_p between the linear relation and the apparent relation, i.e., the largest mixed alkaline earth effect.

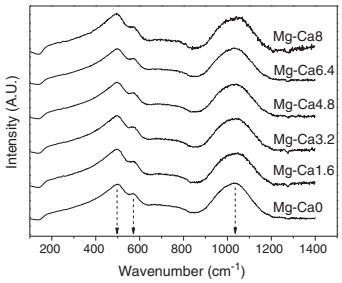

Fig. 11. Raman spectra for the sodium aluminosilicate glasses. The spectra are shifted vertically for clarity. The composition of each sample is tabulated in Table 1, with the designation written on the right corresponding to a specific composition. The arrows indicate the approximate peak positions.

three different deformation mechanisms: densification, elastic deformation, and plastic flow [79]. The elastic moduli of the measured glasses show no compositional dependence (Fig. 5), so according to Yamane and Mackenzie [70] the elastic resistance in these systems should be compositionally invariant. This is in good agreement with the fact that the two end-member compositions exhibit identical hardness. Furthermore, it is expected that the magnesium composition is *less* susceptible to densification based on its lower molar volume [70,80]. However, the magnesium composition has a lower refractive index compared to the calcium composition, indicating that the former composition is *more* susceptible to densification [81]. Both density and refractive index only show minor composition variation ($\pm$1–2%). Thus, it is likely that densification is also compositionally independent within the studied composition range. Plastic flow has earlier been argued to take place above a certain concentration of network modifiers [82]. As both end-member compositions contain the same amount of alkali and alkaline earth oxides, the plastic flow should be identical, and hence, both have similar Vickers hardness (Fig. 4).

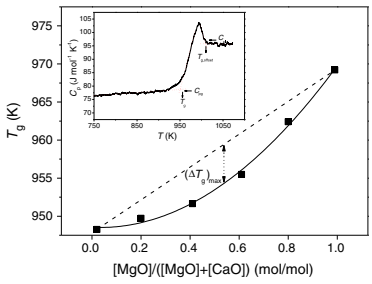

Fig. 10. The glass transition temperature from differential scanning calorimetry as a function of the molar ratio of [MgO] / ([MgO] + [CaO]). The solid line represents the apparent relation between T_g and the molar ratio of [MgO] / ([MgO] + [CaO]), whereas the dashed line is a linear relation; both are guides for the eye. $(\Delta T_g)_{max}$ is marked on the figure where the largest discrepancy exists between linear relation and apparent relation, i.e., the largest mixed alkaline earth effect. Inset: Method for determining T_g and characteristic heat capacities from the heat capacity curves measured by differential scanning calorimetry [53]. The uncertainty of this method is $\pm$2–3 K [88].

The liquid fragility is closely related to the microstructure of glasses and liquids. Usually for oxide compositions, at temperatures above T_g, *strong* liquids contain a high degree of connectivity and *fragile* ones a comparably low degree of connectivity [63]. More precisely, strong liquids have a medium-range structure which is more stable towards temperature fluctuation around T_g. As shown in Figs. 1 and 9, kinetic and thermodynamic fragilities both exhibit the same composition dependence, viz., a decrease in fragility as magnesium is substituted for calcium. As discussed above, the higher field strength of magnesium increases the amount of rigid constraints at T_g and hence, results in lower fragility indices. This is supported by the Raman spectroscopic data, which imply stronger bonding in the magnesium end-member composition.

The higher field strength of magnesium is correlated with a deeper potential energy well, resulting in a decrease of the magnitude of the anharmonic vibrations at a given temperature, and thus, also a decrease of the coefficient of thermal expansion [48]. This agrees with the findings reported in Fig. 2, where α is found to decrease when substituting magnesium for calcium. It is generally accepted that T_g is mainly determined by both the connectivity of the network and its average bond strength. This is supported by accurate quantitative T_g predictions using temperature-dependent constraint theory [83,84]. In our case, the fragility, α, and Raman spectroscopic data suggest a stronger network, i.e., more rigid constraints, in the Mg^{2+} containing compositions. Hence, the higher bond strength between magnesium and oxygen is

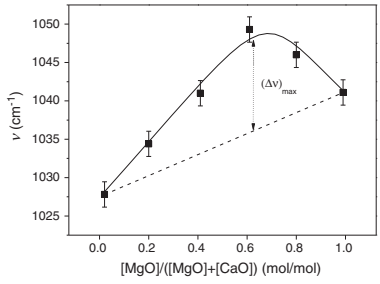

Fig. 12. Peak position wavenumber (ν) of the Raman peak near 1050 cm^{-1} as a function of the molar ratio [MgO] / ([MgO] + [CaO]). The solid line represents the apparent relation between ν and the molar ratio of [MgO] / ([MgO] + [CaO]), whereas the dashed line represents a linear relation between the end-member compositions. Both lines are guides for the eye. $(\Delta\nu)_{max}$ is equal to the maximum discrepancy in ν between the linear relation and the apparent relation, i.e., the largest mixed alkaline earth effect.

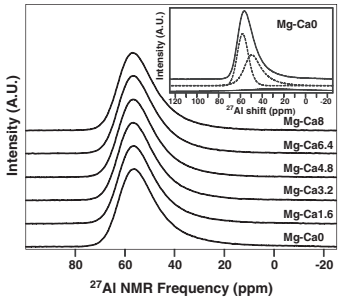

Fig. 13. ^{27}Al MAS NMR spectra for the six selected glasses. The spectra show unchanging lineshape for all glasses expect the magnesium end-member composition, which is slightly broader on the more shielded side. The inset shows an example of deconvoluting these data into Al^{IV} (dashed lines) and Al^{V} peaks (filled area), allowing for an estimation of changes in Al coordination [85]. Multiple Al^{IV} resonances were required to account for the complex lineshape and are consistent with literature values for isotropic chemical shift and quadrupolar coupling product in sodium aluminosilicate and alkaline earth aluminosilicate glasses. The fitting parameters for the Al^{V} resonance match those used in Ref. [85].

overcompensating the smaller coordination number [12], resulting in a higher T_g (Fig. 10). In other words, compared to calcium, magnesium has more rigid constraints at the temperatures of measurement (sub-T_g). The explanation is that some magnesium constraints have a higher onset temperature than those of calcium, which results in more rigid constraints at sub-T_g temperatures, even though the coordination number of magnesium is lower than that of calcium. The same phenomenon is responsible for the increase in isokom temperatures (Fig. 3), because an increase in isokom temperature corresponds to an increase in viscosity (for a constant temperature below T_g). This observation is in agreement with the overall trends of the Raman spectroscopic data, fragility and glass transition temperature data, all suggesting stronger oxygen bonding, more rigid constraints, and more tetrahedral bonding in the magnesium-containing compositions. From the NMR data (Fig. 13), we conclude that AlO_4 tetrahedra in the Ca-containing glasses are essentially all charge-balanced by a combination of Na^+ and Ca^{2+}. These spectra can be satisfactorily simulated without the need for an Al^{V} resonance. However, in the one instance where Ca is only present at trace levels, the need for alkaline earth cations (Mg^{2+}) to complement the role of Na^+ is partially ineffective, leading to a small population of Al^{V} species. In detail we find approximately 5% Al^{V} in the Mg–Ca0 composition compared to 0% in the remaining compositions (see inset of Fig. 13). Such quantities of Al^{V} species are consistent with high quality fitting of ^{27}Al MAS NMR spectra in similar systems [58,85]. Changes in aluminum speciation in the mixed alkaline earth compositions are thus negligible, even though we measure a slight increase of the connectivity in the magnesium-containing end-member composition. This slight increase in Al^{V} of the magnesium-containing composition contributes to the general trend, being that the magnesium-containing composition compared to the calcium-containing one has higher T_g, isokom temperatures and fragility, i.e., properties related to the connectivity.

4.2. Mixed alkaline earth effect

The mixed alkaline earth effect is observed as a deviation from linear composition dependence. For the current glasses under investigation, we find the effect manifested in the Raman spectroscopic data (Fig. 12) as a maximum and in the Vickers hardness (Fig. 4), fragility (Figs. 1 and 9), glass transition temperature (Fig. 10) and viscosity data (Fig. 3) as a minimum. According to Fluegel [78], the mixed alkaline earth effect is normally observed as a minimum in viscosity. He observed a gradient in the slope of the viscosity-composition plot, going from a large negative departure at low concentration of modifier to a relatively small slope at high concentration of modifier. Neuville and Richet [49] explain the minima in viscosity by an excess of entropy caused by mixing, however, this behavior is in complete contrast to the theory given by Dietzel [3]. The theory by Dietzel [3] is that oxygen stabilized by two different alkaline earth ions is energetically much more favored than oxygen stabilized by similar alkaline earth ions [50], which should result in *maxima* in Vickers hardness, isokom temperatures and T_g. The observed *minima* in Vickers hardness (Fig. 4), isokom temperatures (Fig. 3), and T_g (Fig. 10) indicate the exact opposite, namely that the mixed magnesium–calcium compositions experience weaker bonding than the end-member compositions.

Above we argued that both densification and elastic deformation are compositionally independent. This suggests that plastic flow accounts for the nonlinear composition dependence of Vickers hardness [6,86]. Faivre et al. [6] reported that the plastic flow of glass is caused by the hopping of network modifiers, promoting slippage of the rigid parts of the network [82,86]. This is, however, not the entire explanation, as we may assume that the plastic flow is generated by a more cooperative rearrangement of atoms. Ionic conductivity measurements reveal a minimum in conductivity as one alkaline earth ion is substituted for another one [1]. Hence, the lowest concentration of mobile ions is at a substitution degree of 0.50 and the plastic flow according to Faivre et al. [6] should therefore have a minimum at this composition. The minimum in ionic conductivity at equal concentrations of alkaline earth ions is also predicted by the dynamic structure model [30,33]. This is, however, not what we observe in Fig. 4, since a *minimum* in ionic conductivity should correspond to a *maximum* in hardness. If we instead consider viscosity to be an estimate of the plastic flow, we suggest that the occurrence of the minimum in hardness is associated with the corresponding minimum in isokom temperatures. Although the deformation under indentation and the viscous flow under shear occur at various temperature regions, their mechanisms are similar to large extents, i.e., both are related to the translational motion of structural units. It can be argued that the responsible underlying topological constraints of the mechanisms may differ, due to the temperature dependence of these constraints. If this is the case, an offset might occur between the minima in Vickers microhardness and isokom temperatures at room-temperature [87].

Based on the Raman spectroscopic data, we find a relatively high concentration of T–O–T bonds in the mixed alkaline earth region (Fig. 12). This might be associated with the observed negative deviation from linearity for the liquid fragility index, since higher network connectivity generally corresponds to a *stronger* liquid. However, the low-temperature viscosity of the mixed alkaline earth compositions is lower than that of the end-member compositions (Fig. 3). The Raman spectroscopic data suggest that the network connectivity of the mixed Ca–Mg compositions is higher than that of the two end-members, which normally increases viscosity. Therefore we can infer that the decrease of viscosity observed in this work is not related to the network connectivity, but instead is mainly related to the local structural environment around the network modifiers causing overall bond weakening.

5. Conclusion

We have studied the mixed alkaline earth effect in a series of MgO/CaO sodium aluminosilicate glasses by substituting MgO for CaO. We find that the mixed alkaline earth effect manifests itself as a maximum in T–O–T bonds, but a minimum in Vickers microhardness, glass transition temperature, and isokom temperatures. We explain the minimum in viscosity by a bond weakening in the local structural environment around the network modifiers, viz., the minimum originates from the structural character of the modifying ions.

The viscous flow under shear and deformation under indentation are both related to the translational motion of structural units, and

since the elastic moduli in the investigated system are compositionally independent, we suggest that the observed minimum in microhardness is associated with the corresponding minimum in shear viscosity.

Acknowledgments

We thank the Characterization and Materials Processing Directorate at Corning Incorporated for the help with glass preparation and characterization, respectively. L. Huang acknowledges the support from the NSF under grant DMR-1105238.

References

[1] Y. Gao, C. Cramer, Solid State Ionics 176 (2005) 921.
[2] A. Mohajerani, J.W. Zwanziger, J. Non-Cryst. Solids 358 (2012) 1474.
[3] A.H. Dietzel, Phys. Chem. Glasses 24 (1983) 172.
[4] D.E. Day, J. Non-Cryst. Solids 21 (1976) 343.
[5] R.J. Hand, D.R. Tadjiev, J. Non-Cryst. Solids 356 (2010) 2417.
[6] A. Faivre, F. Despetis, F. Guilaume, P. Solignac, J. Am. Ceram. Soc. 93 (2010) 2986.
[7] G. Gehlhoff, M. Thomas, Z. Tech. Phys. (1926) 105.
[8] J.E. Shelby, D.E. Day, J. Am. Ceram. Soc. 53 (1970) 182.
[9] H.W. Guo, X.F. Wang, Y.X. Gong, D.N. Gao, J. Non-Cryst. Solids 356 (2010) 2109.
[10] J.O. Isard, J. Non-Cryst. Solids 1 (1969) 235.
[11] Y. Hasegawa, Glastech. Ber. 57 (1984) 177.
[12] K. Hirao, M. Yoshimoto, N. Soga, K. Tanaka, J. Non-Cryst. Solids 130 (1991) 78.
[13] K.-D. Kim, Glastech. Ber. Glass. Sci. Technol. 72 (1999) 393.
[14] M. Solvang, Y.Z. Yue, S.L. Jensen, J. Non-Cryst. Solids 345 & 346 (2004) 782.
[15] M.L.F. Nascimento, E. Nascimento, S. Watanabe, Mater. Chem. Phys. 96 (2006) 55.
[16] B. Roling, M.D. Ingram, J. Non-Cryst. Solids 265 (2000) 113.
[17] M.L.F. Nascimento, S. Watanabe, Mater. Chem. Phys. 105 (2007) 308.
[18] M.D. Ingram, A.H.J. Robertson, Solid State Ionics 94 (1997) 49.
[19] M.D. Ingram, C.T. Moynihan, A.V. Lesikar, J. Non-Cryst. Solids 38 & 39 (1980) 371.
[20] D. Wolf, J. Phys. Chem. Solids 40 (1979) 757.
[21] J.N. Mundy, Solid State Ionics 28–30 (1988) 671.
[22] D. Ravaine, J. Non-Cryst. Solids 73 (1985) 287.
[23] J.A. Bruce, M.D. Ingram, M.A. MacKenzie, Solid State Ionics 18 & 19 (1986) 410.
[24] S.R. Elliott, Solid State Ionics 27 (1988) 131.
[25] S.R. Elliott, Mater. Sci. Eng. B3 (1989) 69.
[26] K. Funke, Prog. Solid State Chem. 22 (1993) 111.
[27] A. Bunde, M.D. Ingram, P. Mass, J. Non-Cryst. Solids 172–174 (1994) 1222.
[28] M.D. Ingram, Physica A266 (1999) 390.
[29] S. Balasubramanian, K.J. Rao, J. Phys. Chem. 97 (1993) 8835.
[30] A. Bunde, M.D. Ingram, P. Maass, K.L. Ngai, J. Non-Cryst. Solids 131–133 (1991) 1109.
[31] J. Dyre, P. Maass, B. Roling, D.L. Sidebutton, Rep. Prog. Phys. 72 (2009) 1.
[32] K.J. Rao, S. Kumar, Curr. Sci. 86 (2003) 945.
[33] P. Maass, R. Peibst, J. Non-Cryst. Solids 352 (2006) 5178.
[34] G.N. Greaves, K.L. Ngai, Phys. Rev. B52 (1995) 6358.
[35] S.N. Houde-Walter, J.M. Inman, A.J. Dent, G.N. Greaves, J. Phys. Chem. 97 (1993) 9330.
[36] B. Gee, M. Janssen, H. Eckert, J. Non-Cryst. Solids 215 (1997) 41.
[37] J.F. Stebbins, Solid State Ionics 112 (1998) 137.
[38] E.I. Kamitsos, A.P. Patsis, G.D. Chryssikos, J. Non-Cryst. Solids 152 (1993) 246.
[39] E.I. Kamitsos, Y.D. Yiannopoulos, H. Jain, W.C. Huang, Phys. Rev. B54 (1996) 9775.
[40] J. Swenson, A. Matic, C. Karlsson, L. Börjesson, C. Meneghini, W.S. Howells, Phys. Rev. B63 (2001) 132202.
[41] H. Lammert, A. Heuer, Phys. Rev. B72 (2005) 214202.
[42] J. Habasaki, I. Okada, Y. Hiwatari, J. Non-Cryst. Solids 183 (1995) 12.
[43] A.K. Varshneya, Int. J. Appl. Glass Sci. 1 (2010) 131.
[44] G. Mingin, Z. Zhang, L. Ly, W. Xingen, Y. Ruifang, XIV Int. Cong. Glass, 357, 1986.
[45] J. Briggs, Glass Ceram. Bull. 22 (1975) 73.
[46] M.M. Smedskjaer, L. Huang, G. Scannell, J.C. Mauro, Phys. Rev. B85 (2012) 144203.
[47] S. Yoshida, J.-C. Sanglebæuf, T. Rouxel, J. Mater. Res. 20 (2005) 3404.
[48] J.-O. Byun, B.-H. Kim, K.-S. Hong, H.-J. Jung, S.-W. Lee, A.A. Izyneev, J. Non-Cryst. Solids 190 (1995) 288.
[49] D.R. Neuville, P. Richet, Geochim. Cosmochim. Acta 55 (1991) 1011.
[50] Y. Hasegawa, Glastech. Ber. 53 (1980) 277.
[51] R. Waesche, R. Brückner, J. Non-Cryst. Solids 107 (1989) 309.
[52] B.Z. Pevzner, V.P. Klyuev, Glass Phys. Chem. 30 (2004) 506.
[53] Y.Z. Yue, J.deC. Christiansen, S.L. Jensen, Phys. Chem. Lett. 357 (2002) 20.
[54] M. Guerette, L. Huang, J. Phys. D: Appl. Phys. 45 (2012) 275302.
[55] V.P. Zakaznova-Herzog, W.J. Malfait, F. Herzog, W.E. Halter, J. Non-Cryst. Solids 353 (2007) 4015.
[56] W.J. Malfait, W.E. Halter, Phys. Rev. B77 (2008) 014201.
[57] D. Massiot, F. Fayon, M. Capron, I. King, S. Le Calvé, B. Alonso, J.-O. Durand, B. Bujoli, Z. Gan, G. Hoatson, Magn. Reson. Chem. 40 (2002) 70.
[58] D.R. Neuville, L. Cormier, D. Massiot, Geochim. Cosmochim. Acta 68 (2004) 5071.
[59] G. Adam, J. Gibbs, J. Phys. Chem. 43 (1965) 139.
[60] I. Avramov, A. Milchev, J. Non-Cryst. Solids 104 (1988) 253.
[61] J. Mauro, Y.Z. Yue, A.J. Ellison, P.K. Gupta, D.C. Allan, Proc. Natl. Acad. Sci. U. S. A. 106 (2009) 19780.
[62] G.W. Scherer, J. Am. Ceram. Soc. 75 (1992) 1060.
[63] C.A. Angell, Science 267 (1995) 1924.
[64] D.W. Marquardt, J. Soc. Indust. Appl. Math. 11 (1963) 431.
[65] K. Levenberg, Quart. Appl. Math. 2 (1944) 164.
[66] R. Roeskiy, J.R. Varner, J. Am. Ceram. Soc. 74 (1991) 1129.
[67] H. Li, R.C. Bradt, J. Non-Cryst. Solids 146 (1992) 197.
[68] T. Kavetskyy, J. Borc, K. Sangwal, V. Tsmots, J. Optoelectron. Adv. Mater. 12 (2010) 2082.
[69] J.-M. Schneider, M. Bigerelle, A. Iost, Mater. Sci. Eng. A262 (1999) 256.
[70] M. Yamane, J.D. Mackenzie, J. Non-Cryst. Solids 15 (1974) 153.
[71] F.L. Galeener, J. Non-Cryst. Solids 49 (1982) 53.
[72] P. McMillan, Am. Mineral. 69 (1984) 622.
[73] S.H. Risbud, R.J. Kirkpatrick, A.P. Taglialavore, B. Montez, J. Am. Ceram. Soc. 70 (1987) C10.
[74] A.K. Katz, J.P. Glusker, S.A. Beebe, C.W. Bock, J. Am. Chem. Soc. 118 (1996) 5752.
[75] B.N. Nelson, G. Exarhos, J. Chem. Phys. 71 (1979) 2739.
[76] K. Shimoda, T. Nemoto, K. Saito, J. Phys. Chem. B112 (2008) 6747.
[77] S. Sen, H. Maekawa, G.N. Papatheodorou, J. Phys. Chem. B113 (2009) 15243.
[78] A. Fluegel, Eur. J. Glass Sci. Technol. A48 (2007) 13.
[79] J.A. Howell, J.R. Hellmann, C.L. Muhlstein, Mater. Lett. 62 (2008) 2140.
[80] T. Rouxel, T. Hammouda, A. Moréac, Phys. Rev. Lett. 100 (2008) 225501.
[81] T. Rouxel, H. Ji, J.P. Guin, F. Augereau, B. Rufflé, J. Appl. Phys. 107 (2010) 094903.
[82] K.W. Peter, J. Non-Cryst. Solids 5 (1970) 103.
[83] J.C. Mauro, P.K. Gupta, R.J. Loucks, J. Chem. Phys. 130 (2009) 234503.
[84] P.K. Gupta, J.C. Mauro, J. Chem. Phys. 130 (2009) 094503.
[85] D.R. Neuville, L. Cormier, V. Montouillout, P. Florian, F. Millot, J.-C. Rifflet, D. Massiot, Am. Mineral. 93 (2008) 1721.
[86] A. Mohajerani, J.W. Zwanziger, J. Non-Cryst. Solids 358 (2012) 1474.
[87] M.M. Smedskjaer, J.C. Mauro, Y.Z. Yue, Phys. Rev. Lett. 105 (2010) 115503.
[88] Q. Zheng, M. Potuzak, J.C. Mauro, M.M. Smedskjaer, R.E. Youngman, Y.Z. Yue, J. Non-Cryst. Solids 358 (2012) 993.

Paper V

JOURNAL OF APPLIED PHYSICS **117**, 034903 (2015)

Role of elastic deformation in determining the mixed alkaline earth effect of hardness in silicate glasses

Jonas Kjeldsen,[1] Morten M. Smedskjaer,[1] Marcel Potuzak,[2] and Yuanzheng Yue[1,a)]
[1]*Section of Chemistry, Aalborg University, DK-9000 Aalborg, Denmark*
[2]*Science and Technology Division, Corning Incorporated, Corning, New York 14831, USA*

(Received 3 October 2014; accepted 6 January 2015; published online 16 January 2015)

Glasses deform permanently as a result of indentation and the total resistance to deformation consists of three individual resistances, i.e., those to elastic deformation, densification, and plastic flow. The link between Vickers hardness and the resistances to densification and plastic flow has been investigated previously, but the link between the resistance to elastic deformation and hardness has not yet been studied. In this work, we investigate the link between elastic deformation during indentation and Vickers hardness in a series of mixed magnesium-barium boroaluminosilicate glasses. We show that the mixed alkaline earth effect manifests itself as deviations from linearity in shear modulus, Poisson's ratio, glass transition temperature, liquid fragility index, hardness, volume of densification, and volume of plastic flow. We find no correlation between the elastic part of the indentation and hardness, and we thus infer that elastic deformation does not play a dominant role in determining the mixed alkaline earth effect of hardness. However, interestingly, we find a strong correlation between Poisson's ratio, volume of plastic flow, and hardness, by which the minimum in hardness could be explained in terms of a minimum in shear viscosity. © *2015 AIP Publishing LLC*. [http://dx.doi.org/10.1063/1.4906099]

INTRODUCTION

The study of indentation deformation processes in glass was initiated in 1962, at which time it was proposed that these processes obey the classical law of plasticity, i.e., indentation was perceived as a purely plastic process.[1–4] Later, via comparison between the indent volume and the volume of pile-up, it was shown that indentation deformation originates from both plastic flow and densification.[5–7] It is now widely accepted that intrinsically glass is a brittle material that deforms both by plastic flow and by densification when pressure is applied.[1] As hardness is a measure of the ability for a material to resist elastoplastic deformation, it is one of the most important mechanical properties of glass for applications such as scratch-resistant covers for personal electronic devices.[8]

According to Yamane and Mackenzie,[9] the resistance of a glass to deformation is a result of the resistance to three distinct deformation processes: plastic flow, densification, and elastic deformation. Plastic flow is a volume conservative displacement of matter, where material is forced upwards creating a positive flux, which in turn results in pile-ups around the indent. Densification is a non-volume conservative irreversible compression that creates a hemispherical area of increased density beneath the indent. Elastic deformation is a reversible compression that recovers after unloading. Recently, Yoshida *et al.*[10] have developed a method that is capable of quantifying the amount of nonplasticity in glass. One of the key steps for the method is to perform sub-T_g annealing to enable quantification of densification and plastic flow. The resistance to the elastic part of the deformation process is, however, not accessed in their approach.[10–12] Under an applied pressure, the atomic bonds in the glass stretch and bend away from their favorable position, allowing for some elastic deformation. Upon unloading, the bonds return to the state of lowest energy and the material recovers to its original shape. In other words, part of external mechanical energy (given by indentation) causes elastic work in the glass, which in turn leads to an increase of the potential energy of the atoms. When unloading, this increased potential energy is released, resulting in an expansion work. The rest of the mechanical energy causes plastic flow (i.e., a sort of deformation work), permanent densification (a permanent high potential state) and a small amount of dissipation heat. Thus, the energy conservation law is obeyed. As hardness is calculated as the applied force divided by the indent size, part of which is used for the elastic deformation, the latter contributes to the glass hardness.[9,10] Kjeldsen *et al.*[4,13] have proposed a new approach to predict the compositional scaling behavior of hardness in mixed modifier silicate glasses. In this approach, the compositional dependence of hardness is assumed to be a consequence of the resistance of the glass network to plastic flow. The investigated mixed modifier glass systems were designed to achieve constant elastic moduli with respect to composition, i.e., the influence of the elastic deformation on hardness was kept constant.

The resistance of a glass to permanent deformation (i.e., hardness) is typically dominated by one of the three deformation process. Kjeldsen *et al.*[4,13] have found that in mixed modifier glasses, the resistance to plastic flow is the dominant resistance to deformation.[4] However, in glass systems of high silica content (>85 mol. % SiO_2), densification has been reported to be the dominant deformation process.[4–6,10–14] In certain glass systems indented under low loads, elastic

a)Author to whom correspondence should be addressed. Electronic mail: yy@bio.aau.dk. Tel.: +45 9940 8522.

deformation could be the dominant deformation process. In order to enable prediction of the compositional dependence of hardness, it is important to account for all three deformation mechanisms. Makishima and Mackenzie considered the glass hardness to be closely related to the Young's modulus (E).[15] E is a measure of a material's resistance to axial stress under circumstances where plastic flow is prohibited. Thus, the atomic movement in glass during axial deformation should be similar to that during elastic deformation during indentation, i.e., E correlates well with the elastic part of indentation, and hence, with hardness under certain circumstances. Recently, Hand and Tadjiev[16] proposed a direct one-to-one relation between E and H_v and found that increasing hardness is usually correlated with increasing modulus. While this correlation applies to many compositions,[16] it does not apply to all.[4,13] Therefore, the intrinsic link between E and H_v still needs to be explored. To the best of our knowledge, the relation between the elastic part of indentation and hardness has not yet been studied.

In this paper, we investigate the correlation between Vickers hardness (H_v) and the deformation processes under indentation in a series of mixed magnesium-barium boroaluminosilicate glasses. In our recent investigations on the relation between deformation processes under indentation and H_v, we kept E constant and thus neglected its influence on H_v.[4,13] Here, we choose a series of boroaluminosilicate glasses with varying MgO/BaO molar ratios as the objects of this study since they are expected to exhibit a relatively large change in E upon Mg-for-Ba substitution.[17] The contributions of densification and plastic flow to indentation are determined using atomic force microscopy (AFM), applying the method developed by Yoshida *et al.*[10] The composition dependences of density (ρ), shear modulus (G), glass transition temperature (T_g), and liquid fragility index (m) are also determined, which are useful for interpreting the AFM results. Finally, we discuss the correlations among the deformation processes under indentation, Young's modulus, and hardness.

EXPERIMENTAL

Sample preparation

The nominal compositions of the studied mixed magnesium-barium boroaluminosilicate glasses are $64SiO_2$-$12Al_2O_3$-$6B_2O_3$-$12Na_2O$-$(6–x)MgO$-$xBaO$, where $x = 0$, 1.5, 3, 4.5, and 6. The end-member glasses, i.e., $x = 0$ and 6, were previously studied in Refs. 18–20 with respect to their mechanical, thermophysical, and optical properties. All glasses included ~0.16 mol. % SnO_2 as a fining agent. To prepare the glasses, the raw materials were first melted in a covered platinum crucible for 5 h in air at a temperature between 1450 and 1600 °C, depending on composition. The melts were first quenched in water, and the resulting glass pieces were crushed and remelted for 6 h at 1650 °C and finally cast onto a stainless steel plate in air. The remelting was performed to ensure quality and homogeneity of the final glass product. The glasses were annealed for 2 h at their respective annealing points ($\eta = 10^{12.3}$ Pa s). The chemical compositions of the final glasses were determined using X-ray fluorescence, and the analyzed compositions were all within 0.5 mol. % of the nominal targets (see Table I). Room-temperature densities of the glasses were determined by Archimedes' principle using water as immersion liquid.

Viscosity

The temperature dependence of equilibrium viscosity was measured by performing beam bending, parallel plate, and concentric cylinder experiments. The viscosity curve of each composition is represented by data points at $10^{6.6}$ Pa s (obtained via parallel plate viscometry), 10^{11} Pa s (obtained via beam bending viscometry), and 12–20 data points in the range of 10^1 to 10^6 Pa s (obtained via the concentric cylinder method). For beam bending experiments, bars of 55 mm length and 2.5×2.5 mm^2 cross section were cut from the bulk glasses. For parallel plate experiments, cylinders of 6.0 mm diameter and 5.0 mm thickness were core drilled, and afterwards, the flats were polished to an optical finish. For concentric cylinder experiments, ~600 g of crushed glass was remelted. The temperature errors associated with determining the 10^{11} Pa s point by the beam-bending method and the $10^{6.6}$ Pa s point by the parallel plate method are ±1 and ±2 °C, respectively. The estimated error in viscosity for the high-temperature measurements (by the concentric cylinder method) is $\log(\eta) = \pm 0.02$ (η in Pa s).

Indentation and AFM

All of the prepared glass samples were polished to mirror image finish and H_v was measured using a Duramin 5 indenter (Struers A/S). A total of 30 indents were conducted on each sample using an indentation time of 10 s and an indentation load of 0.49 N. The measurements were performed in air at room temperature. The indentation impressions were observed using a Ntegra (NT-MDT) AFM. Measurements of deformation volumes were performed in tapping mode at 50% relative humidity and room temperature. The AFM cantilever had a silicon tip, the scanning frequency was 0.47 Hz, and the scan size was $20 \times 20\ \mu m^2$. Following the procedure of Yoshida *et al.*,[10] at least ten indentations were examined before and after annealing for 2 h at 0.9 times the glass transition temperature (in K) of the respective composition.

TABLE I. Chemical compositions of the 5 magnesium-barium boroaluminosilicate glasses under study, which were analyzed using X-ray fluorescence (±0.1 mol. %).

	Composition (mol. %)						
Glass ID	SiO_2	Al_2O_3	B_2O_3	Na_2O	MgO	BaO	SnO_2
Mg-Ba0	64.03	11.80	5.99	11.92	5.89	…	0.15
Mg-Ba1.5	64.03	11.91	6.04	11.77	4.53	1.50	0.15
Mg-Ba3	64.02	11.93	6.01	11.87	2.98	2.98	0.15
Mg-Ba4.5	64.06	11.96	5.96	11.83	1.52	4.46	0.15
Mg-Ba6	63.87	11.94	5.92	11.96	0.03	6.09	0.16

Elastic moduli

The elastic properties (E and G) were measured at room temperature using resonant ultrasound spectroscopy. Prisms of dimensions 10 mm × 8 mm × 6 mm were used to gather resonance spectra from 100 to 300 kHz. For each sample, the first five resonant peaks as a function of frequency resulting from excited resonant eigenmodes were used to calculate the elastic properties.

Calorimetry

Calorimetric measurements were performed on a differential scanning calorimeter (DSC 449C, Netzsch) to determine the calorimetric T_g. Each sample was subjected to two up and downscans at 10 K/min to a maximum temperature of ~100 K above the glass transition temperature. The first scan reflects an unknown thermal history, whereas the second scan reflects the standard thermal history of a cooling of 10 K/min.[21] A flow of 40 ml/min argon was used as protective gas, and platinum crucibles were used for both sample and reference. In order to calculate the isobaric heat capacity (C_p) of the aluminosilicate glasses, a sapphire standard of approximately the same weight was measured before the measurement of each sample.

RESULTS

The composition dependence of the elastic moduli (E and G) is plotted in Fig. 1 for the mixed Mg-Ba boroaluminosilicate glass series with various molar ratios of [MgO]/([MgO] + [BaO]) (hereafter, this molar ratio is denominated by the symbol f). It is seen that E decreases linearly with f, whereas G decreases in a nonlinear fashion with the largest deviation from linearity at $f = 0.5$. That is, the mixed alkaline earth effect is observed in G, but not in E (Fig. 1). The nonlinear trend for G and the negative linear trend for E have not been reported in earlier studies.[4,13] Using these trends, we can qualitatively explain the changing trend of the elastic part of deformation under indentation with varying f. From the values of E and G, the Poisson's ratio (ν) can be calculated as $\nu = 2E/G - 1$.[9] In Fig. 2, ν is plotted as a function of f. It is seen that ν initially increases with f and then decreases when $f > 0.5$, i.e., the largest deviation from linearity is found at $f = 0.5$.

Fig. 3 shows the composition dependence of H_v, which manifests an initial increase followed by a decrease with f, i.e., the mixed alkaline earth effect of hardness occurs. The largest negative deviation from linearity and the minimum value of H_v are observed at around $f = 0.5$. Examples of the indents are shown in Fig. 4. As mentioned in the introduction, the resistance of a glass to deformation during Vickers indentation is a result of three distinct processes, namely, plastic flow, densification, and elastic deformation.[9] AFM measurements are therefore performed to determine the size of the indents and the amount of pile-up both before and after sub-T_g annealing. From these results, the volume of densification (V_d) and volume of plastic flow (V_p) are calculated as per Eqs. (1) and (2):[10]

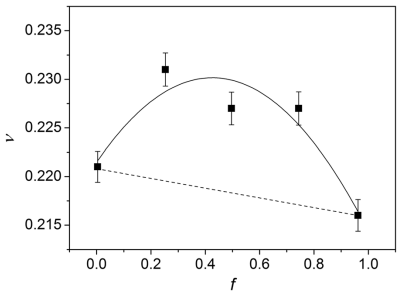

FIG. 2. Poisson's ratio (ν) as a function of the molar ratio of f = [MgO]/([MgO] + [BaO]). ν is calculated as $2E/G - 1$.[9] The solid line represents the compositional scaling of ν, whereas the dashed line depicts a linear relation between the two end-member compositions. Both lines are guides for the eye.

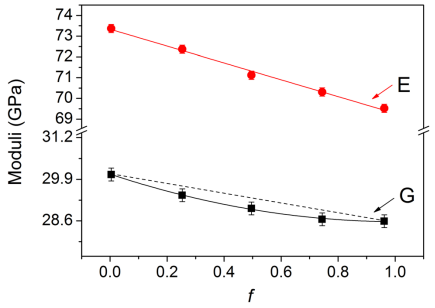

FIG. 1. Shear modulus (G) and Young's modulus (E) as a function of the molar ratio (f) of magnesium to total alkaline earth content, i.e., [MgO]/([MgO] + [BaO]). The solid lines represent the compositional scaling of E and G, whereas the dashed lines depict a linear relation between the two end-member compositions. Both lines are guides for the eye.

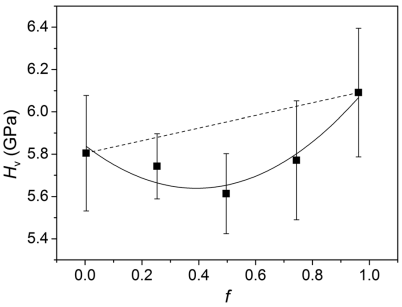

FIG. 3. Vickers hardness (H_v) as a function of the molar ratio of f = [MgO]/([MgO] + [BaO]). The solid line represents the compositional scaling of H_v, whereas the dashed line depicts a linear relation between the two end-member compositions. Both lines are guides for the eye.

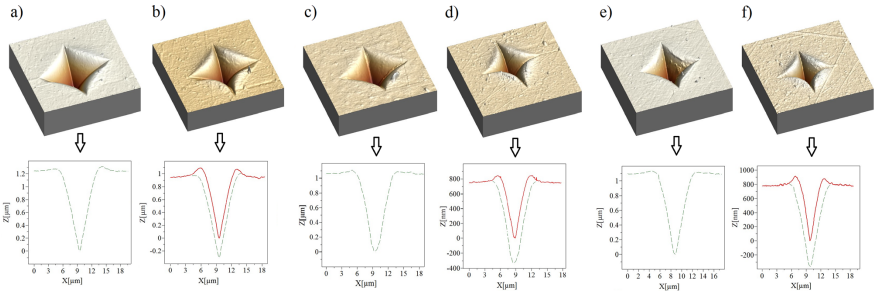

FIG. 4. AFM images of indents and their respective cross-sections. Images (a) and (b) are obtained for the glass with $f=0$ before and after annealing at $0.9\times T_g$ (in K), respectively. Images (c) and (d) are for the glass with $f=0.5$ before and after annealing at $0.9\times T_g$, respectively. Images (e) and (f) are obtained for the glass with $f=1$ before and after annealing at $0.9\times T_g$, respectively. All images have the same scanning area ($20\,\mu m\times 20\,\mu m$), but the height of the images (z) is different and indicated on each cross-sectional image. The dashed lines represent the initial volume (V_i^-), while the solid lines indicate the indent volume after annealing (V_i^+). The volume in between is the volume of densification (V_d).

$$V_d = (V_i^- - V_a^-) + (V_a^+ - V_i^+), \quad (1)$$

$$V_p = V_i^- - ((V_i^- - V_a^-) + (V_a^+ - V_i^+)), \quad (2)$$

where subscripts i and a indicate initial volumes and volumes after annealing, respectively, and superscripts $-$ and $+$ indicate indentation volumes and pile-up volumes, respectively. The derived volumes of densification and plastic flow (V_d and V_p) are plotted in Fig. 5 as a function of f, and their determination is illustrated in Fig. 4. Both V_d and V_p exhibit nonlinear compositional scaling with the largest deviation from linearity at around $f=0.5$. V_p is experiencing a positive deviation, while V_d is experiencing a negative deviation from linearity, but both exhibit the mixed alkaline earth effect. It is notable that V_d is ~4 times larger than V_p.

The Poisson's ratio is a measure of the materials ability to expand in the transverse axes of applied compression, and is consequently closely related to V_d and V_p. A negative correlation has previously been proposed between ν and the ratio of densification to initial indentation volume (this ratio is also referred to as the volume of recovery (V_R)).[10,22] To test this, the volume of recovery is plotted as a function of magnesium to total alkaline earth content in Fig. 6. V_R initially decreases with f, but at around $f=0.5$, the slope changes and V_R increases with further increase in f. The compositional scaling of V_R (Fig. 6) resembles that of $1/\nu$ (Fig. 2).

The composition dependence of liquid fragility index (m) and glass transition temperatures (T_g) both relates to shear motion and thus to plastic flow. To determine the liquid fragility index, m, we use the measured viscosity data in the range of 10^1 to 10^{11} Pa s. Those data are fitted to the equation:[23]

$$\log\eta(T) = \log\eta_\infty + (12-\log\eta_\infty) \times \frac{T_g}{T}\exp\left[\left(\frac{m}{12-\log\eta_\infty}-1\right)\left(\frac{T_g}{T}-1\right)\right], \quad (3)$$

where η_∞ is the high-temperature limit of liquid viscosity. The derived m values are plotted against composition in

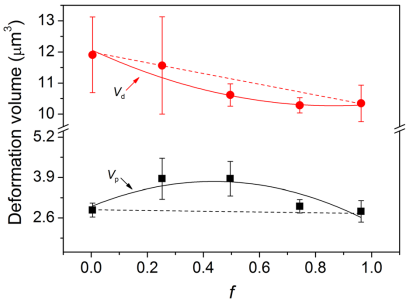

FIG. 5. Volumes of plastic flow (V_p) and densification (V_d) as a function of the molar ratio of $f=$[MgO]/([MgO]+[BaO]). The solid lines represent the compositional scaling of V_p and V_d, whereas the dashed lines depict a linear relation between the two end-member compositions. Both lines are guides for the eye.

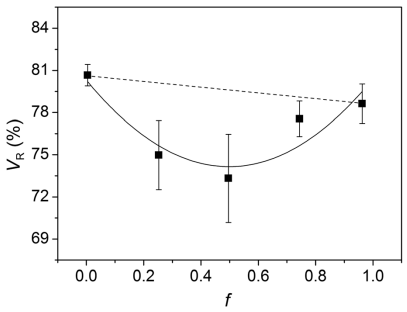

FIG. 6. Volume of recovery (V_R) as a function of the molar ratio of $f=$[MgO]/([MgO]+[BaO]). The solid line represents the compositional scaling of V_R, whereas the dashed line depicts a linear relation between the two end-member compositions. Both lines are guides for the eye.

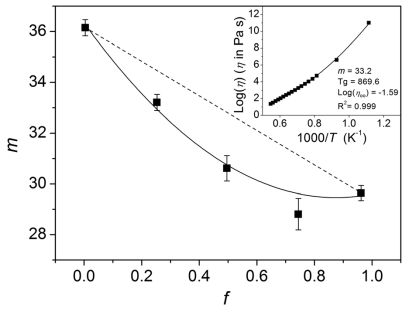

FIG. 7. Liquid fragility indices (m) as a function of the molar ratio of $f = [MgO]/([MgO] + [BaO])$. m values are determined by fitting Eq. (3) to viscosity data. An example of this determination is shown in the inset,[20] where $f = 0.75$ is used as an example. The solid lines represents the compositional scaling of m, whereas the dashed line depicts a linear relation between the two end-member compositions. Both lines are guides for the eye.

Fig. 7. The T_g values determined by DSC are shown in Fig. 8, and experience similar compositional scaling as those obtained from Eq. (3). It is seen in Fig. 7 that m experiences a nonlinear decrease with increasing f, and on Fig. 8 that T_g experiences a nonlinear increase with increasing f. Both T_g and m have the largest deviation from linearity at $f \approx 0.5$.

Fig. 9 shows the compositional scaling of ρ and molar volume (V_0). V_0 is calculated as the molar mass divided by the glass density. ρ is found to linearly decrease with f, whereas V_0 decreases in a nonlinear fashion with the largest deviation from linearity at $f \approx 0.5$.

DISCUSSION

Elastic deformation

Based on the information of the short-range glass structure, such as interatomic bonding energies and network connectivity, it is possible to estimate the composition dependence of

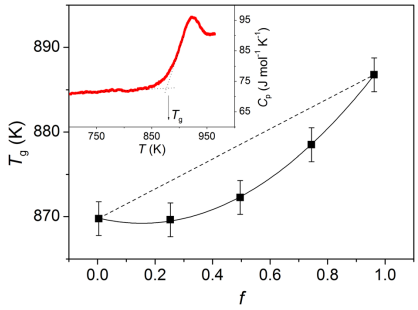

FIG. 8. Glass transition temperatures (T_g) as a function of the molar ratio of $f = [MgO]/([MgO] + [BaO])$. The solid line represents the compositional scaling of T_g, whereas the dashed line depicts a linear relation between the two end-member compositions. Both lines are guides for the eye. Inset: Determination of T_g, using the glass with $f = 0.25$ as an example.[21]

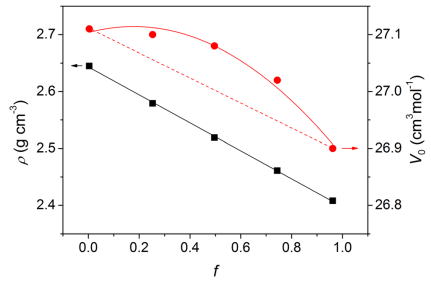

FIG. 9. Density (ρ) and molar volume (V_0) as a function of the molar ratio of $f = [MgO]/([MgO] + [BaO])$. ρ is plotted on the primary ordinate and V_0 on the secondary. The solid lines represent the compositional scaling of ρ and V_0, whereas the dashed line depicts a linear relation between the two end-member compositions. Both lines are guides for the eye.

properties such as E and H_v.[1,11,15,24,25] Therefore, it could be expected that the two properties are linked since they rely on the same set of underlying constraints.[9,15,16] Hand and Tadjiev[16] found a relatively good positive correlation between E and H_v for a wide range of glasses ($R^2 = 0.74$). In this work, E exhibits a linear decrease with increasing f (Fig. 1), whereas H_v exhibits a minimum value at $f = 0.5$ and a general increase from the Mg to Ba end-member compositions (Fig. 3). Thus, for the mixed alkaline earth glasses investigated in this study, there is not a positive correlation between E and H_v. Consequently, if E is considered to represent the resistance to elastic deformation under indentation, elastic deformation is not the dominant deformation process when predicting the mixed alkaline earth effect of hardness. If the composition dependence H_v is primarily controlled by the resistance to elastic deformation, it would be expected that the observed linear decrease in E would be superimposed on H_v. However, this is not the case as H_v generally increases with increasing f (i.e., not decreases as observed for E).

Densification

ρ (Fig. 9) exhibits the same compositional trend as E (Fig. 1), i.e., a linear decrease with increasing f, in consistence with the trend reported in Ref. 26. As MgO has a smaller molar mass than BaO, the decrease in ρ can be attributed to the substitution of Mg^{2+} ions for Ba^{2+} in former barium sites within the glassy network. This coincides with the general decrease in V_0 (Fig. 9) and E (Fig. 1), assuming that the Mg sites are essentially similar to the Ba sites.[26] Both density and refractive index have been used as indicators for the amount of densification (V_d) that occurs during indentation.[1,27] Within a family of glasses, as the density increases, the resistance towards densification intuitively becomes larger and the relative amount of densification therefore decreases. However, this is not the case for the glasses in this study. As f increases, ρ decreases, and thus, V_d would be expected to increase. However, on the contrary, an inverse relation is observed as shown in Fig. 5. The same inverse relation is observed for the bulk modulus (calculated from E

and G), as it decreases with increasing f. This means that V_d does not positively correlate with either bulk modulus (Fig. 1) or ρ (Fig. 9). Both V_d (Fig. 5) and V_R (Fig. 6) exhibit negative deviations from linearity, corresponding to a positive deviation in the resistance to densification. Assuming that densification is the dominant deformation process, H_v would be expected to positively deviate from linearity. In Fig. 3, it is seen that this is not the case.

It is worth mentioning that the investigated glasses, compared to, e.g., aluminosilicates, might undergo a larger degree of densification because boron could be converted from trigonal to tetrahedral configuration during indentation.[28,29] This conversion results in an increased density of the network, enhancing the effect of densification on hardness. However, the larger degree of densification in the boron-containing glasses compared to that of boron-free glasses is not observed, since V_R of the studied glasses (Fig. 6) is generally lower than that of a mixed Na/K aluminosilicate system without boron.[30] As no correlation is observed between V_d and H_v, we infer that densification is not the dominant deformation process during indentation of the studied glasses.

Plastic flow

G (Fig. 1), H_v (Fig. 3), and V_p (Fig. 5) are related to structural shear motion, and show a mixed alkaline earth effect.[16,31] m (Fig. 7) and T_g (Fig. 8) are dynamic quantities that relate to the viscosity of the glass, and they also exhibit a mixed alkaline earth effect. It has recently been proposed that in mixed modifier aluminosilicate glasses, plastic deformation is the dominant part of the total deformation,[4,13] and thus, the dominant factor in determining the compositional dependence of H_v. As known, G, m, and T_g all exhibit a negative mixed alkaline earth effect with largest deviation from linearity around $f = 0.5$. Hence, when both types of the alkaline earth ions co-exist in the glass, the resistance of the glass to deformation will be lowest because of the largest negative deviation from the linear trend of plastic flow. V_p undergoes a positive mixed alkaline earth effect, implying that the positive deviation of both shear and plastic flow from a linear trend reaches the highest degree near $f = 0.5$. This is in good agreement with the measured compositional scaling of hardness, and the findings presented in Ref. 4. The dominant role of plastic flow in determining the mixed alkaline earth effect on the glass hardness is verified by the measured composition dependence of indentation volumes (Fig. 5). Assuming a linear positive relation between deformation resistances and indentation volumes, the resistance of the glass to plastic flow should be four times larger than that to densification, since the value of V_p is four times smaller than that of V_d. In addition, it is interesting to note that the mixed alkaline earth effect is found for G, but not for E (Fig. 1). This confirms that plastic shear flow is the controlling deformation process for the compositional scaling of hardness, because G is inversely proportional to the degree of shear motion, whereas E negatively relates to the compactness of the glass.[32] The compositional trends of G and E are reflected in the compositional behavior of ν (Fig. 2).

As the compositional changes in E do not affect H_v, the resistance of the glass to elastic deformation is believed to be rather small compared to the resistance to plastic flow. As the indenter penetrates the glassy material, all three deformation modes co-act, but the one with the highest resistance to the external load is the dominant one in determining the glass hardness.[9] Hence, lowering the highest resistance of the deformation mode to the external load should affect the glass hardness the most, in agreement with the theory proposed by Yamane and Mackenzie,[9] according to which H_v is proportional to the geometrical average of the three resistances. Although plastic flow is the dominant deformation process, a quantitative link between plastic flow and Vickers hardness has not yet been established. This means that the degree of plastic flow exerts a much larger influence on Vickers hardness compared to that of both densification and elastic deformation. However, it is still not possible at this stage to predict the absolute hardness values solely from the plastic flow volumes.

Poisson's ratio

An alternative way to explain the compositional scaling of H_v is to explore the change of ν with composition. A general rule has been proposed to account for the relation between ν and V_R in glassy materials,[1,10] viz., an increase in ν results in a decrease in V_R. For small changes in ν, which is the case in this study (Fig. 2), the relation can be approximated by a linear scaling. That is, the tendency of the change of ν with composition corresponds to the inverse trend of V_R. This agrees with the results displayed in Figs. 2 and 6, where the observed compositional minimum in ν corresponds to the observed maximum in V_R. As mentioned earlier, the ratio between the deformation processes during indentation differs between different families of glasses, and any correlation between ν and H_v is thus not universal, as H_v does not correlate with the elastic part of indentation. Since ν relates to the ratio between transverse and axial strain, it is a viable index to discriminate between densification and plastic flow.[1] Higher values of ν correspond to a larger ratio of transverse to axial strain, and therefore, plastic flow is favored. Within the same glass series, e.g., mixed modifier silicate glasses, a correlation between the dominant deformation mechanism and H_v has been found to exist.[4,13] As observed in this work, within a given family of glasses, a correlation exists between ν and H_v.

CONCLUSIONS

In the investigated series of magnesium-barium boroaluminosilicate glasses, we have found that the mixed alkaline earth effects manifest themselves as deviations from linearity in shear modulus (G), Poisson's ratio (ν), Vicker's hardness (H_v), volume of densification (V_d), volume of plastic flow (V_p), volume recovery of indentation (V_R), glass transition temperatures (T_g), liquid fragility indices (m), and molar volume (V_0). We found that E and ρ do not exhibit a mixed alkaline earth effect, but exhibit linear composition dependence. We found no correlation between the observed compositional

trends of E and H_v. Since E represents the elastic part of indentation resistance, we infer that the elastic deformation does not play the dominant role in determining the mixed alkaline earth effect of hardness in mixed magnesium-barium boroaluminosilicate glasses. Instead, we confirm that plastic flow is the dominant deformation process during indentation of mixed modifier glasses.

Interestingly, we have also found that Poisson's ratio exhibits a positive deviation from compositional linear dependence, which is in agreement with the negative deviation from linearity observed in hardness. Higher values of Poisson's ratio correspond to a higher degree of shear and a higher volume of plastic flow, and thus, Poisson's ratio is negatively correlated to hardness in cases where either densification or plastic flow have the largest impact on glass hardness.

[1]T. Rouxel, J. Ji, J. P. Guin, F. Augereau, and B. Rufflé, J. Appl. Phys. **107**, 094903 (2010).
[2]W. B. Hillig, "Concerning the creation and stability of pyramidal hardness impression on glass," in *Proceedings of the VIth International Congress on Glass*, Washington, 8–14 July 1962 (American Ceramic Society, Westerville, OH, 1963), p. 51.
[3]E. W. Taylor, Nature **163**, 323 (1949).
[4]J. Kjeldsen, M. M. Smedskjaer, J. C. Mauro, and Y. Z. Yue, Appl. Phys. Lett. **104**, 051913 (2014).
[5]F. M. Ernsberger, J. Am. Ceram. Soc. **51**, 545 (1968).
[6]K. W. Peter, J. Non-Cryst. Solids **5**, 103 (1970).
[7]D. M. Marsh, Proc. R. Soc. A **282**, 33 (1964).
[8]A. K. Varshneya, Int. J. Appl. Glass Sci. **1**, 131 (2010).
[9]M. Yamane and J. D. Mackenzie, J. Non-Cryst. Solids **15**, 153 (1974).
[10]S. Yoshida, J.-C. Sanglebæuf, and T. Rouxel, J. Mater. Res. **20**, 3404 (2005).
[11]J. E. Neely and J. D. Mackenzie, J. Mater. Sci. **3**, 603 (1968).
[12]T. Rouxel, J. C. Sanglebæuf, C. Moysan, and B. Truffin, J. Non-Cryst. Solids **344**, 26 (2004).
[13]J. Kjeldsen, M. M. Smedskjaer, J. C. Mauro, R. E. Youngmann, L. Huang, and Y. Z. Yue, J. Non-Cryst. Solids **369**, 61 (2013).
[14]M. Jebahi, D. André, F. Dau, J. Charles, and I. Iordanoff, J. Non-Cryst. Solids **378**, 15 (2013).
[15]A. Makishima and J. D. Mackenzie, J. Non-Cryst. Solids **12**, 35 (1973).
[16]R. J. Hand and D. R. Tadjiev, J. Non-Cryst. Solids **356**, 2417 (2010).
[17]R. Kirchheim, J. Non-Cryst. Solids **328**, 157 (2003).
[18]M. M. Smedskjaer and M. Potuzak, J. Am Ceram. Soc. **96**, 2831 (2013).
[19]M. Potuzak and M. M. Smedskjaer, Phys. Chem. Glasses: Eur. J. Glass Sci. Technol. B **55**, 18 (2014).
[20]M. M. Smedskjaer, M. Potuzak, X. Guo, and J. C. Mauro, Opt. Mater. **35**, 2435 (2013).
[21]Y. Z. Yue, J. D. Christiansen, and S. L. Jensen, Chem. Phys. Lett. **357**, 20 (2002).
[22]P. Sellappan, T. Rouxel, F. Celarie, E. Becker, P. Houizot, and R. Conradt, Acta Mater. **61**, 5949 (2013).
[23]J. C. Mauro, Y. Z. Yue, A. J. Ellison, P. K. Gupta, and D. C. Allan, Proc. Natl. Acad. Sci. U.S.A. **106**, 19780 (2009).
[24]Q. Zheng, M. Potuzak, J. C. Mauro, M. M. Smedskjaer, R. E. Youngman, and Y. Z. Yue, J. Non-Cryst. Solids **358**, 993 (2012).
[25]M. M. Smedskjaer, J. C. Mauro, and Y. Z. Yue, Phys. Rev. Lett. **105**, 115503 (2010).
[26]N. Soga, H. Yamanaka, C. Hisamoto, and M. Kunugi, J. Non-Cryst. Solids **22**, 67 (1976).
[27]T. Rouxel, H. Ji, T. Hammouda, and A. Moréac, Phys. Rev. Lett. **100**, 225501 (2008).
[28]L. S. Du, J. R. Allwardt, B. C. Schmidt, and J. F. Stebbins, J. Non-Cryst. Solids **337**, 196 (2004).
[29]A. Winterstein-Beckmann, D. Moncke, D. Palles, E. I. Kamitsos, and L. Wondraczek, J. Non-Cryst. Solids **401**, 110 (2014).
[30]J. Kjeldsen, M. M. Smedskjaer, J. C. Mauro, and Y. Z. Yue, J. Non-Cryst. Solids **406**, 22 (2014).
[31]Y. Hasegawa, Glastech. Ber. **57**, 177 (1984).
[32]T. Rouxel, C. R. Mec. **334**, 743 (2006).

Paper VI

Journal of Non-Crystalline Solids 378 (2013) 196–200

Contents lists available at ScienceDirect

Journal of Non-Crystalline Solids

journal homepage: www.elsevier.com/ locate/ jnoncrysol

Electronic conductivity of vanadium-tellurite glass-ceramics

Jonas Kjeldsen [a], Yuanzheng Yue [a,*], Caio B. Bragatto [b], Ana C.M. Rodrigues [b,**]

[a] Section of Chemistry, Aalborg University, DK-9000 Aalborg, Denmark
[b] Department of Materials Engineering, Federal University of São Carlos, C.P. 676, 13565-905 São Carlos, SP, Brazil

ARTICLE INFO

Article history:
Received 27 February 2013
Received in revised form 25 June 2013
Available online 30 July 2013

Keywords:
Glass-ceramics;
Vanadium tellurite;
Electronic conductivity;
Cathode materials;
Glass transition temperature;
Percolation

ABSTRACT

In this paper, we investigate the electronic conductivity of $2TeO_2$–V_2O_5 glass-ceramics with crystallinity ranging from 0 to 100 wt.%, i.e., from entirely amorphous to completely crystalline. The glass is prepared by the melt quenching technique, and the crystal is prepared by subsequent heat treatment thereof. Glass-ceramics are prepared by mixing glass and crystal powder, followed by a sintering procedure. Activation energies for electronic conduction in the glass and in the crystal are determined by fitting the Mott–Austin equation to the electronic conductivity data obtained by impedance spectroscopy. We find similar activation energies for both glass and crystal, implying that they have similar conduction mechanisms, i.e., thermally activated hopping. The electronic conductivity of $2TeO_2$–V_2O_5 glass is about one order of magnitude higher than that of the corresponding crystal, and a percolation phenomenon occurs at a glass fraction of 61 wt.%, increasing from a lower conductivity in the crystal to a higher conductivity in the glass. We explain the behavior of electronic conduction in the $2TeO_2$–V_2O_5 glass-ceramics by considering constriction effects between particles as well as percolation theory. This work implies that, based on its electronic conductivity, vitreous $2TeO_2$–V_2O_5 is more suitable as a cathode material in secondary batteries compared to a $2TeO_2$–V_2O_5 glass-ceramic.

1. Introduction

Batteries are essential in modern society to sustain our high-tech lifestyles. Since a large segment of the world's population utilizes electronics powered by batteries every day, both available technologies for batteries and prospects for future technology are objects of extensive research. As an excellent source of mobile energy, batteries are receiving a large amount of attention compared to other available technologies.

Lithium is both the most electro-positive (−3.04 V vs. a standard hydrogen electrode) as well as the lightest metal and therefore has the strongest potential for designing batteries with a high energy density [1]. For high power electrochemical cells, it is important that the electronic conductivity in the electrodes is high and that there is a rapid change in charge carriers at the electrolyte/electrode interface (transfer from lithium ions in the electrolyte to electrons in the electrodes) [2]. Considering these requirements, the use of an amorphous mixed conductive electrode material has been proposed [2], i.e., an amorphous material that is able to conduct a current by both electrons and ions. Since V_2O_5–TeO_2 glass may intercalate lithium ions [3], the use of lithium-intercalated V_2O_5–TeO_2 may present several advantages: First, the change in charge carriers is not confined to the surface of the electrode but can extend through the material, which increases the number of sites available for transfer. Second, in an amorphous electrode, the electro-active species is separated from the electron and occupies well-defined cationic sites. When dissolved in this manner, the electro-active species is considered to be intercalated, and its chemical potential is far less than that of the pure species [2]. This difference in chemical potential is the driving force for current flow in a battery and is therefore highly important for the design of highly energy dense electrochemical cells. Third, when comparing amorphous and crystalline structures, degradation during consecutive lithiation cycles (repetitions of charging and discharging) is lowest in an amorphous material [2]. Compared to a crystalline material, the structural units in a glass are easier to rearrange, and thus, the glass is more resistant to the degradation caused by expansion during lithiation cycles.

The most common cathode material in secondary lithium batteries is $LiCoO_2$. However, $LiCoO_2$ only has a moderate energy density (measured in kWh/kg), and the CoO_2 layers created during delithiation (charging) are sheared from the electrode surface, which reduces the energy density because fewer lithium sites are available for lithiation [4]. Cobalt, which is both expensive and toxic, is also dissolved in the electrolyte during delithiation [5]. Due to the listed limitations of the current cathode material, it is of interest to find another material with superior properties. Lithium vanadiotellurite is a mixed conductor that previously has been suggested for use as a cathode material [2,3,6,7]. Vanadium tellurite is able to intercalate lithium ions and experiences high electronic conductivity compared to other binary or ternary vanadium compounds [2,8–21]. Because electronic conduction

* Corresponding author. Tel.: +45 9940 8522.
** Corresponding author. Tel.: +55 16 3351 8556.
E-mail addresses: yy@bio.aau.dk (Y.Z. Yue), acmr@ufscar.br (A.C.M. Rodrigues).

0022-3093/$ – see front matter © 2013 Elsevier B.V. All rights reserved.
http://dx.doi.org/10.1016/j.jnoncrysol.2013.07.011

occurs by electron hopping from one vanadium ion to another, theoretically, the highest electronic conductivity is achieved in pure vanadium oxide, simply because the distance between adjacent vanadium ions is minimized. Hirashima et al. [22] postulate that the conductivity of a vanadium tellurite crystal might be as high as that of a divanadium pentoxide crystal and that both are 2 orders of magnitude larger than that of the corresponding glass. The synthesis of congruent $2TeO_2$–V_2O_5 crystals has been reported [6,23–31], but to the best of our knowledge, the electronic conductivity of either the crystal or the mixtures between glassy and crystalline $2TeO_2$–V_2O_5 has not been measured. Therefore, in this paper, we investigate the dependence of the electronic conductivity on the weight % of glass in different mixtures of congruent $2TeO_2$–V_2O_5 crystal and glass.

2. Experimental

Glass samples were prepared via the normal melt quenching technique using reagent grade ≥99.6% V_2O_5 and ≥99.5% TeO_2. Appropriate amounts for obtaining $2TeO_2$–V_2O_5 were mortared, and 12 g was melted in a gold crucible at 700 °C for 1 h. The melt was quenched on a brass block and annealed for 2 h at 250 °C. Differential scanning calorimetry (DSC) (Netsch, DSC404) at 1 K/min was performed up to 400 °C on a solid sample using gold crucibles. Heat treatment was conducted at 400 °C for 2 h in order to crystallize the glass, and both crystalline and glassy samples were examined with a scanning electron microscope (SEM) (Phenom). Images were taken on the surface of the samples and in fractures (the interior of the samples). Different ratios of glass and crystal were mixed to obtain nine samples with a glass fraction ranging from 0 to 100 wt.%. Each sample was pressed under 20.6 MPa and sintered for 2 h at 270 °C. All samples were disc shaped with a diameter of 1.8 mm and a height of 1 mm. The temperature of sintering (T_s) was obtained with an optical dilatometer (Misura, HSM-ODHT) measuring 2-dimensional shrinkage during scans from 298 to 673 K with scanning rates of 2, 5 and 10 K/min. T_s is then defined as the temperature where the largest volume shrinkage occurs. SEM images were taken of these glass-ceramic samples. The samples were polished, and gold was sputtered on the parallel surfaces before the electronic conductivity was measured by impedance spectroscopy (IS) (Solartron, SI1260). The electrical measurements were performed in air with a two-point sample holder from 303 to 523 K and with an applied voltage of 100 mV in the frequency range from 10^6 to 1 Hz. X-ray diffraction (XRD) (Rigaku, Ultima IV) using Cu K_α-radiation was applied at room temperature on all samples in order to confirm their amorphous or crystalline states. Scans were conducted at 0.02°/s from 10 to 90°.

3. Results & discussion

Fig. 1 shows the DSC curve of the $2TeO_2$–V_2O_5 glass, from which the glass transition temperature (T_g) and the crystallization temperature (T_c) are determined to be 251 and 400 °C, respectively. T_c is determined from the crystallization peak position, whereas T_g is determined from the onset temperature of the glass transition [32,33]. The $2TeO_2$–V_2O_5 glass crystallizes around a single distinctive temperature, indicating the formation of one single crystalline phase. The T_g and T_c values agree well with those reported in the literature [13,25,30]. Figs. 2 and 3 show the XRD patterns and scanning electron microscopy images of both glassy and crystalline $2TeO_2$–V_2O_5 (the crystalline phase was obtained by heat treatment at 400 °C for 2 h). The XRD pattern confirms the amorphous nature of the sample before heat treatment due to the lack of Bragg peaks [34]. Fig. 2(b) and (c) shows that the XRD pattern of the analyzed sample coincides with the pattern of $2TeO_2$–V_2O_5 from the Joint Committee on Powder Diffraction Standards (card no. 71-0719) [25,29], indicating that the crystal obtained in this work is $2TeO_2$–V_2O_5. SEM images were taken of both glass and crystal (Fig. 3). As shown in Fig. 3, the glassy sample contains no

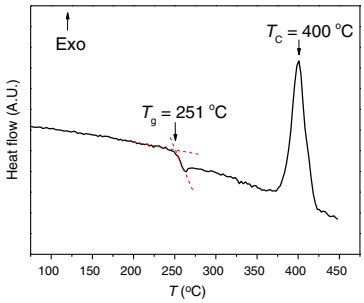

Fig. 1. A DSC scan of $2TeO_2$–V_2O_5 glass at a scanning rate of 1 K/min. Glass transition temperature (T_g) and crystallization temperature (T_c) are marked on the figure.

detectable crystals (Fig. 3(a)), and the crystalline sample contains no detectable vitreous phase either on the surface (Fig. 3(b)) or in the bulk (Fig. 3(c)); thus, the vitreous sample is fully amorphous, and the crystalline sample is completely crystallized.

The mixed glassy and crystalline samples are sintered at T_s = 543 K. As shown in Fig. 4, this temperature corresponds to that of the largest volume shrinkage and, hence, the highest sintering rate. Moreover, T_s is independent of the heating rate, and sintering starts almost immediately after the temperature is raised above T_g. Sintering, which is driven by a diffusion of atoms, occurs immediately after the temperature exceeds T_g due to a fast drop in viscosity upon heating, which indicates a fragile liquid. Fig. 4 shows that an expansion occurs at temperatures higher than T_s, which is attributed to the release of trapped air. At high heating rates, the time for the trapped air to be released is so short that the expansion becomes more pronounced (Fig. 4).

We analyzed a vitreous bulk sample and a vitreous sintered sample, i.e., a sample made by sintering glass powder following the sintering conditions described above, and found identical electronic conductivity for the two samples. XRD data confirm that both the bulk and the sintered powder samples are amorphous. Both samples present the same electrical conductivity, so the applied sintering process does not induce crystallization (which was expected based on Fig. 1.) and does not change the electronic conductivity. In Fig. 5, the electronic conductivity of a vitreous and a crystalline bulk sample is plotted against the inverse temperature. Earlier measurements combined with those presented in this paper show that by increasing the melting temperature, the electronic conductivity can be increased by 2 orders of magnitude [13–15]. Since an increase in melting temperature reduces the valence state of the vanadium in the melt, the

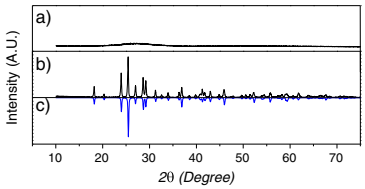

Fig. 2. X-ray diffraction patterns of (a) $2TeO_2$–V_2O_5 glass produced in this work, (b) $2TeO_2$–V_2O_5 crystal produced in this work, and (c) $2TeO_2$–V_2O_5 crystal from [29]. For better comparison between the crystal produced in this work and the crystal presented in [29], their pattern has been inversed (Fig. 2(c)).

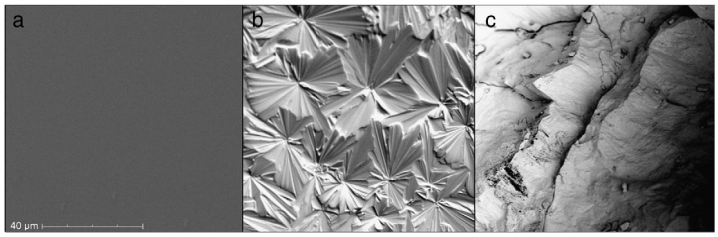

Fig. 3. Scanning electron microscopy images of (a) the surface of $2TeO_2$–V_2O_5 glass, (b) the surface of $2TeO_2$–V_2O_5 crystal, and (c) the fracture of $2TeO_2$–V_2O_5 crystal. The three images are taken with similar settings but (c) is taken at a lower magnitude compared to (a) and (b).

melting and annealing conditions are crucial parameters for varying the electronic conductivity. Therefore, a comparison of the electronic conductivity between two samples is only meaningful when they have identical thermal histories, as is the case for the samples presented in Fig. 5.

Electronic conductivity data were fitted using an equivalent circuit consisting of one resistor in parallel with one capacitor. By using a Levenberg–Marquardt algorithm, the variables from the equivalent circuit are fitted to the impedance data presented in a Nyquist plot, and the resistance of the sample is determined [35,36]. An example of the obtained IS data is shown in the inset of Fig. 5. The electronic conductivity (σ) is calculated using Eq. (1).

$$\sigma = \frac{1}{R_s} \cdot \frac{l}{A} \tag{1}$$

where l is the thickness of the sample, A is the area of the electrode in contact with the sample, and R_s is the resistance of the sample [13,37]. As shown in Fig. 5, the temperature dependence of $\log(\sigma T)$ follows a linear tendency and can therefore be approximated by the Mott–Austin equation [38,39].

$$\sigma = \left(\frac{\nu e^2}{Rk_bT}\right) c(1-c) e^{-2\alpha R} e^{-\frac{W}{k_bT}} \tag{2}$$

where ν is the optical phonon frequency, R is the mean distance between the ions where the electron transfer occurs (vanadium ions in this case), c is the concentration of these ions, α is the tunneling factor and W is the activation energy, which is split into two terms depending on temperature.

$$W = \begin{cases} W = W_H + \frac{1}{2}W_D & \text{for } T \geq \frac{1}{2}\Theta_D \\ W = W_D & \text{for } T \leq \frac{1}{2}\Theta_D \end{cases} \tag{3}$$

where W_H is the polaron hopping energy, W_D is the energy of disorder and Θ_D is the Debye temperature. The solid lines in Fig. 5 are Mott–Austin fits (Eq. (2)), from which the activation energies can be determined. The slopes of the straight lines are similar, which indicates that the activation energies are similar. The activation energies of the glass and the crystal are $W_{glass} = 0.39 \pm 0.03$ eV and $W_{crystal} = 0.42 \pm 0.03$ eV, respectively. The activation energies are determined using electronic conductivities in a temperature range from 303 to 523 K, which is much higher than $1/2\Theta_D$ [40], so the electronic conduction occurs by thermally activated hopping (Eq. (3)) [38]. Since the difference in activation energy between the two samples is within the error range, the mechanisms of electron transfer for the two samples are likely similar. The activation energy calculated for conduction in the glass is in good agreement with what have been reported in the literature, $W_{glass} = 0.42 \pm 0.08$ eV [13–15].

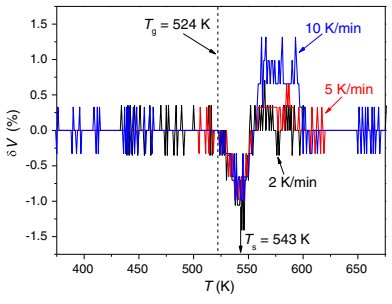

Fig. 4. Volume changes (δV) as a function of temperature measured with a heating microscope. The samples are vitreous $2TeO_2$–V_2O_5 with a starting volume of 2.5 mm^3. Isotropic shrinkage is assumed, and the heating rates are marked on the figure along with the sintering temperature (T_s) and the glass transition temperature (T_g).

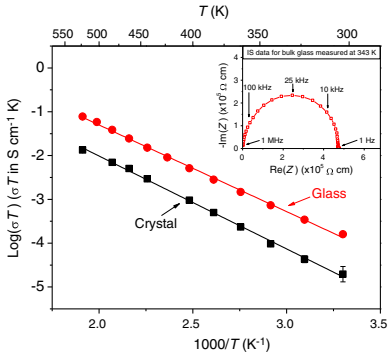

Fig. 5. $\text{Log}(\sigma T)$ as a function of the inverse temperature for both bulk $2TeO_2$–V_2O_5 crystal and glass. Solid lines: Mott–Austin fits (Eq. (2)) [38,39] with a correlation factor of $r^2 = 0.998$ for both lines. Both samples were melted at 973 K for 1 h and annealed at T_g for 2 h. Inset: Example of a semicircle obtained for glassy $2TeO_2$–V_2O_5 by impedance spectroscopy at 343 K. Note the absence of any low frequency spike attributable to the polarization of the electrode–electrolyte interface. Its absence is characteristic of pure electronic conductivity (no ionic transport) [49].

The electronic conductivity of samples with crystallinity ranging from 0 to 1 is plotted against the inverse temperature in Fig. 6. The base glass of these samples experienced different annealing conditions from those whose electronic conductivity is presented in Fig. 5. Therefore, the electronic conductivities presented in Figs. 5 and 6 are not comparable. Fig. 6 shows that the electronic conductivity of the glass-ceramic samples increases with increasing temperature in a non-Arrhenian way. It should be mentioned that the Mott–Austin equation is applicable only for monophase structures and not for multi-phase systems, such as glass-ceramics [39]. This limitation is due to possible differences in the temperature dependence of activation energies for different phases.

Fig. 6 shows that the electronic conductivity increases with an increasing fraction of glass in the sample. This trend is better revealed in Fig. 7, where the electronic conductivity measured at different temperatures is plotted against the glass fraction in the samples. All four curves show the same overall trend of two plateaus separated by a transition zone. The crossover from low to high conductivity occurs at a glass fraction of about 61 wt.%. Another trend is that the enhancement of the electronic conductivity by increasing the glass fraction is more pronounced at low temperatures than at high temperatures (inset of Fig. 6). As the activation energy of the glassy phase is slightly higher than that of the crystal, a more pronounced difference in electrical conductivity at low temperatures is expected.

According to [38], the Mott–Austin equation (Eq. (2)) is only applicable for monophase systems. However, here, we show that the activation energies for the two different phases are constant in the entire temperature range of measurement, implying that the Mott–Austin equation could be applicable. All samples have comparable α and ν values (Eq. (1)) because they have identical chemical compositions. This leaves us with only two parameters, namely, c and R, which can be related to the dependence of the glass fraction on the electronic conductivity. This dependence results from either: changes in the redox state of vanadium in crystallized samples (reflected by changes in c) or limitation of the electronic conduction in the grain boundaries. A reduced conduction in grain boundaries has been shown for ionic conductors [41,42] and is attributed to a constriction effect caused by a small contact area between grains [43]. This may also be applied in the present case of electronic conduction in mixed crystalline and vitreous grains. The sigmoid shape of the curves (Fig. 7) indicates a percolation threshold, which could be caused by the lower intrinsic electronic conductivity in the crystal grains

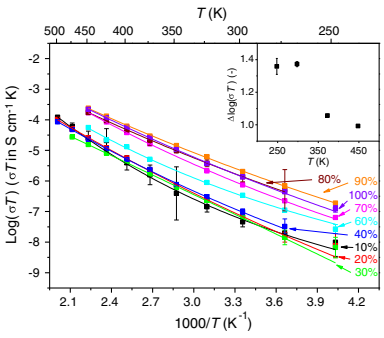

Fig. 6. Log(σT) as a function of the inverse temperature for different wt.% of glass in the glass-ceramic samples (marked on the curves), where σ is the electronic conductivity. The solid lines are guides for the eyes. Inset: $\Delta\log(\sigma T)$ as a function of temperature, where $\Delta\log(\sigma T)$ is the difference in $\log(\sigma T)$ between the sample containing 90 wt.% glass and that containing 10 wt.% glass.

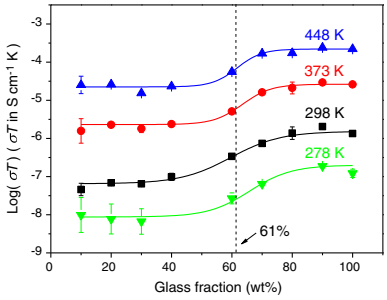

Fig. 7. Electronic conductivities measured at different temperatures (marked on the curves) as a function of the glass fraction in the $2TeO_2$–V_2O_5 glass-ceramic samples. Solid lines: sigmoid fits; Vertical dashed line: crossover point of the sigmoid curves.

compared to that in the glassy grains. Since the electronic conductivity is higher in the glassy grains than in the crystal grains, the glassy phase facilitates the electrons' preferred pathway. Fig. 7 suggests that an interconnected pathway of glass grains does not occur until the glass fraction reaches 61 wt.%, which agrees with the critical site percolation concentration (p_c) of 0.59 in a 2-dimensional square lattice [44–46]. However, a 3-dimensional network of randomly packed spheres has a p_c of 0.27 (16 vol.%) [45], whereas a 3-dimensional cubic lattice has a p_c of 0.31 [46]. These p_c values are inconsistent with the findings depicted in Fig. 7. If the conductivity jump illustrated in Fig. 7 originates from a percolation threshold, the system studied in this work would considerably differ from the ideal systems described by the models proposed in [45–47]. The cause of the measured p_c being relatively high could lie in either a small packing fraction of the glass-ceramic or a low average coordination number of the grains. Either cases alone or a combination hereof leads to an increase of apparent p_c [45,47,48]. From the SEM image in Fig. 8, it is difficult to determine the apparent particle size distribution or particle morphology and to make a link between the experimental system and the models described elsewhere [44–46]. In Fig. 8, it is not possible to distinguish between the glassy and crystalline grains, as the difference in electronic density between the two phases is too small. If possible, this would have provided important information about the percolation threshold. Using the critical glass fraction of 61 wt.%, we can infer that below this value, the electrons must travel through

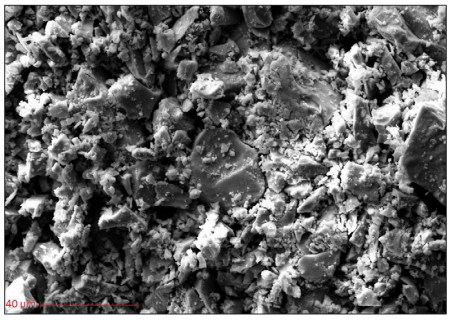

Fig. 8. SEM image of a glass-ceramic sample with a glass fraction of 30 wt.%. The image was taken in a fracture.

crystal regions of lower conductivity, thus reducing the overall electronic conductivity, whereas above this value an interconnected glass phase exists, and the electrons may therefore travel only in the glassy grains, increasing the electronic conductivity. Fig. 6 shows that the electronic conductivity of vitreous $2TeO_2–V_2O_5$ is up to 1.5 orders of magnitude higher than that of the crystal. This result is in contrast to results reported in [22], where the electronic conductivity of a $2TeO_2–V_2O_5$ crystal was 2 orders of magnitude higher than that of the corresponding glass. This discrepancy could be related to differences in the redox state of the vanadium ions in the samples in this work and in the samples investigated in [22]. It is also worth noting that the crystallized $2TeO_2–V_2O_5$ samples studied in [22] contained V_2O_5-crystals that may have contributed to the increased electronic conductivity of the $2TeO_2–V_2O_5$ glass-ceramic.

4. Conclusions

Activation energies for electronic conduction determined in the temperature range from 303 to 523 K in both vitreous and crystallized $2TeO_2–V_2O_5$ are found to be similar within experimental error, where $W_{glass} = 0.39 \pm 0.03$ eV and $W_{crystal} = 0.42 \pm 0.03$ eV. These results indicate that the mechanisms of electronic conduction are similar, i.e., thermally activated hopping. The electronic conductivity of vitreous $2TeO_2–V_2O_5$ is up to 1.5 orders of magnitude higher than that of the crystal, suggesting that $2TeO_2–V_2O_5$ glass is more suitable for use as a cathode material in secondary batteries than a $2TeO_2–V_2O_5$ glass-ceramic. The lower electronic conductivity of the glass-ceramic samples, compared to that of the amorphous one, is explained by constriction effects in the grain boundaries. A jump in electronic conductivity is observed at a glass fraction of 61 wt.%, and is attributed to a critical percolation concentration, which is higher than the theoretical value due to heterogeneities and flaws in the investigated system.

Acknowledgments

We thank the collaboration partners of the Department of Materials Engineering at Federal University of São Carlos for their help with sample preparation and characterization. Ana C. M. Rodrigues and Caio B. Bragatto acknowledge support from Fapesp, the São Paulo state funding agency. Ana C. M. Rodrigues acknowledges support from grant # 2007/08179-9, São Paulo State Research Foundation (Fapesp)-Brazil.

References

[1] A. Patil, V. Patil, D.W. Shin, J.-W. Choi, D.-S. Paik, S.-J. Yoon, Mater. Res. Bull. 43 (2008) 1913.
[2] M. Levy, J.L. Souquet, Mater. Chem. Phys. 23 (1989) 171.
[3] M. Levy, M.J. Duclot, F. Rousseau, J. Power Sources 26 (1989) 381.
[4] J.W. Fergus, J. Power Sources 195 (2010) 939.
[5] A.G. Ritchie, J. Power Sources 96 (2001) 1.
[6] P. Rozier, T. Dubois, P. Sallas, J. Non-Cryst. Solids 311 (2002) 241.
[7] M.A. Frechero, O.V. Quinzani, R.S. Pettigrosso, M. Villar, R.A. Montani, J. Non-Cryst. Solids 353 (2007) 2919.
[8] L. Murawski, R.J. Barczynski, Solid State Ionics 176 (2005) 2145.
[9] R.A. Montani, A. Robledo, J.C. Bazán, Mater. Chem. Phys. 53 (1998) 80.
[10] N. Lebrun, M. Levy, J.L. Souquet, Solid State Ionics 40/41 (1990) 718.
[11] M. Levy, F. Rousseau, M.J. Duclot, Solid State Ionics 28–30 (1988) 736.
[12] C.H. Chung, J.D. Mackenzie, J. Non-Cryst. Solids 42 (1980) 357.
[13] M.M. El-Desoky, Mater. Chem. Phys. 73 (2002) 259.
[14] G.D.L.K. Jayasinghe, M.A.K.L. Dissanayake, M.A. Careem, J.L. Souquet, Solid State Ionics 93 (1997) 291.
[15] R.A. Montani, A. Lorente, M.A. Vincenzo, Solid State Ionics 130 (2000) 91.
[16] B.W. Flynn, A.E. Owen, J.M. Robertson, Proc. 10th Int. Conf. on Amorphous and Liquid, Semiconductors, 1977, p. 678.
[17] H. Mori, H. Matsuno, H. Sakata, J. Non-Cryst. Solids 276 (2000) 78.
[18] D. Souri, J. Non-Cryst. Solids 356 (2010) 2181.
[19] T. Sankarappa, M.P. Kumar, G.B. Devidas, N. Nagaraja, R. Ramakrishnareddy, J. Mol. Struct. 889 (2008) 308.
[20] V.K. Dhawan, A. Mansingh, M. Sayer, J. Non-Cryst. Solids 51 (1982) 87.
[21] N. Chopra, A. Mansingh, G.K. Chadha, J. Non-Cryst. Solids 126 (1990) 194.
[22] H. Hirashima, M. Ide, T. Yoshida, J. Non-Cryst. Solids 86 (1986) 327.
[23] G.A. Chase, C.J. Phillips, J. Am. Ceram. Soc. 47 (1964) 467.
[24] H. Sakata, M. Amano, T. Yagi, J. Non-Cryst. Solids 194 (1996) 198.
[25] M. Nlyaz Ahamad, R. Vaish, K.B.R. Varma, J. Therm. Anal. Calorim. 105 (2011) 239.
[26] G.R. Jones, I.M. Young, J.W. Burgess, C. O'Hara, R.W. Whatmore, J. Phys. D Appl. Phys. 13 (1980) 2143.
[27] D. Xiao, S. Wang, E. Wang, Y. Hou, Y. Li, C. Hu, L. Xu, J. Solid State Chem. 176 (2003) 159.
[28] S. Sakida, S. Hayakawa, T. Yoko, J. Phys. Condens. Matter 12 (2000) 2579.
[29] J. Darriet, J. Galy, Cryst. Struct. Commun. 2 (1973) 237.
[30] V. Dimitrov, J. Solid State Chem. 66 (1987) 256.
[31] S. Rada, M. Rada, E. Culea, Spectrochim. Acta A 75 (2010) 846.
[32] Y.Z. Yue, J.deC. Christiansen, S.L. Jensen, Chem. Phys. Lett. 357 (2002) 20.
[33] Q. Zheng, M. Potuzak, J.C. Mauro, M.M. Smedskjaer, R.E. Youngmann, Y.Z. Yue, J. Non-Cryst. Solids 358 (2012) 993.
[34] L. Lutterotti, R. Ceccato, R.D. Maschio, E. Pagani, Mater. Sci. Forum 278–281 (1998) 87.
[35] K. Levenberg, Q. Appl. Math. 2 (1944) 164.
[36] D.W. Marquardt, J. Soc. Ind. Appl. Math. 11 (1963) 431.
[37] L.F. Maia, A.C.M. Rodrigues, Solid State Ionics 168 (2004) 87.
[38] N.F. Mott, Adv. Phys. 16 (1967) 49.
[39] I.G. Austin, N.F. Mott, Adv. Phys. 18 (1969) 41.
[40] M.A. Sidkey, R. El Mallawany, R.I. Nakhla, A. Abd El-Moneim, J. Non-Cryst. Solids 215 (1997) 75.
[41] N.M. Beekmans, L. Heyne, Electrochim. Acta 2 (1976) 303.
[42] J.E. Bauerle, J. Phys. Chem. Solids 30 (1969) 2657.
[43] G. Bruce, A.R. West, J. Electrochem. Soc. 130 (1983) 918.
[44] K. Shida, R. Sahara, M.N. Tripathi, H. Mizuseki, Y. Kawazoe, Mater. Trans. 50 (2009) 2848.
[45] R. Zallen, The Physics of Amorphous Solids, Wiley-VCH, 1998.
[46] M.N. Rahaman, Ceramic Processing and Sintering, CRC Press, 2003.
[47] I.J. Youngs, J. Phys. D Appl. Phys. 35 (2002) 3127.
[48] M. Sahimi, B.D. Hughes, L.E. Scriven, H.T. Davis, J. Phys. C Solid State Phys. 16 (1983) L521.
[49] A. Huanosta, A.R. West, J. Appl. Phys. 61 (1987) 5386.